Microstructure and displacements of the gerbil incudostapedial joint under static pressures

Sajjad Feizollah

Department of BioMedical Engineering

McGill University, Montréal

August 2019

A thesis submitted to McGill University

in partial fulfillment of the requirements of the degree of

Master of Engineering

Microstructure and displacements of the gerbil incudostapedial joint under static pressures

Abstract

Understanding middle-ear mechanics is crucial to the development of effective screening and diagnostic methods for ear disorders. Developing three-dimensional finite-element models of the middle ear has been an effective approach to study its mechanical behaviour and to simulate clinical tests. Tympanometry is a clinical test in which a quasi-static pressure is introduced in the ear canal along with an acoustical excitation and the response of the outer and middle ear is determined as an acoustical input admittance. Measuring the effects on the middle ear of tympanometry-like static pressures helps us to understand the hearing mechanism, and provides valuable data to validate quantitative models. Our goal in this study was to measure displacements of the lenticular plate of the incus and of the head of the stapes, and to examine microstructural changes of the incudostapedial joint, under static pressures in the gerbil.

A stereoscopic microscope with a video camera was used to record displacements of the lenticular plate and stapes under ramp pressure signals applied to the ear canal. These videos were processed using an object-tracking algorithm based on the Lucas-Kanade method, to obtain displacements of the lenticular plate and stapes. For the microstructural study, the ossicles were immobilized in the presence of an ear-canal static pressure, using an adhesive applied to the incus and malleus at the incudomallear joint, and to the stapes footplate. We used two imaging modalities to investigate the incudostapedial joint structure: X-ray nanoCT and light-sheet microscopy. Samples were stained with phosphotungstic acid in order to enhance soft-tissue visualization in nanoCT. For the

light-sheet microscopy, we employed a modified tissue-clearing method which consisted of polymerization, decalcification, and refractive-index matching.

Our displacement results obtained from three ears showed average total displacements (from fully compressed to fully stretched) of 19.6 μm for the lenticular plate, and 13.9 μm for the stapes. Changes in the incudostapedial gap size were then calculated by subtracting the stapes displacements from the lenticular-plate displacements. The average total increase of the gap across all three ears was 6.6 μm. Measurements of the microstructure of the incudostapedial joint were done in three samples using nanoCT, and in one sample using light-sheet microscopy. Three fresh samples were prepared under a pressure of 0 Pa; in addition, one previously frozen sample was prepared under a pressure of −2500 Pa. The average sizes of the gaps at 0 Pa were 10 μm and 9 μm for the two samples using nanoCT, and 9 μm for the one using light-sheet microscopy. The average size of the gap in the nanoCT sample prepared at −2500 Pa was 73 μm.

Résumé

Comprendre la mécanique de l'oreille moyenne est crucial pour le développement de méthodes efficaces de dépistage et de diagnostic des troubles de l'oreille. Le développement de modèles tridimensionnels à éléments finis de l'oreille moyenne s'est avéré une approche efficace pour étudier son comportement mécanique et simuler des tests cliniques. La tympanométrie est un test clinique dans lequel une pression quasi statique est introduite dans le canal auditif avec une excitation acoustique et la réponse de l'oreille externe et moyenne est déterminée en tant qu'admission acoustique. Mesurer les effets sur l'oreille moyenne de pressions statiques analogues à la tympanométrie nous aide à comprendre le mécanisme auditif et fournit des données précieuses pour la validation de modèles quantitatifs. Notre objectif dans cette étude était de mesurer les déplacements de la plaque lenticulaire de l'incus et de la tête du stapes, et d'examiner les modifications microstructurales de l'articulation incudostapédienne, sous des pressions statiques chez le gerbille.

Un microscope stéréoscopique avec une caméra vidéo a été utilisé pour enregistrer les déplacements de la plaque lenticulaire et du stapes sous des signaux de pression de rampe appliqués au canal auditif. Ces vidéos ont été traitées à l'aide d'un algorithme de suivi d'objet basé sur la méthode Lucas-Kanade, afin d'obtenir les déplacements de la plaque lenticulaire et du stapes. Pour l'étude microstructurale, les osselets ont été immobilisés en présence d'une pression statique dans le canal auditif, à l'aide d'un adhésif appliqué sur l'incus et le malleus au niveau de l'articulation incudomalléaire et de la plaque de base du stapes. Nous avons utilisé deux méthodes d'imagerie pour étudier la structure de l'articulation incudostapédienne: le nanoCT à rayons X et la microscopie à couches minces. Les échantillons ont été colorés avec de l'acide phosphotungstique afin d'améliorer la visualisation des tissus mous par nanoCT. Pour la microscopie à couches minces, nous avons utilisé

une méthode de clarification des tissus modifiée consistant en une polymérisation, une décalcification et une adaptation à l'indice de réfraction.

Nos résultats de déplacement obtenus à partir de trois oreilles ont montré des déplacements totaux moyens (de complètement compressé à complètement étiré) de 19,6 µm pour la plaque lenticulaire et de 13,9 µm pour le stapes. On a ensuite calculé les modifications de la taille de l'écart incudostapédien en soustrayant les déplacements du stapes aux déplacements de la plaque lenticulaire. L'augmentation totale moyenne de l'écart dans les trois oreilles était de 6,6 µm. Les mesures de la microstructure de l'articulation incudostapédienne ont été effectuées dans trois échantillons en utilisant nanoCT, et dans un échantillon en utilisant une microscopie à couches minces. Les trois échantillons ont été préparés sous une pression de 0 Pa; en outre, un échantillon préalablement congelé a été préparé sous une pression de −2500 Pa. Les tailles moyennes des lacunes pour les trois échantillons préparés à 0 Pa étaient de 10 µm et 9 µm avec du nanoCT et de 9 µm avec la microscopie à couches minces. La taille moyenne de l'écart dans l'échantillon préparé à −2500 Pa était de 73 µm.

Acknowledgements

I would like to thank all the people who have helped me to complete my work. First of all, I would like to express my deep appreciation to my supervisor Dr. W. Robert J. Funnell for accepting me into his group and helping me throughout the years of my master's. Without his broad knowledge and his guidance and incredible patience I would not have been able to perform this work.

I would like to express my deep gratitude to my parents, who have always helped and supported me anytime and anywhere.

I would like to thank Dr. Marc D. McKee for providing access to his lab and invaluable suggestions that helped me understand and overcome many problems in my thesis.

I would like to thank Dr. Erika Wee at the McGill Advanced BioImaging Facility (ABIF) for her consultation and helping me with the light-sheet microscopy. I would also like to thank Dr. Rui Tahara for helping me with the nanoCT scans.

I would like to thank my friends and colleagues in our AudiLab for all of their suggestions and discussions about my work. I especially thank my dear friend Orhun for his valuable help in conducting experiments and providing tools I needed for my work. Without his help I would not have been able to perform my experiments smoothly. I want to acknowledge Majid for his comments and patience in explaining basic concepts for me. I want to thank Marzieh for her valuable questions and kindness. I was fortunate that Tina and I started our master's together. I want to thank her for her support and kindness during my master's.

I would also like to thank Pina Sorrini, Trang Q. Tran, and Sabrina Teoli for their invaluable help.

This work was supported by the Canadian Institutes of Health Research, the Natural Sciences and Engineering Research Council of Canada and the BioMedical Engineering Department.

Table of Contents

Chapter 1. Introduction

1.1 Motivation

The peripheral auditory system is a complex structure converting mechanical sound waves to electrical impulses that can be interpreted by the brain. Efforts to understand its remarkable mechanical and electrical functions, and to find new methods for diagnosis and treatment of auditory disorders, have motivated researchers to simulate its behaviour using quantitative modelling. Among modelling approaches, finite-element analysis is a powerful tool to study mechanical phenomena. It is a numerical method for solving a complex system by dividing it into smaller, simpler parts that are called finite elements. The equations that model these small finite elements, individually simple, can be combined to form large matrix equations to model the entire system.

One of the applications of finite-element analysis is modelling clinical tests with the goal of understanding the underlying mechanisms of hearing in order to improve the tests for better screening and diagnosis. Tympanometry is one of these tests, in which a quasi-static pressure sweep is introduced in the ear canal along with an acoustical excitation and the response of the outer and middle ear is determined as an acoustical input admittance. Finite-element models have been developed to simulate this test. In order to validate such models, measurements of the behaviour of the middle ear in experimental animals under the same conditions are acquired.

The geometry of a model plays an important part in the accuracy of the estimated solution. Moreover, measurements of the geometry changes under different conditions help us to validate these models. Therefore, knowledge of the anatomy of the ear and its changes under quasi-static pressure variations is very important.

1.2 Objectives

In this study, our objective was to experimentally simulate tympanometric quasi-static pressures in the gerbil middle ear, and to measure the displacements and microstructural changes of the middle-ear structures, in particular the lenticular plate, stapes, and incudostapedial joint. Specifically, our objectives were:

1. Measurement of displacements of the lenticular plate and stapes under ramp static pressures.
2. Examination of microstructural changes of the incudostapedial joint under static pressures.

1.3 Thesis outline

Chapter 2 includes an overview of gerbil middle-ear anatomy and a literature review of previous studies related to this work. In Chapter 3, the proposed methods are described. This is followed by our results in Chapter 4. In Chapter 5, a summary of our work is presented, and future work and significance are discussed.

Chapter 2. Gerbil auditory system

2.1 Introduction

In this chapter, we first describe the anatomy of the gerbil ear in Section 2.2, then the methods that have been used to gain anatomical information will be surveyed in Section 2.3. In Section 2.4, methods that reveal the dynamic changes of the ear anatomy under pressure changes will be reviewed.

2.2 Review of anatomy

Experimental animals are used for invasive and harmful procedures that are not possible to perform on humans. They are easily accessible for both in-vivo and post-mortem experiments, and have less inter-subject variability than humans do. Additionally, recently euthanized animals are fresher than the human cadavers generally used for medical research. Over the last few decades, Mongolian gerbils (*Meriones unguiculatus*) have been very widely used in middle-ear research. Their affordability, relatively large eardrum-to-body-size ratio, and accessible middle-ear structures make them good candidates for auditory research. The peripheral auditory system in human and gerbil is divided into three parts: outer ear, middle ear, and inner ear. Air-borne sound waves are directed into the system through the outer ear, which itself consists of the pinna and ear canal. Then, those sound waves are converted into mechanical vibrations and transmitted to the inner ear by the structures in the middle ear, including the tympanic membrane (TM) or eardrum, and the ossicular chain (malleus, incus and stapes) with their attachments (ligaments and muscles). The vibrations are then transferred by the stapes, through the oval window, to the liquid-filled cochlea in the inner ear. The liquid motions vibrate the hair cells which consequently generate electrical signals that are perceivable by the brain. The details of the anatomy of the human temporal bone can be found in standard anatomy books (e.g., Gulya, 1995). In Figure 2.1

the overall anatomy of the human ear is shown. In this section, we will only cover the anatomy of the gerbil ear.

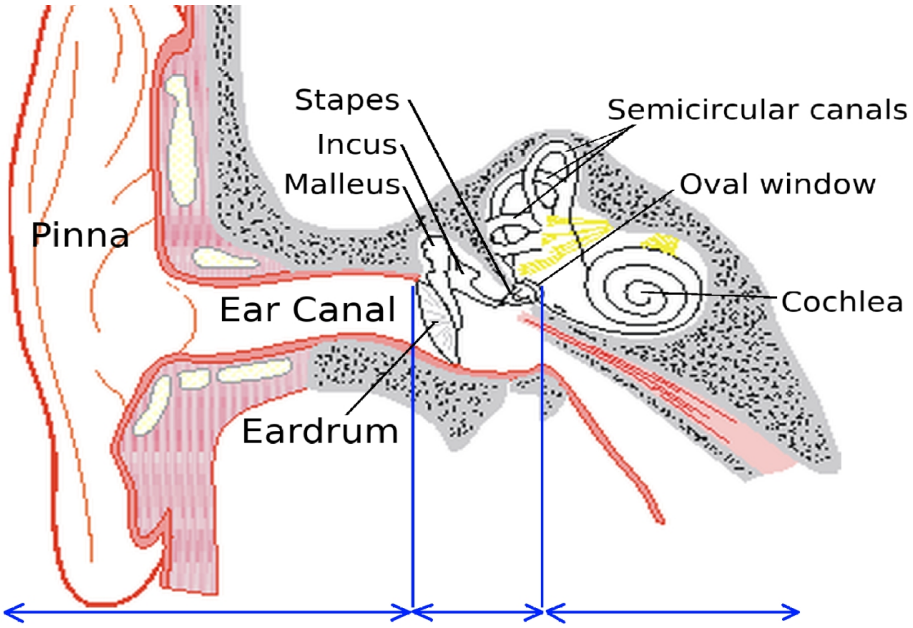

Figure 2.1: Human temporal bone anatomy. The outer, middle, and inner ear spaces are separated with blue lines from left to right respectively. (Adapted from: http://audilab.bme.mcgill.ca/AudiLab/teach/me_saf/me_saf.html, accessed on 2019 July 19)

2.2.1 Gerbil outer-ear anatomy

The outer ear consists of the pinna and the ear canal. The pinna is the visible part of the outer ear which collects sound waves. It is connected to muscles allowing it to make subtle movements in response to different sound frequencies, amplitudes and directions.

The ear canal is an air-filled tube that has two parts: cartilaginous tissue, and the bony meatus. The soft part connects the pinna to the bony meatus, which is covered with a layer of pigmented skin attached to the boundary of the TM.

2.2.2 Gerbil middle-ear anatomy

The middle ear starts with the TM at the medial end of the ear canal, and ends with the footplate of the stapes at the oval window of the inner ear. The function of the middle ear is to

match the low acoustical impedance of the air to the high acoustical impedance of the liquid in the cochlea. In Figure 2.2 the arrangement of the main middle-ear components are shown.

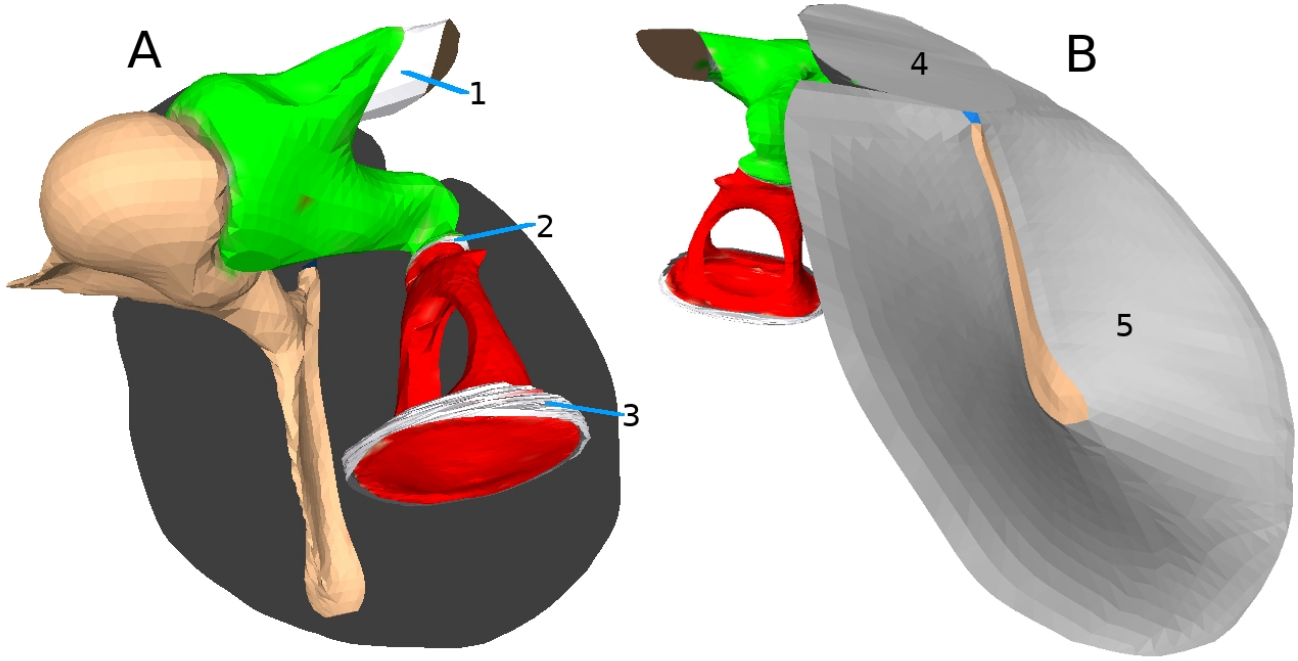

Figure 2.2: Middle-ear structures: (A) Medial view: beige: malleus; green: incus; and red: stapes. (B) Lateral view: grey: TM, beige: manubrium (handle of the malleus). (1) posterior incudal ligament in white, (2) incudostapedial joint in white, (3) stapedial annular ligament in white, (4) pars flaccida, (5) pars tensa. (Derived from model of Maftoon (2014))

2.2.2.1 Middle-ear cavity

The middle-ear cavity is a bony chamber that takes up a significant volume of the gerbil's skull. Similar to the ear canal, the bulla is filled with air. A thin mucosal layer covers the inner surface of the cavity. The Eustachian tube connects the bulla to the nasopharynx to equalize the pressure of the middle ear and the ambient pressure.

2.2.2.2 Tympanic membrane

The TM (the grey structure in the lateral view in Figure 2.2) is a very thin structure separating the outer-ear and middle-ear spaces. It is divided into two parts with different micro structures: the smaller segment is the pars flaccida ((4) in Figure 2.2), and the larger one is the pars tensa ((5) in Figure 2.2). The pars tensa is connected to the bony meatus by a

fibrocartilaginous ring. The pars tensa has an additional attachment in the middle to the handle (manubrium) of the malleus. The TM is concave toward the middle ear, with the most depressed region called the umbo.

Both the pars tensa and pars flaccida are made up of three layers: an outer epidermal layer, an inner mucosal layer, and a layer in the middle called the lamina propria. Figure 2.3 shows the layers of the pars tensa. The lamina propria of the pars tensa is the most complex and organized layer of the TM, and is composed of four sublayers: subepidermal connective tissue, radial and circular fibres, and submucosal connective tissue. The subepidermal connective-tissue sublayer consists of loose collagen fibres, fibroblasts, capillaries, and nerve fibres (Lim, 1968a). The radial fibres start from the manubrium and extend toward the fibrocartilaginous ring. The circular fibres start from one side of the manubrium and extend circumferentially to the inferior part of the TM and then around toward the other side of the manubrium (Shimada & Lim, 1971). In the pars flaccida the radial and circular fibres of the lamina propria are not present but a large amount of elastic fibres can be found (Lim, 1968b).

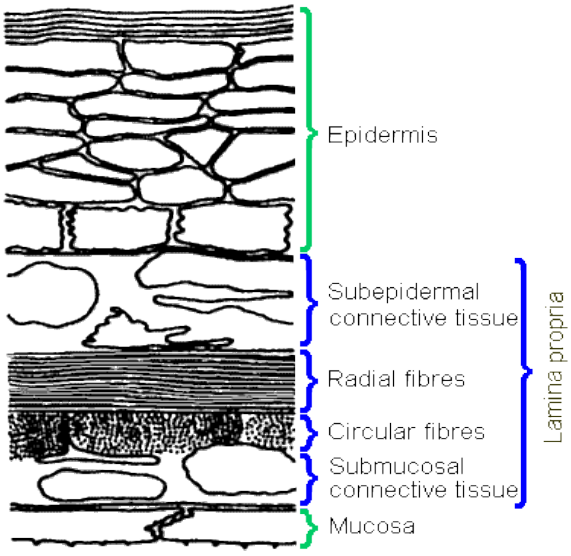

Figure 2.3: Layers of the pars tensa (Source: http://audilab.bme.mcgill.ca/AudiLab/teach/me_saf/me_saf.html, after Lim DJ (1968a) accessed on 2019 July 3)

The thickness of the TM is not uniform. In the gerbil (Kuypers et al., 2005), the thickness of the pars-tensa central region, forming a horse-shoe shape between the manubrium and the fibrocartilaginous ring, is about 7 μm. Moving away from the central region, the thickness gradually increases to about 20 μm near the manubrium, and about 35 μm near the annulus. The pars flaccida in general is thicker than the pars tensa: The central region is about 24 μm thick and the thickness near the edges increases steeply to about 80 μm.

2.2.2.3 Ossicles

Three bones in the middle ear form the ossicular chain: malleus, incus and stapes. They transmit the TM's vibrations to the cochlea. The malleus (the brown structure in Figure 2.2) has three principal parts: the long and thin manubrium, a head, and a long anterior process. The malleus adheres to the TM at the manubrium and attaches to the incus at the malleus head forming a synovial incudomallear (IM) joint. The anterior process of the malleus is attached to the bulla wall with a bony attachment (Rosowski et al., 1999). In addition to these connections, there is also a tendon attaching the tensor tympani muscle to the malleus neck.

The incus (the green structure in Figure 2.2) is the second bone in the chain and has three main parts: a head, a short process, and a long process. The head of the incus articulates with the head of the malleus at the IM joint. At the end of the long process of the incus there is usually, but apparently not always (Djerić et al., 1987), a small region called the lenticular process where the incus is joined to the head of the stapes (e.g., Shrapnell, 1832; Eysell, 1970; Hüttenbrink, 1988). The incus has a posterior ligament ((1) in Figure 2.2) between the short process of the incus and the bulla wall.

Accurate determination of the anatomy of the lenticular process has been a challenge, due to its delicacy and tiny dimensions. During the last two decades, new studies have revealed more details about the structure of the lenticular process. It is composed of the pedicle and the

lenticular plate (LP). The pedicle is a very thin bony structure attaching the incus and the lenticular plate, possibly making a significant contribution to the flexibility of the incus-stapes coupling (Funnell et al., 2005).

Between the lenticular plate and the head of the stapes there is the smallest synovial joint in the body, called the incudostapedial (IS) joint ((2) in Figure 2.2). Figure 2.4 shows the gerbil lenticular process and stapes in their natural undisturbed condition. The IS joint in both human and gerbil consists of synovial fluid, articular cartilage (calcified and uncalcified), and a joint capsule. A cross-sectional histological image of the gerbil IS joint is displayed in Figure 2.5. As can be seen, the joint has a width of about 300 μm in the gerbil. In the figure the capsule is broken and the joint is dislocated.

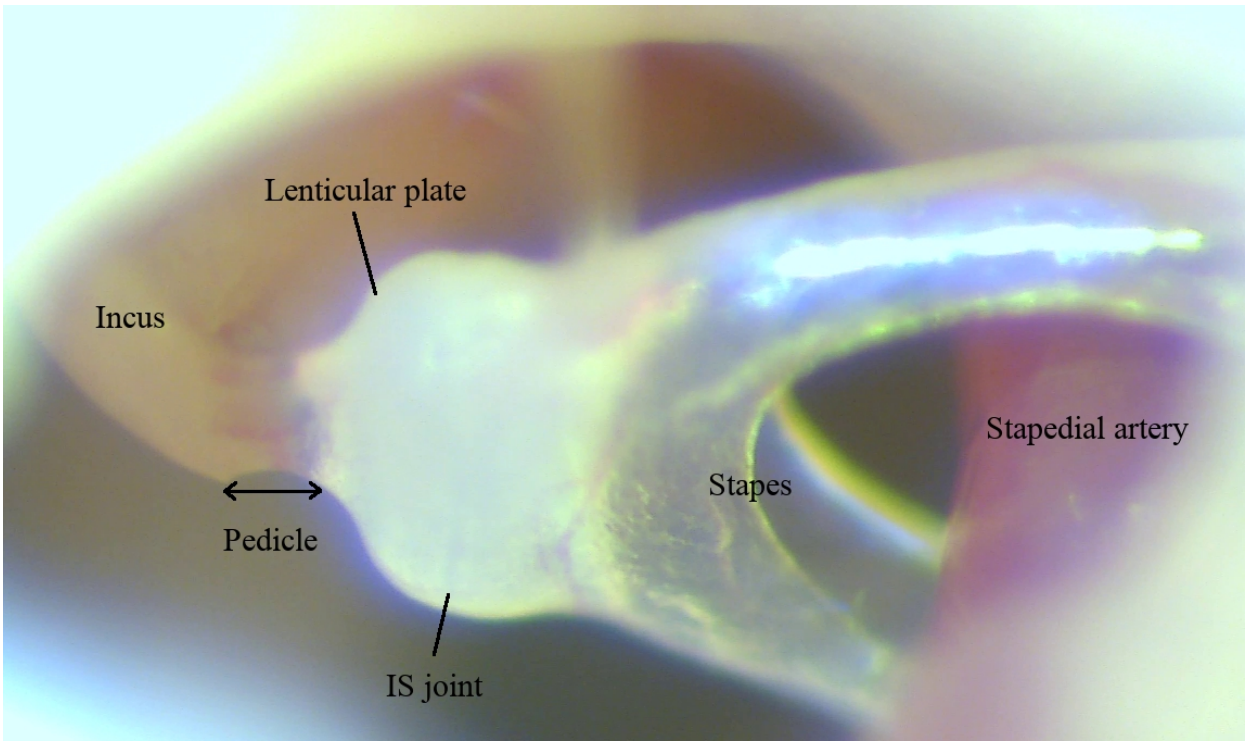

Figure 2.4: The gerbil lenticular process and stapes in their natural undisturbed condition in a gerbil, recorded with a stereoscopic microscope.

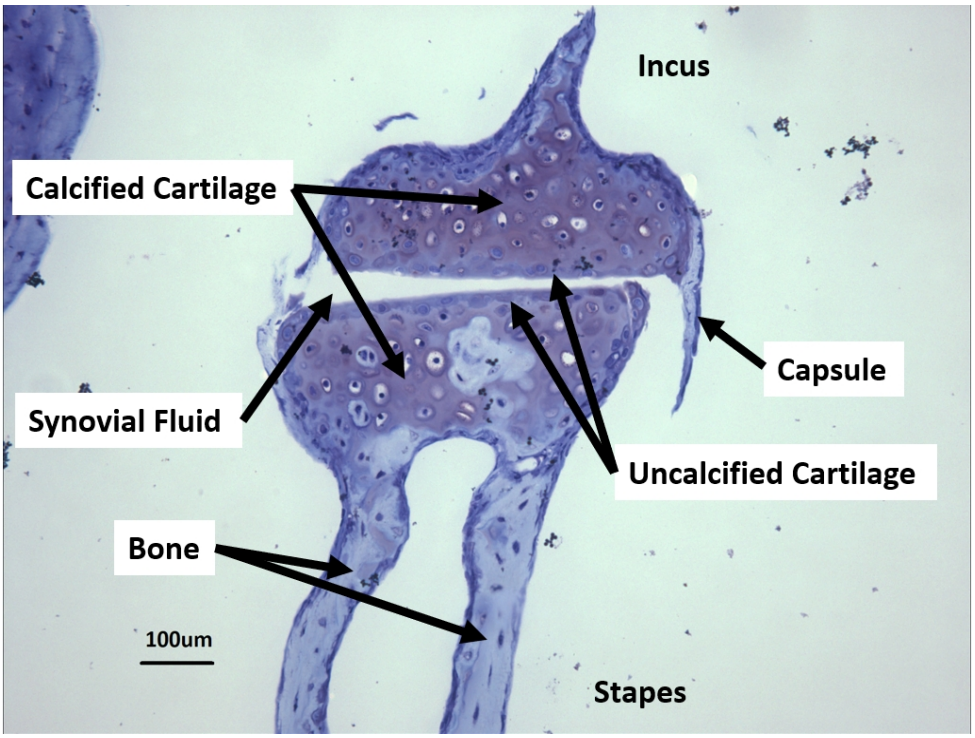

Figure 2.5: Histological section of the gerbil IS joint. The capsule is broken and the joint is dislocated. (Histological material courtesy of M. von Unge)

Karmody et al. (2009), after studying 86 human temporal bones, pointed out that four layers of an articular joint can be found in the human IS joint, namely, superficial, transitional, deep, and calcified cartilage layers. The joint capsule is composed of collagen and elastic fibres extending from the lenticular process to the head of the incus (Ogando et al., 2013).

The stapes (the red structure in Figure 2.2) is the smallest bone of the body and is the last in the ossicular chain. It has four parts: a head, two crura, and a footplate. The head of the stapes branches into the anterior and posterior crura, and they are attached to the footplate. The head of the stapes articulates with the LP and forms the IS joint. The footplate is attached to the oval window of the cochlea by the stapedial annular ligament ((3) in Figure 2.2). Another attachment is the stapedial muscle tendon connecting the head of the stapes, close to the IS joint, to the bulla wall (e.g., Buytaert et al., 2011).

2.2.3 Gerbil inner-ear anatomy

The inner ear is the liquid-filled part of the peripheral auditory system, and converts vibrations into nerve action potentials. It is connected to the middle ear through the oval window. It has three main components: the vestibule, semicircular canals, and cochlea. The vestibule is located medial to the oval window and contains the utricle and saccule which detect head tilting in the horizontal and vertical planes, respectively. Posterior to the vestibule are the semicircular canals, which detect angular acceleration. The cochlea is a snail-shaped organ, anterior to the vestibule, which receives the vibrations transmitted by the middle ear and converts them into electrical impulses.

2.3 Methods of imaging

Early middle-ear FE models were made based on average shape measurements, with simple geometrical shapes for the TM and the ossicles (e.g., Funnell et al., 1978; Williams et al., 1990; Lesser et al., 1991; Wada et al., 1992; Ladak et al., 1996; Blayney et al., 1997; Eiber et al., 1999; Prendergast et al., 1999; Koike et al., 2002). To bring the mechanical behaviour of the models closer to reality, the geometry should be based on details of an individual sample. In order to do that, a set of cross-sectional anatomical images is usually needed. Obtaining such data is challenging.

The middle ear is a complex structure consisting of both soft and hard tissues with tiny dimensions, such as ligaments and bones. Due to the limitations of each imaging modality, such as the spatial resolution and the ability to visualize hard and soft tissues, accurate information about the anatomy requires multiple imaging methods. In this section, we will individually review the main imaging methods that have been employed to acquire such images by first briefly explaining each imaging method, then mentioning middle-ear studies in which it has been used, and then pointing out its strengths and limitations. An important note is that there have been

many finite-element studies of the middle ear, but they mostly used previously obtained scans to generate their models. We only include studies that acquired a new set of images and used it to develop their models.

2.3.1 Histology

The following paragraph is based largely on Wolfe (2019). Histology is a powerful method to study components of a tissue at a cellular level. In histology, a tissue is cut into very thin sections that are then examined by an observational tool such as a microscope. This process requires a procedure to prepare a specimen for the accurate thin cuts. The specific details of the tissue-processing procedure depend on the specimen and the type of the observation, but there are common steps for the tissue preparation, namely, fixation, dehydration, clearing, infiltration, and embedding. The fixation is used to cross-link amino groups in proteins in order to preserve the structural integrity of the cells and tissues. Aldehyde fixatives are most widely used in light microscopy and glutaraldehyde for electron microscopy. The dehydration step, which is mostly done using ethanol, removes the residual fixative as well as the cellular water. Clearing reagents dissolve lipids of tissues and make their components receptive to the infiltration medium. Xylene is the most commonly used clearing agent. After clearing, tissues are infiltrated with a material which displaces the clearing agent and then solidifies to support tissues, allowing thin sections of tissues to be cut. Paraffin wax, agar, gelatin, celloidin, and epoxy resin are examples of the materials used for infiltration. An optional step before sectioning is embedding, in which tissue blocks are made by using an external support medium to facilitate sectioning. After the embedding, tissues are ready for sectioning at a thickness that depends on the purpose and the tool that is used. To provide better discrimination of the sliced-tissue components, usually each slide is stained with a dye that acts as a marker to label a specific type or types of tissue. Comprehensive details of tissue processing for histology are available in Bancroft (2018).

Some early middle-ear models, in which their geometries were generated from an actual sample, used this method. Funnell et al. (1981) derived the shapes of the cat's ossicles from histological sections for a finite-element model, and later the 3-D shape of the malleus was reconstructed, using plastic-embedded sections of a cat middle ear, to investigate manubrial bending (Funnell et al., 1992). Sun et al. (2002) generated a middle-ear model including the ligaments and muscle tendons from 20-μm human temporal-bone sections. Gan et al. (2002, 2004, 2006) used a set of 20-μm sections of the temporal bone in three studies in which the ear canal and the middle-ear cavity were also included. In addition to using reconstructed models for finite-element analysis, Wang et al. (2006) generated a detailed 3-D model of the ear as a teaching tool. Rau et al. (2013) proposed a tissue-preparation method for the histology of the ear, in which they used epoxy resin as the embedding material, and a registration algorithm based on detection of artificial markers made in the samples, to eliminate the misalignment of the images taken from sections of a sample. A recent high-resolution sectioning method was published by Bradel et al. (2017) in which an undecalcified ear was embedded in epoxy resin and sectioned using a microgrinding method that allowed them to remove 35 μm of a sample per grinding run, and in total 20996 histological images were taken with different magnifications showing small details in the middle-ear structures.

Histology is still being used because of its strong ability in visualizing different tissue types, and the capability of having high-resolution images using light and electron microscopy. Apart from its destructive nature, the main disadvantage is its geometrical inconsistency between slices of a specimen. These distortions are caused by the tissue-processing and sectioning steps which cause wrinkles, strains, and shrinkage. Additionally, it is a laborious and time-consuming procedure (e.g., Vogel & Schmitt, 1998). Examples of histological sections of the middle ear are presented in Figure 2.6.

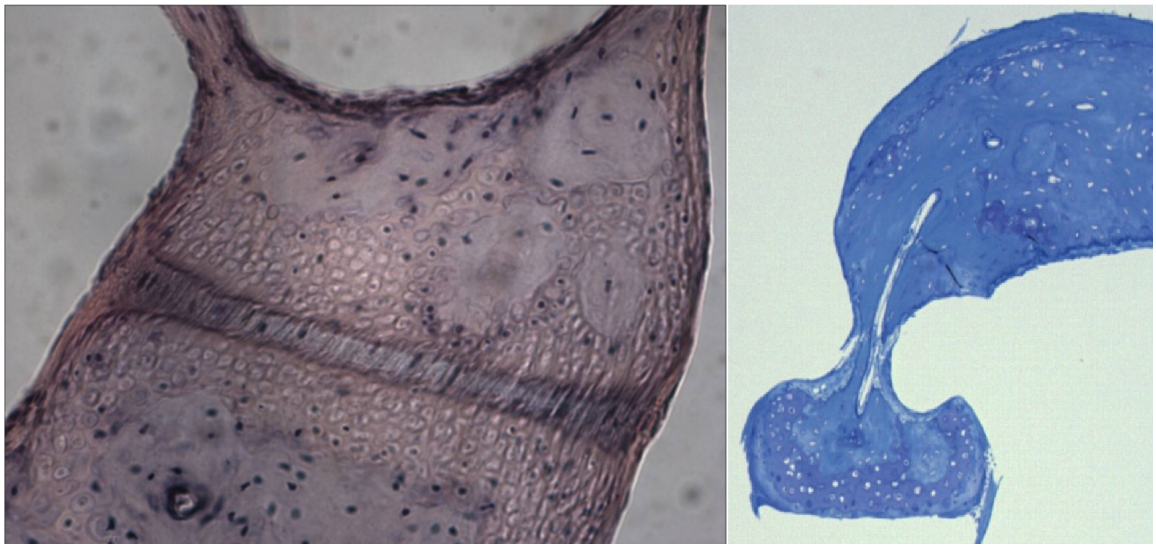

Figure 2.6: Histological section examples. Left: human stapedial annular ligament, right: cat lenticular process (Source: http://audilab.bme.mcgill.ca/AudiLab/teach/me_saf/me_saf.html, accessed on: July 19th 2019).

2.3.2 X-ray computed tomography

X-rays are high-energy electromagnetic radiation with a wavelength from 0.01 to 10 nm. X-rays are either absorbed or scattered by matter; the higher the atomic number, the more X-rays are absorbed (Bushberg et al., 2011). Medical imaging utilizes this principle to get information about the internal organs of the body. Tissues containing more calcium atoms, such as bones, absorb more X-rays, while scattering is the predominant interaction between soft tissues and X-rays. In the process of imaging, the body is exposed to X-rays produced by an X-ray tube. Incident X-rays are differentially attenuated by anatomical structures in the patient. A small fraction of the X-ray beam passes through the patient unattenuated and is recorded on the radiographic detector. In other words, X-ray shadows of the patient's anatomy are projected onto the detector. In addition to this absorption-based method, phase-contrast imaging is also sometimes used. In this method, instead of recording attenuated signals, the X-ray phase shift that is caused by the sample is recorded. To make these phase shifts detectable, the detector is placed at a distance from the sample which allows the phase-shifted beam to interfere with the original beam and produce measurable fringes in the image. These fringes are produced at the boundaries

and surfaces of the sample structures. Detailed information about X-ray-matter interaction and its application in medical imaging can be found in (Bushberg et al., 2011).

3-D computed tomography (CT) produces a set of cross-sectional images of a tissue reconstructed from multiple 2-D projections. In X-ray CT, 2-D projections of an object from different angles are taken by rotating either the object, or the X-ray source and detector positioned on opposite sides of the object. The pixels of a cross-sectional image of the object are the average X-ray attenuation levels of the object in the corresponding locations of the cross-sectional plane. Each of the pixel values is determined by a reconstruction algorithm which uses the information of the pixels in the set of 2-D projections. More information about X-ray CT and the reconstruction algorithms can be found in Herman (2009). Micro computed tomography (microCT) is based on the same principle as is used in X-ray CT, but a micro-focused X-ray source illuminates the object and a very high-resolution detector is used.

Synchrotron radiation (SR) sources are also used in CT. In the process of producing X-rays in these sources, first a beam of electrons is accelerated in an electromagnetic field. Then, these high-energy particles are channelled into another component of the SR generator which supplies the strong magnetic field needed to convert the high-energy electrons into X-ray photons. The X-rays produced are very intense, collimated, narrow-bandwidth and tunable photon beams. These advantages offer much shorter scan times, no beam-hardening artifacts, higher spatial resolution, and reduced background signal (Thompson et al., 1984). The problem with synchrotron X-ray CT is that, due to the costly construction of the very large instruments, the accessibility to these sources is very limited.

The middle ear is mostly composed of bone which provides the best tissue contrast in X-ray scans. Moreover, the ability of microCT in achieving high spatial resolutions makes it the most frequently used method for middle-ear imaging. Clinical CT of the middle ear has been employed for many years for diagnosis, surgical planning, and teaching. These scans were mostly

used for volume and surface rendering, in which a stack of X-ray images was shown as a volume without any segmentation of different structures (e.g., Howard et al., 1990a, 1990b; Egolf et al., 1993; Himi et al., 1996; Reisser et al., 1996). Although clinical CT scans lack anatomical details due to the low spatial resolution, there have been studies that used these scans for developing 3-D models. Rodt et al. (2002) proposed a method to generate 3-D models of the individual middle-ear bones using clinical CT. Later, models based on clinical CT were used for finite-element analysis of the middle-ear components (Lee et al., 2006; Qi et al., 2006, 2008; Wen et al., 2006; Chou et al., 2011; Motallebzadeh et al., 2017a, 2017b).

Most finite-element studies have used microCT scans, in which the spatial resolution is high enough to visualize the details of the structures. This method is only applicable for post-mortem studies in which a sample-preparation step is necessary. Tissue preparation for a microCT scan may include tissue fixation with a chemical fixative (e.g., formaldehyde, 4% paraformaldehyde (PFA) in phosphate-buffered saline (PBS), or glutaraldehyde), and then dehydration in a step-wise process from low to high concentrations of the ethanol to avoid high degrees of tissue shrinkage. The first microCT scan of the middle ear, by Vogel (1999), was taken by a custom-made microCT scanner. He published a scan of a human temporal bone with 60 μm spatial resolution, and later with 10 μm voxel size (Vogel & Schmitt, 1998; Vogel et al., 2000) using an SR CT. The first middle-ear model that used geometries based on microCT images, of cat and human temporal bones, were presented by Decraemer et al. (1999, 2000; 2002, 2003). Since then, most middle-ear models have been developed based on microCT scans alone, or a combination of microCT and other imaging methods such as histological images. To categorize microCT studies, we have divided them based on the imaging methods: regular microCT, microCT with a contrast agent, SR CT, and SR phase-contrast CT.

'Regular' microCT involves scanning a sample prepared with the above-mentioned tissue-preparation method. A noticeable difference between studies is the spatial resolution. For human temporal-bone studies, the resolutions were 20 µm (Lane et al., 2004) and 12.5 µm (Sim et al., 2007). For animal studies, the spatial resolutions were 5.5 µm (Elkhouri et al., 2006), 19.5 µm (Lee et al., 2010), and 12.5 µm (Puria & Steele, 2010). Also, in a multi-species study, Salih et al. (2012) scanned each sample with a different resolution: rat 5.6 µm, gerbil 8.5 µm, rabbit 10.7 µm, cat 23.7 µm, juvenile human 33.5 µm, and adult human 34.4 µm. An example of a microCT scan of a gerbil ear is shown in Figure 2.7.

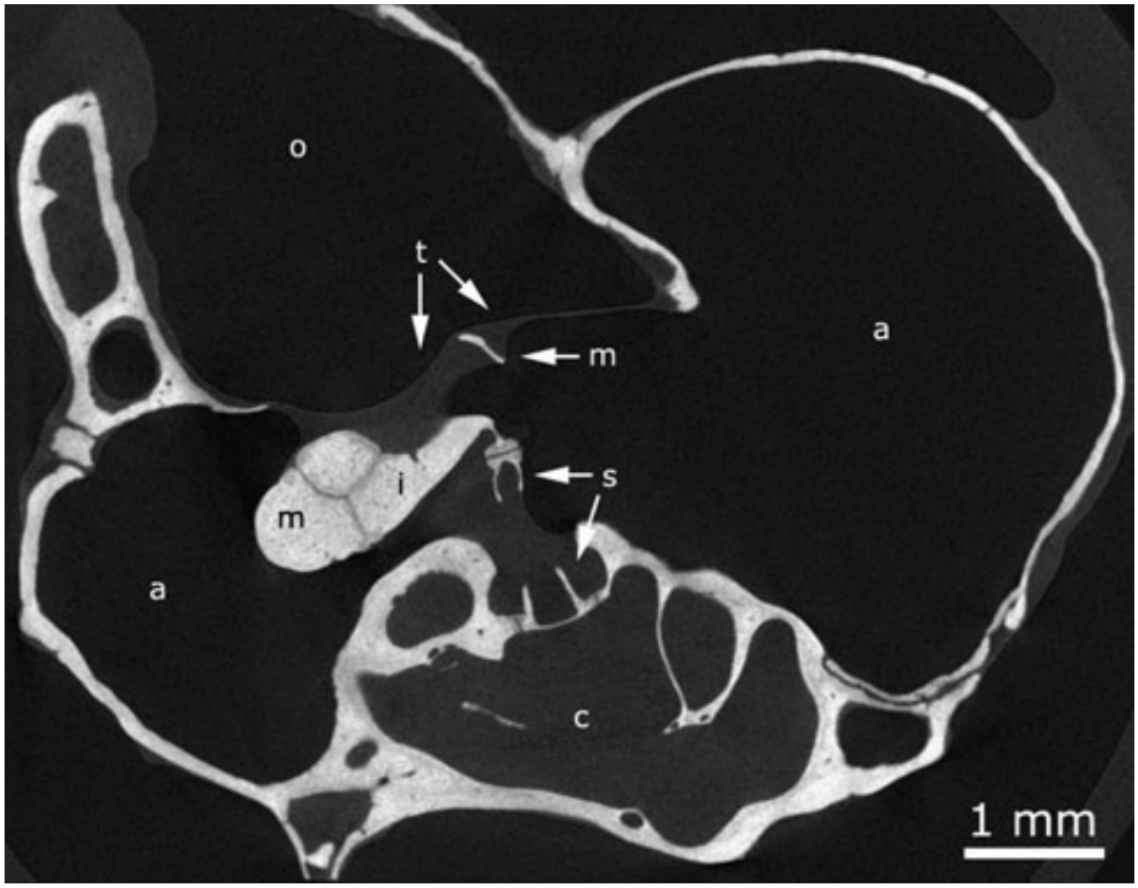

Figure 2.7: Reconstructed microCT cross section of the gerbil ear. (a) middle-ear air cavity, (c) cochlea, (i) incus, (m) malleus, (o) outer ear canal, (s) stapes, (t) tympanic membrane. (Buytaert et al., 2011)

An important disadvantage of X-ray scans is the poor visualization of soft tissues. To address this issue, samples can be stained with a contrast agent which penetrates soft tissues and makes them visible under X-rays. A number of contrast agents have been proposed for X-ray

microCT by Metscher (2009). In middle-ear studies, Buytaert et al. (2014) used phosphotungstic acid (PTA) and iodine-based contrast agents to quantitatively compare the shrinkage of a sample undergoing tissue-preparation processes in microCT and light-sheet microscopy. Later, Greef et al. (2015) scanned six human temporal bones stained with PTA, and proposed a 3-D model of the middle ear based on their scans. Figure 2.8 shows the results of their comparison between stained and unstained scans of the same temporal bone. The voxel size for five of those samples was 22.8 µm and for one of them was 18.5 µm. Rohani et al. (2016) investigated the efficiency of iodine potassium iodide (IKI) to visualize soft tissues in six human temporal bones with 20-µm scans.

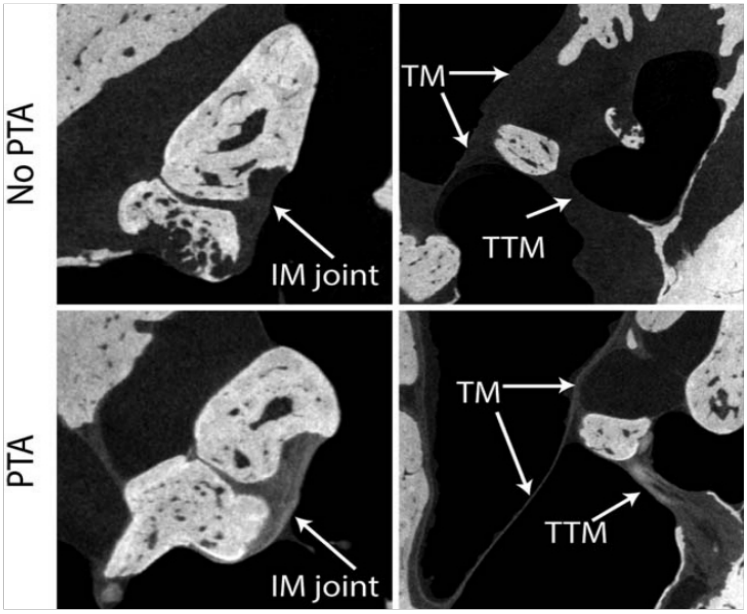

Figure 2.8: Comparison of soft-tissue contrast in microCT images of the same temporal bone sample (Greef et al., 2015).

In addition to the first SR-CT studies by Vogel et al. (1998; 2000) that was mentioned earlier, Neudert et al. (2010) evaluated the bone-implant contact surface of stapes and titanium prostheses, and Kanzaki et al. (2011) studied the cartilaginous components of the ossicles in osteopetrotic mice using this method.

SR phase-contrast CT imaging was used by Elfarnawany et al. (2017) to image hard and soft tissues. In contrast to the conventional absorption-based imaging, soft tissues are

distinguishable in SR phase-contrast CT, since the boundaries of the soft tissues cause a phase shift in X-rays. An example of their results is presented in Figure 2.9.

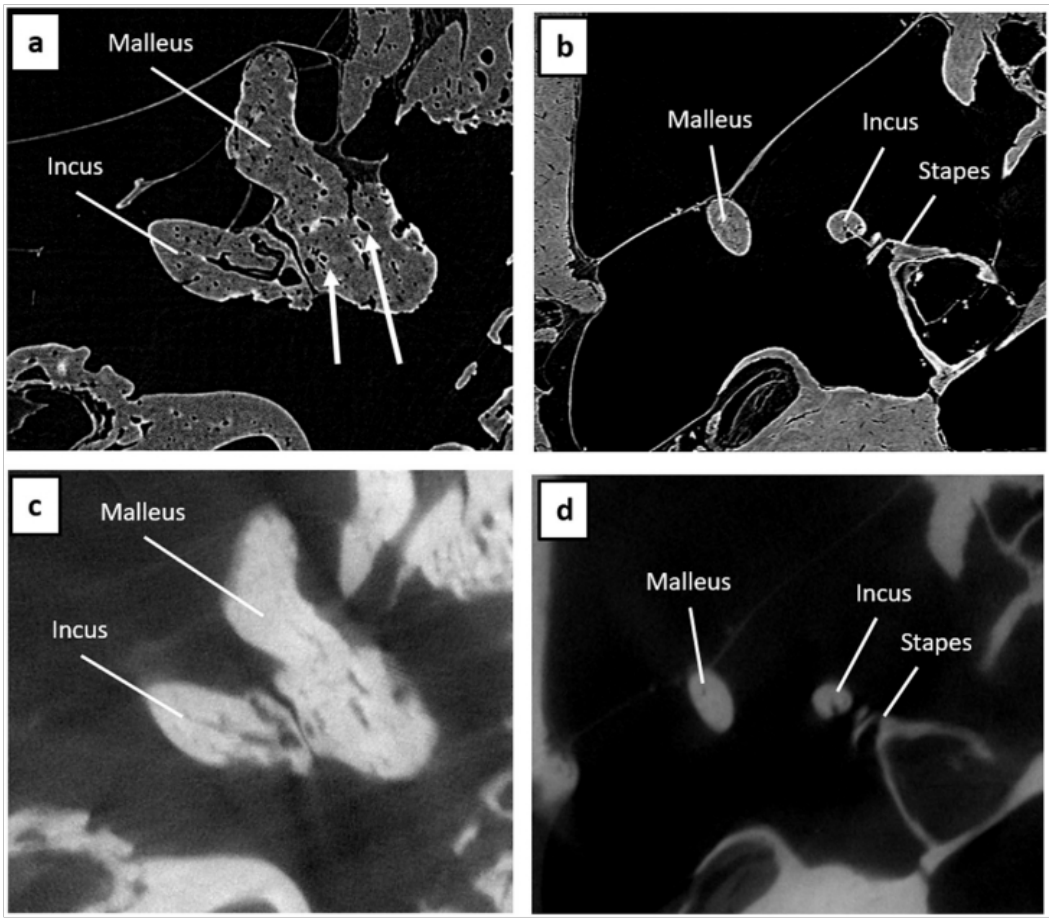

Figure 2.9: Comparison of middle-ear ossicle visualization using SR phase-contrast imaging and microCT (Elfarnawany et al., 2017). a and b were acquired using SR phase-contrast, compared with their corresponding slices in c and d taken by conventional microCT.

X-ray CT scans provide rich information about the structures of the middle ear. Benefiting from its advantages of having the best contrast for hard tissues, and achieving high spatial resolutions, models can now have geometries very close to the reality in terms of bone structures. The main issue, though, is its relatively poor contrast for different types of soft tissues, to make them completely distinguishable from one another, even after using contrast agents and phase-contrast imaging.

2.3.3 Magnetic Resonance Microscopy

The physics of magnetic resonance imaging (MRI) was described in 1946 by Felix Bloch and Edward Purcell. The foundation of MRI is nuclear magnetic resonance (NMR). In this phenomenon, hydrogen atoms align in the presence of a strong static magnetic field and start precessing, which means that, in addition to the natural spinning of the nucleus around itself, the orientation of the rotation axis changes in a circular path with the specific Larmor frequency. By introducing energy in the form of an oscillating magnetic field (as radio-frequency (RF) pulses) with the same Larmor frequency, the hydrogen atoms start resonating, absorbing the energy of the RF pulses, resulting in raising the hydrogen atoms to an excited state. When the RF pulses are stopped, the excited atoms release their energy in the form of decaying RF waves and return to their resting state. These NMR signals are recorded by RF detectors. Since the human body is mostly composed of water molecules comprising hydrogen and oxygen atoms, the NMR signals can give us information about the components of a tissue. There is a different number of hydrogen atoms in a volume of a tissue based on its type, which consequently produces different NMR signals. In MRI, the body is divided into small volumes of tissue and the NMR signal is measured for each one of them, and a 3-D scan of the body is obtained by reconstructing these measurements. Magnetic resonance microscopy (MRM) is based on the same principles of MRI. The difference is in the instruments that are needed to detect very weak RF signals emitted by a small volume of tissue at microscopic levels. In MRM scanners, an ultra-high magnetic field is used to achieve a high signal-to-noise ratio (SNR) of the NMR signals. Also, to avoid the increased field inhomogeneity due to the high magnetic fields, the MRM scanner chambers are usually small, with dimensions of about a centimetre. More information about MRI physics can be found in Callaghan (1993).

As mentioned in the last section, the middle ear is mostly composed of bones, so it does not provide enough contrast in MRM, since the calcium atoms are NMR-inactive, and there is a small number of hydrogen atoms in bones. Most MRM scans of the ear have been used to investigate the inner-ear components, since it is filled with liquids. The first MRM scan of an ear was the inner ear of the mustached bat, published by Henson et al. (1994) with 25 μm voxel size. Later, a gerbil middle-ear scan with 45-μm voxel size was presented by Henson et al. (1999) and used in Funnell et al. (1999, 2000, 2005) to generate a model of the ossicles for finite-element analysis. Other studies have also used MRM for inner-ear research (e.g., Ghiz et al., 2001; Silver et al., 2002; Lane et al., 2005).

MRM principally is capable of visualizing soft tissues better than microCT, but its resolution limitation does not allow us to have such detailed images of the middle-ear soft tissues. Therefore, it is mostly used together with other imaging modalities such as histology and microCT.

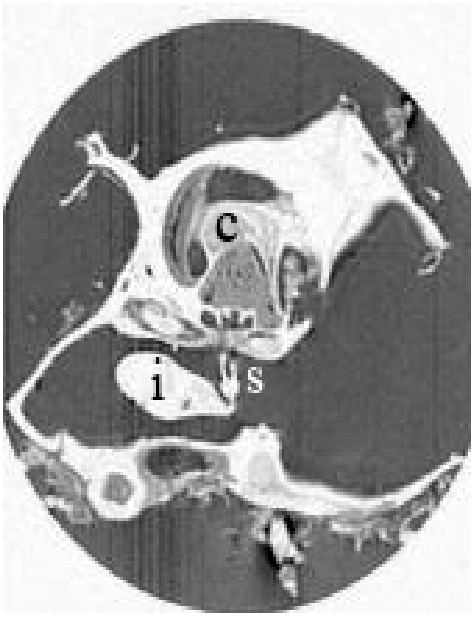

Figure 2.10: A cross-section of an MRM scan of the gerbil middle ear. (i): incus, (s): stapes, (c): cochlea. (Henson et al., 1999)

2.3.4 Orthogonal-plane fluorescence optical sectioning

In conventional transmitted-light microscopes, the sample is placed between the objective lens and the light source, and the transmitted light illuminates the whole sample. The principle of planar-illumination microscopy is to make a thin sheet of light, perpendicular to the observation direction, to selectively illuminate a very thin slice of the sample. In the early versions of these microscopes, white light was used as the light source, but later they were modified to have lasers, giving orthogonal-plane fluorescence optical sectioning (OPFOS). To make the thin layer of light, an additional illumination objective is needed, designed in such a way that it creates the sheet of light in the location exactly corresponding to the focal plane of the objective lens. Besides the spatial resolution, another important parameter in planar microscopy is the thickness of the sheet of light, which determines the imaging depth and affects the clarity of the images. More information about planar-illumination microscopy can be found in Huisken (2006).

Unlike microCT and MRM, in which the sample-preparation step is usually simple, an almost perfectly transparent sample is required to obtain clear images in OPFOS imaging. To become transparent, a sample undergoes an elaborate tissue-processing procedure which either just removes the opaque components of the sample or replaces them with transparent materials. Different tissue-processing approaches have been proposed based on the contents of a tissue. For the middle ear, the most important step is removing the predominant calcium atoms found in the bones that strongly scatter light.

The first use of OPFOS for the ear was by Voie et al. (1993), for the guinea-pig cochlea. It was later used for the middle and inner ear (Voie, 2002). The tissue-clearing process used in the first study was perfusion fixation using buffered formalin; decalcification by ethylene-diaminetetraacetic acid (EDTA); dehydration in ethanol with an increasing concentration of 25%, 50%, 75% and 100%; tissue clearing with Spalteholz fluid (a 5:3 solution of methyl salicylate

and benzyl benzoate); and staining with rhodamine isothiocyanate (RITC) in ethyl alcohol as a fluorescent dye. In the second paper, the ear was treated similarly, with the addition of the use of microwaves for the enhancement of the decalcification. The thickness of the light sheet in both studies was 16 µm. Buytaert et al. (2007, 2009) applied OPFOS to image the gerbil middle ear with a 2-µm sheet of light. The tissue-clearing procedure was similar to that of the previous studies, except for an added decolourization step (in 5% hydrogen peroxide) of the ear canal, which is naturally stained with pigments that absorb light. In their 2009 paper, they also included a 3-D reconstruction of the whole middle ear. Buytaert et al. (2011) used the same method to merge the data of OPFOS microscopy and microCT of the same sample to obtain a complete gerbil middle-ear model including the soft and hard tissues. Figure 2.11 is an example of their results.

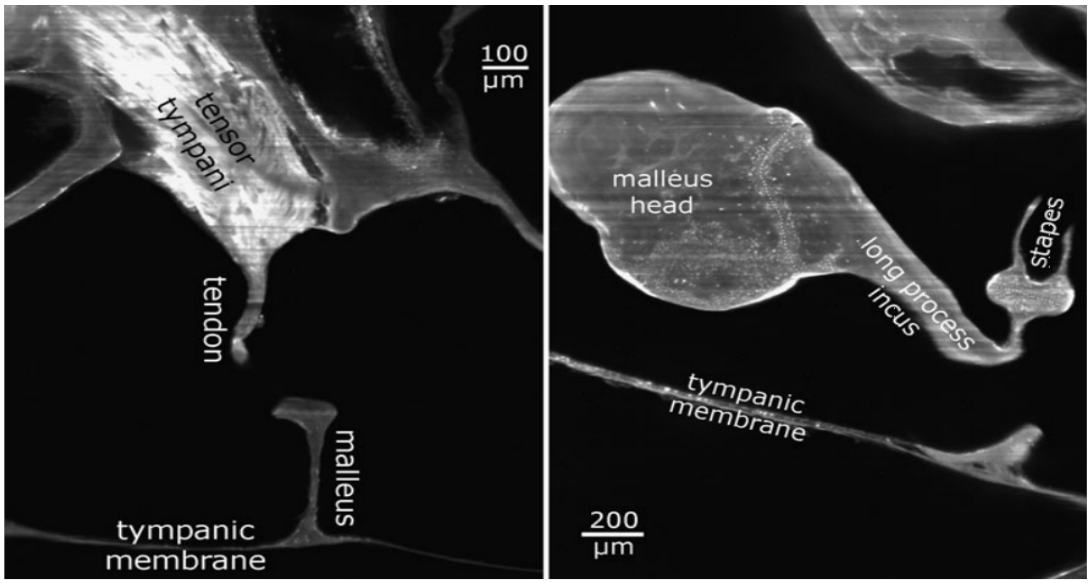

Figure 2.11: OPFOS cross-sectional images of the gerbil middle ear. Two slices of the sample showing the tensor tympani on the left, the ossicles on the right. (Buytaert et al., 2011).

OPFOS microscopy visualizes both soft and hard tissues with a good spatial resolution and details, but the downside is its elaborate tissue-clearing process which causes shrinkage and small structural changes.

2.4 Methods of measuring static deformations

In the last section, we reviewed imaging techniques that have been used to obtain the geometry of the middle ear for finite-element modelling. To evaluate these models, we need accurate experimental data for middle-ear behaviour, such as the displacements of the ossicles and the deformations of the TM as a function of pressure. The first reports of middle-ear behaviour relied on qualitative observations made by simple tools such as a light microscope, but after improvements in the measurement tools, several experimental approaches have been proposed to gain quantitative information. In this section, we will explain the basics of methods that have been used to measure displacements of the ossicles and TM deformations under static pressures.

2.4.1 Radiography

Hüttenbrink (1988) was the first to describe the motions of the ossicles under static pressures quantitatively by using a radiographic magnification technique. He reported one- and two-dimensional displacements of certain landmarks placed on the ossicles in 25 fresh human temporal bones. His experiments were performed under static pressures ranging between −400 and +400 Pa. He concluded from his measurements, among other things, that the LP and stapes have predominant inward/outward motions.

2.4.2 Moiré interferometry

Moiré interferometry has often been used to study TM deformations (Salih et al., 2016). In this method, shadows made by a light source and a line grating are projected on a surface and then observed using either another grating or the same grating, resulting in a pattern called moiré fringes (e.g., Gea, 2012). From these fringes the depth can be calculated and converted into a 3-D height map. This method usually takes several seconds to record a full-field shape of the TM, so

it is usually used for a single pressure step during which the TM shape does not move. In this method, usually a large area of tissue is removed to expose the TM, which introduces problems such as drying of the sample.

Moiré interferometry has been used to measure both shapes and deformations of the TM in human (Decraemer et al., 1991; Dirckx & Decraemer, 1991), gerbil (von Unge et al., 1993; Dirckx et al., 1997, 1998; Dirckx & Decraemer, 2001), and cat (Funnell & Decraemer, 1996; Ladak et al., 2004).

2.4.3 MicroCT

The basics of microCT were explained briefly in the last section. This method has been applied to measure the displacements of the ossicles and the boundary deformations of the TM in human and gerbil under different static pressures (Gea et al., 2010; Gea, 2012). MicroCT scans of the middle ear with about 7-μm spatial resolution were obtained while the ear-canal pressure was maintained at specific values. Later, Salih et al. (2011a, 2011b) proposed a novel X-ray stereoscopic technique to measure average amplitudes of 3-D motions of a marker under quasi-static pressures using X-ray scans. In this method, by recording images of an object from two different angles by spatially rotating it 90°, the average amplitude of a periodic motion of a marker is measurable in 3D. In Salih et al. (2011b), they measured displacements of two points on the gerbil manubrium, and Salih et al. (2016) measured displacements of the ossicles in rabbit and gerbil under quasi-static pressures using this method Salih et al. (2016). In their experiment, the middle ear was subjected to sinusoidal quasi-static pressure signals at amplitudes of ±1 kPa and ±2 kPa for frequencies of 0.5, 5, 10 and 50 Hz. Figure 2.12 shows snapshots of their scans showing positions of the markers.

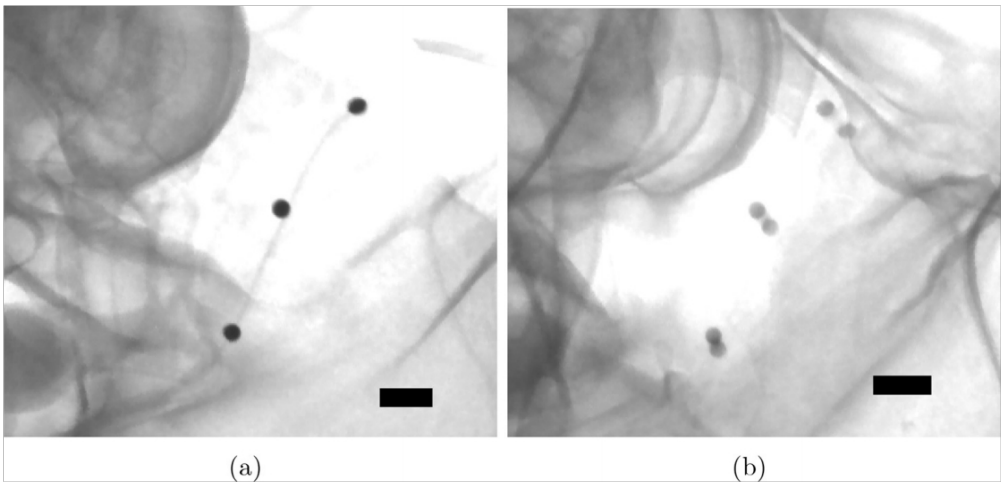

Figure 2.12: Tungsten marker placement on the malleus of a gerbil. Snapshots of: (a) resting state before applying pressure, (b) during pressure loading of the TM with a pressure of 2 kPa (peak-to-peak) at 50 Hz. (Salih et al., 2016).

Chapter 3. Methods

3.1 Introduction

The objectives our project were to measure displacements of the LP and stapes under static pressures, and to observe changes in the IS joint, also under static pressures. We designed our experiment to collect our data in two stages using instruments introduced in Section 3.2. An experiment for measuring the displacements of the LP and the stapes is described in Section 3.3, followed by a procedure for microstructural examination of the IS joint in Section 3.4. The details of the algorithms and methods that were implemented to extract information from the collected data are described in Section 3.5.

3.2 Devices

In this study we used a pressurization system, a stereoscopic microscope, a nanoCT scanner, a light-sheet microscope, and tissue-clearing equipment. We will introduce each of these instruments in this section.

3.2.1 Pressurization system

A pressurization device was used to simulate the static pressures in the ear canal that are found in daily life and, more important, in hearing screening tests such as tympanometry, as introduced in Chapter 1. We used a custom-made pressurization system consisting of hardware components, which produce and sense pressures, and software, which controls these components. This device was initially implemented as a student project (Ding, 2011), then enhanced by Shapiro (2014) and then later by Kose (2017, 2019). We also made several improvements in this device which are described in this section.

3.2.1.1 Hardware components

This system consists of a controller circuit board, a pressure sensor, a DC motor, a peristaltic pump, and an H-bridge motor-driver board. An overview of this system is shown in Figure 3.1.

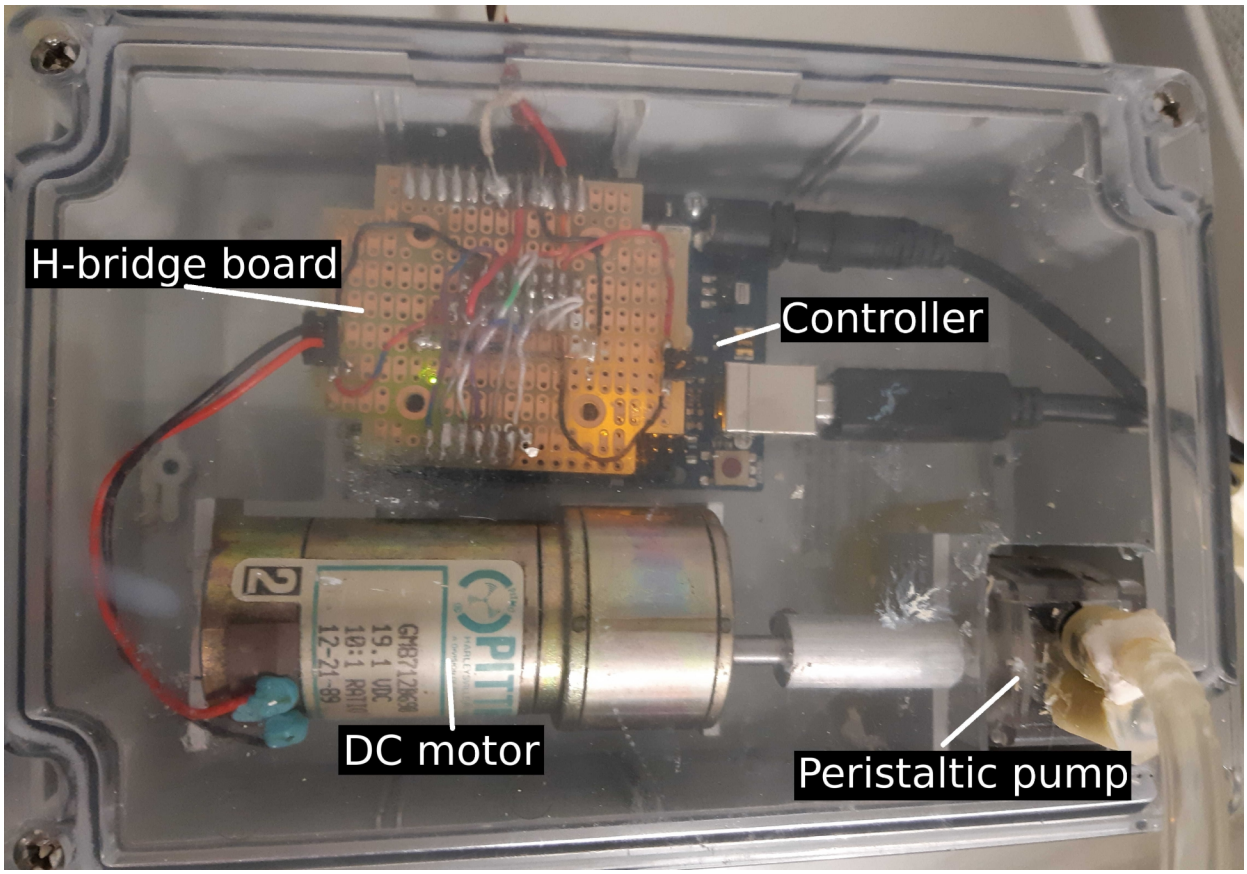

Figure 3.1: Components of the pressurization system used in our study.

The Arduino Uno is a programmable microcontroller-based board that is available as an open-source development kit (SmartProjects, Strambino, Italy, www.arduino.cc). It is equipped with a Microchip ATmega328P microcontroller which executes a user-defined program written in C using the Arduino IDE software.

The pressure sensor used in our system converts the difference between the pressures applied to its two input ports into an analogue electrical voltage. We used a 20 INCH-D-4V sensor (All Sensors, Morgan Hill, CA, www.allsensors.com). Its input pressure range is ±5000 Pa (±20 inH_2O), and the converted analogue voltage ranges from 0 to 4 V. This analogue output is

converted by the Arduino to a digital value between 0 and 1023 units. The value for a zero-pressure difference is 460 units, and the resolution is 12 Pa per digital unit. The reported full-scale linearity is 0.05%. This sensor is illustrated in Figure 3.2.

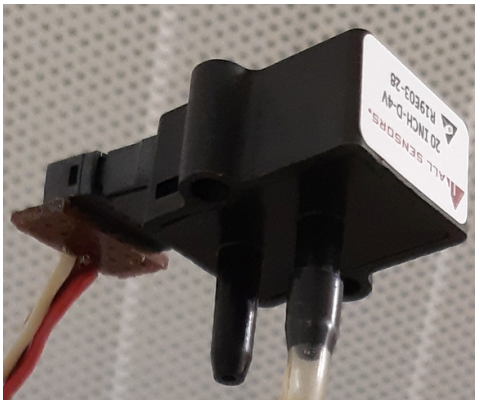

Figure 3.2: 20 INCH-D-4V low-pressure sensor.

A brushless bi-directional DC motor (GM8712D690, Pittman Motors, Harleysville, PA) is used in this system to rotate a peristaltic pump to produce the desired pressures. The speed is controlled by the voltage, with the maximum of 240 rpm achieved at 19 V.

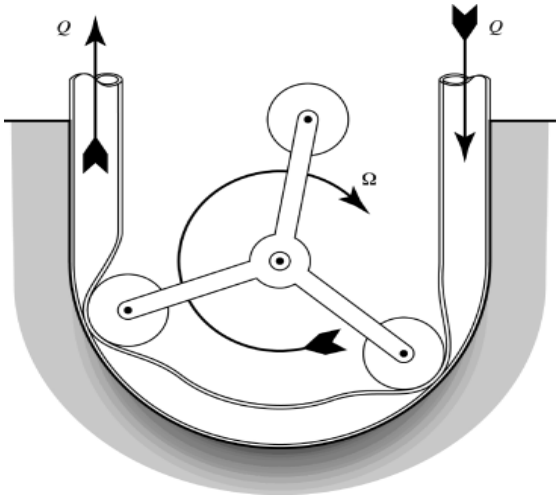

Figure 3.3: Schematic diagram of a peristaltic pump (Berg & Dallas, 2008).

The shaft of the motor is connected to the peristaltic pump, obtained from Caswell Inc. (Lyons, NY), by means of a custom-manufactured cylindrical link. A generic schematic diagram of a peristaltic pump is shown in Figure 3.3. Since it works bidirectionally, it is capable of generating either positive or negative pressures.

The maximum output voltage of the Arduino is 5 V with a low output current that is not enough to run a DC motor operating with a voltage between 0 and 19 V and a current of up to 2 A. An external H-bridge board as the motor driver is connected to the Arduino to supply the motor with adequate power, and to control the direction of its rotation. The schematic diagram of an H-bridge circuit is displayed in Figure 3.4. In this circuit, when the switches S1 and S4 are closed, the motor runs in the clockwise direction, and when S3 and S2 are switched on, it runs in the counter-clockwise direction. S1 to S4 are representations of transistors that function as switches. We used an L298HN integrated circuit (STMicroelectronics, Geneva, Switzerland) as the motor driver.

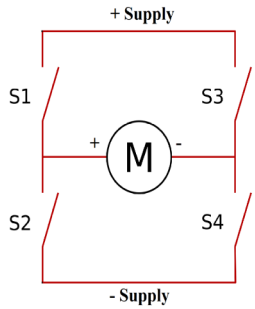

Figure 3.4: Simplified schematic diagram of an H-bridge ("H bridge," 2019).

One of the input ports of the pressure sensor is left open to the ambient pressure, and the other port is inserted into the system. The pressure difference measured by the sensor is fed into the Arduino. In order to change the speed of the pump, which corresponds to the speed of the pressure change, the Arduino uses pulse width modulation (PWM): a rectangular pulse train with a controllable duty cycle is sent to the H-bridge board, a higher duty cycle resulting in faster rotation of the motor. The Arduino also sends the values of the pressure measured by the sensor to a separate computer using a serial connection.

3.2.1.2 Pressure signals

We used two types of pressure signals: a step sequence and a ramp. In the step-sequence pressure signal, the pressure is increased in a staircase fashion with a fixed step size, from zero to a maximum value, while the pressure is maintained at each level for a specific time duration. Then, the pressure is dropped back to zero in the same pattern. After reaching zero, the pressure is decreased to a minimum negative value, followed by an increase to zero, both in the same step-wise pattern. In the ramp pressure signal, the pressure is increased and decreased linearly at a constant rate. Examples of the step and ramp pressure signals are shown in Figure 3.5.

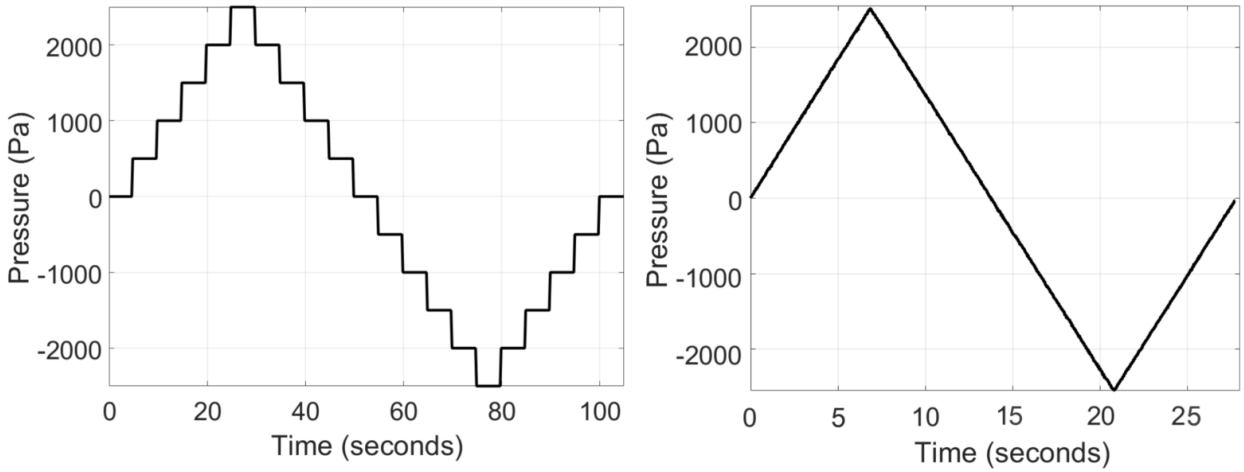

Figure 3.5: Left: an ideal step pressure signal with 500 Pa step size, maximum value of 2500 Pa, and 5 seconds duration time at each level; Right: an ideal ramp pressure signal with a pressurization speed of 360 Pa/s, and a maximum value of 2500 Pa

The part of the signal that starts from zero and ends in either the maximum positive or minimum negative value is called loading, and going back to zero from those values is referred to as unloading. A pressure signal which includes both the loading and the unloading parts for both positive and negative pressures is a full cycle.

3.2.1.3 Connection tubes and buffer volume

In our project, we made the step and ramp pressure signals with different hardware setups. One complete rotation of the motor at full speed causes an immediate pressure change of over

1000 Pa in the volume of the middle ear, which has a volume of about 0.2 ml (Ravicz et al., 1992).

The setup that we used to make a step pressure signal was a 6-mm tube with one end connected to the output of the pump and the other end connected to the pressure sensor. A smaller tube with a diameter of 1 mm was inserted into the middle of the main tube, to be used for the ear-canal pressurization. To seal the connections, we used dental cement.

For the pressure ramps, the peristaltic pump mechanism would cause ripples in the output pressure if the motor worked at low speeds with the same setup that was used for the pressure steps. In order to create smooth ramp pressure signals, a glass bottle with a volume of 150 ml (previously used by Shapiro (2014)) was added to the connections as shown in Figure 3.6. The empty buffer volume helps us to eliminate pressure oscillations, but on the other hand it reduces the highest achievable speed of a ramp signal. With the current setup, ramp signals were produced having pressure rates between 180 Pa/s and 360 Pa/s.

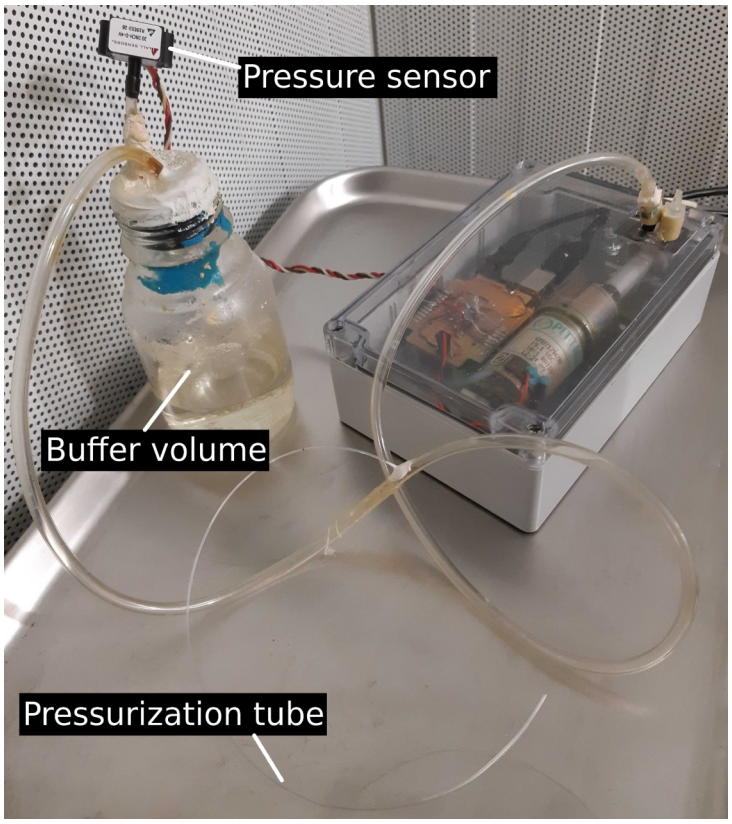

Figure 3.6: Added buffer volume to the pressurization setup.

3.2.1.4 Software

The Arduino controls the pressure production with a user-defined program. It is programmed in such a way that a user can send pressure values and speeds through Python code running on a separate computer, and receives the pressure values measured by the pressure sensor. In this section, the computer and Arduino codes that were used to produce step and ramp pressure signals will be described. The codes for the Arduino and the computer are available in Appendices 1 and 2, respectively.

The Python code establishes a serial connection between the computer and the Arduino to transfer data. The user is asked for the desired type of pressure signal (step or ramp), the maximum value of the pressure, the number of full cycles, and the duration of a delay before starting the pressurization. Also, depending on the selected pressure type, the user is asked for the number of steps between zero and the maximum value and the time duration of each level for the step signal, or for the pressurization speed for the ramp signal. After getting these values, the computer sends them to the Arduino and waits for it to start sending the pressure-sensor values. The computer constantly receives these data from the Arduino, converts them into actual pressure values, and saves the results in a text file, until it gets a flag value indicating the end of the pressurization. The text file containing the pressure values has two columns, the first one being the receiving time of the data, and the second one being the pressure value. To convert pressure-sensor values to pressures, they are subtracted from 460 (digital equivalent of the sensor output at ambient pressure) and multiplied by 12 (the sensor resolution in Pa).

3.2.1.4.1 Step pressure signal generation

The Python code calculates the values of the pressure levels in the step pressure signal based on the maximum value and number of steps entered by the user. It sends each pressure level to the Arduino and then, after waiting for the defined time duration at each level, sends the

next pressure value. The Arduino receives the target pressure and the Start command. The difference between the current pressure (measured by the sensor) and the target value is computed. Then the motor is started at full speed in the direction determined by the sign of the calculated difference. This process is repeated every few hundred microseconds until the pressure difference falls into the tolerance range of ±36 Pa. Then the Arduino sends the Stop value to the computer and turns the motor off.

3.2.1.4.2 Ramp pressure signal generation

Making a ramp pressure signal is not as simple as producing a step since the pressure needs to change at a constant rate. The Arduino changes the speed of the motor using the PWM signal to maintain the rate of the pressure change. In order to achieve an acceptable linear ramp signal, the relationship between the speed of the motor and the rate of the pressure change is estimated, and then it is used in a proportional-integral-derivative (PID) controller implemented in the Arduino.

3.2.1.4.2.1 Pressure speed vs motor speed function estimation

There is an adjustable PWM variable between 0 to 255 that corresponds to the duty cycle (0 to 1) of the generated pulse which controls the speed of the motor. To estimate the relationship between the PWM value and the pressure speed, we programmed the Arduino to start increasing the pressure from 0 Pa for a second with PWM values of 175, 195, 215, 235 and 255, and calculated the speed for each of these values. The motor does not work with values below 175, because of the stiction between the motor shaft and the pump. Based on these measurements, it was determined that every unit increment in the PWM value results in an increase of about 3 Pa/s in the pressurization speed.

3.2.1.4.2.2 PID controller

A PID controller is a simple but effective control-loop feedback method that uses the output error of a system to regulate variables producing the result. It has three functions, namely, proportional, integral, and derivative (Unbehauen, 2009). Each of these functions has a variable referred to as a PID coefficient. A block diagram of a PID controller is depicted in Figure 3.7.

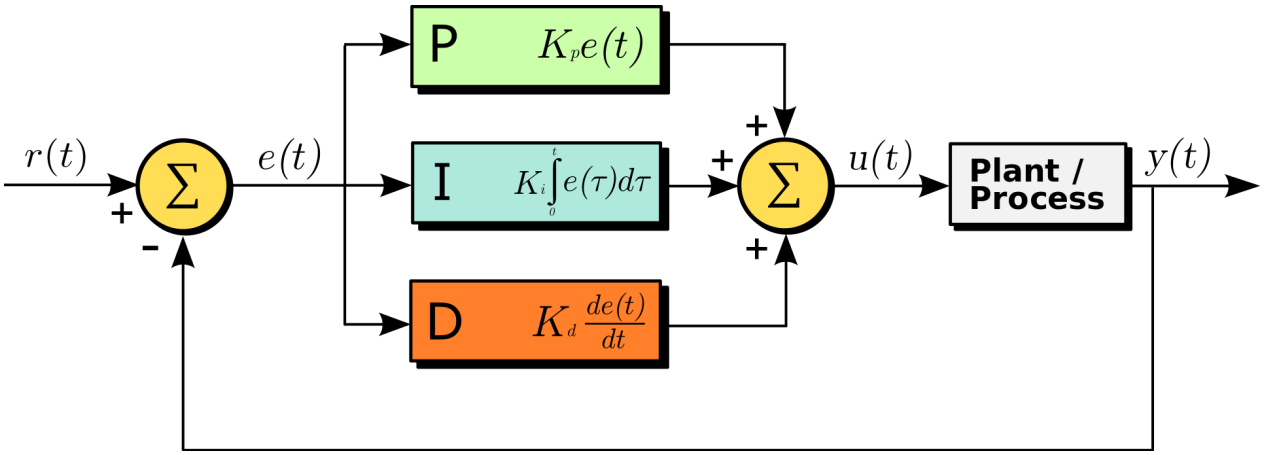

Figure 3.7: A block diagram of a PID controller in a feedback loop. r(t) is the target point, and y(t) is the measured process value. The error functions used to calculate u(t), the PID output, are shown in each box (Source: https://en.wikipedia.org/w/index.php?title=PID_controller, accessed on: 2019 July 23).

In our pressurization system, the error value is calculated by subtracting the defined target speed from the current pressure speed. Due to noise in the system and the resolution limitation of the pressure sensor, using just two consecutive pressure values to calculate the current pressure speed does not give us an accurate value. Therefore, we used an average of the measured pressure values over a time interval as shown in Equation 3.1.

$$speed = \left| \frac{\text{mean}\left(Pressure\right)_{t+\Delta t} - \text{mean}\left(Pressure\right)_{t}}{\Delta t} \right| \tag{3.1}$$

The duration of the time interval Δt affects the performance of the PID controller. A small interval length causes inaccuracy in the speed estimate as mentioned earlier, and a long interval duration, which means a larger pressure change in that specific time, causes poor control with oscillations in the output pressure. Furthermore, there is a range of desired speeds, which means

that in a fixed time interval the pressure changes by different amounts. Therefore, an adaptive time interval is implemented such that its length changes linearly as a function of the speed between about 70 ms for the highest speed (360 Pa/s), and about 200 ms for the lowest speed (180 Pa/s). The highest and lowest values were determined so that the pressure sensor measures at least 2 units (24 Pa) over the time interval. This way, the pressure measurements are more reliable, since the changes are more than the sensor resolution, and at the same time they are small enough to give a good PID performance. The linear function used to determine the length of the interval is given in Equation 3.2. Note that the calculated value is divided by 10, because the pressure measurements are performed every 10 ms.

$$t_{\text{interval}} = -0.07\, speed_{\text{target}} + 33 \tag{3.2}$$

After obtaining the error, the PID output is determined using the proportional, integral, and derivative functions. We used only the proportional and derivative terms of the PID, because when there was an integral term we found that sometimes the output of the integral function became a large negative or positive value due to the summation of the errors over time, and adversely affected the final PID output. In fact, we used a PD controller with function coefficients, K_P and K_d, which were set to 0.5 and 0.05 respectively, determined by running several tests.

The output of the controller gives the amount of the correction needed to be made in the system in order to regulate the speed. By using the relationship between the speed of the motor and the pressure speed that was obtained earlier, the controller output is divided by 3 and then added to the PWM value to correct the motor speed.

In addition to the pressure speed, the Arduino monitors the pressure until it reaches the target pressure, then it sends the Stop flag to the computer and turns the motor off.

3.2.2 Stereoscopic microscope

A stereoscopic or dissecting microscope is a low-magnification optical microscope that has two separate optical paths, with two objectives and eyepieces, to provide a slightly 3-D visualization of the object. Unlike a transmitted light microscope, it typically uses the reflected light from the surface of the sample. The important feature that makes it suitable for our purpose is that it provides a reasonably large magnification at a large enough working distance.

We used a Leica M80 stereo microscope (Leica, Wetzlar, Germany) shown in Figure 3.8 with a 9.6× objective lens and a 10× eyepiece lens, providing 96× total magnification. An external Leica illumination device with two arms was used to provide the light.

Figure 3.8: Leica M80 stereo microscope used in our experiment.

3.2.2.1 Microscope camera

The Leica MC170HD (Leica, Wetzlar, Germany) is a camera that is attached to one of the eyepieces and records videos. It has a CMOS sensor with a resolution of 5 mega pixels and the ability to record videos at 1920×1080 with 30 frames per second and three channels (RGB). It can be connected to a computer via USB to show real-time images and to save videos, or a remote controller can be used directly to record the data on an SD card. We used the controller to record the videos on an SD card, while it was connected to a monitor via an HDMI cable to see the real-time view of the camera. The camera is shown in Figure 3.9.

Figure 3.9: Leica MC170HD microscope camera used in our experiment.

The spatial resolution of the microscope was measured by using a grating slide. We captured an image of a 100-lines-per-mm slide by the camera, and measured a spatial resolution of 0.8 μm per pixel in the focal plane.

Light refraction is the principle underlying the design of lenses. The refractive index that quantifies this phenomenon depends on the wavelength of light. This effect in a lens causes different wavelengths of visible light to converge at different distances from the lens. Since this difference can be several microns, it is more significant at higher magnifications and produces

blurry images with incorrect colours. Achromatic lenses are designed in such a way as to reduce this effect by bringing two wavelengths into focus on the same plane ("Achromatic lens," 2019). In the microscope that we used, an achromatic lens which corrects the focal distances of the red and green wavelengths is used.

3.2.3 NanoCT scanner

We reviewed the fundamentals of X-ray imaging, and studies that employed this method, in Chapter 2 and pointed out that microCT is a popular imaging method in middle-ear studies. The resolution of microCT varies down to about 1 μm. This resolution is enough to investigate most structures in the middle ear, but still not sufficient to study the IS joint in detail. The gerbil IS joint has structures with dimensions of only a few microns, and the resolution of microCT does not allow us to do accurate measurements and observations.

A new type of X-ray scanner has been developed that allows us to reach resolutions of a fraction of a micron. These scanners benefit from lenses that can magnify X-rays, as optical lenses do with visible light (Hunter, 2017). The wavelength of X-rays is shorter than that of visible light; therefore, a special material is used in the X-ray lenses to make X-ray refraction possible.

The imaging parameters of the nanoCT scanner can be adjusted to acquire high-quality scans. Some of its important parameters are: the X-ray source voltage, exposure time, and number of 2-D projections.

The energy of X-ray photons emitted from the source directly affects the contrast of images (Bushberg et al., 2011). If a low-energy X-ray beam is used, most of its photons would be absorbed by the sample, which leads to noisy images. On the other hand, a high-energy X-ray beam passes thorough a sample more easily, resulting in less image contrast. The energy of the X-rays is mainly determined by the source voltage.

Exposure time is the duration over which a sample is exposed to X-rays to acquire a 2-D projection. Longer exposure times allow the detector to receive more photons and form a better image. In the nanoCT scanner that was used in this work, there is a parameter known as *counts* which quantitatively shows the intensity of X-rays received by the detector in different areas of an image. It is recommended by Zeiss to have about 5000 *counts* for each pixel to get high-quality scans. Setting long exposure times makes the whole scanning time longer which leads to specimen deterioration and shifting.

The cross-sectional images of a sample using the nanoCT scanner are reconstructed from 2-D projections with the same algorithms discussed in chapter 2. More 2-D images taken with a small rotation step (0.1125° in our case) make the reconstructed images more accurate and less noisy, but the scan times longer. For our samples, for which the X-ray absorption dose is not important, the costs and time constraints are the reasons for acquiring only a limited number of projections of a sample.

We used a Zeiss Xradia 520 Versa, which can achieve resolutions down to to 0.1 μm.

3.2.4 Light-sheet microscope

The fundamentals of planar microscopy were described in Chapter 2. Over the past couple of years, improvements have been made to such microscopes which have enhanced the resolution and quality of their scans. In the first OPFOS scanners, a single cylindrical lens was used to make and project the light sheet into the sample. A new type of planar microscope has been developed (under the name light-sheet fluorescence microscopy, LSFM) that combines an illumination objective with the cylindrical lenses to refine the properties of the light sheet, particularly its thickness (Allen, n.d.).

We used a Zeiss Lightsheet Z.1 to acquire cross-sectional images of the IS joint with different magnifications. In this microscope, the sample is suspended from the top of a chamber,

submerged into a liquid with the same refractive index as the sample. Two excitation lenses illuminate the sample from the sides, and an objective lens is used for observation. The microscope is controlled using a computer to adjust the sample's location, record the observations, and to change excitation lasers. A 20× objective lens allows users to achieve 0.2 μm resolutions.

3.2.5 X-CLARITY system

A requirement of light-sheet microscopy is a transparent sample. X-CLARITY is a set of tissue-clearing equipment and reagents developed by Logos Biosystems (https://logosbio.com/tissue-clearing_3d-imaging/tissue-clearing/x-clarity). This system consists of two main parts. The first part is a tissue-hydrogel hybridization system to stabilize the structure of a tissue, and contains a hydrogel solution kit, and a polymerization device. The second part is a lipid-removal system which has an electrophoretic tissue-clearing solution, and a tissue-clearing device. This system was primarily developed to clear soft tissues such as brain. The complete original protocol of tissue clearing for a mouse brain is given in Appendix 3. A summary of this procedure is: hydrogel infusion by incubating the tissue in a solution of 10X PBS, acrylamide, and VA-044 for 24 hours and then using the polymerization system; electrophoretic tissue clearing (ETC) by placing the tissue in the ETC system for 24 hours; refractive-index matching by putting the tissue in the solution that will be used for light-sheet microscopy for 24 hours to change the refractive index of the cleared sample to that of the solution.

3.3 Displacement measurement

In order to measure the displacements of the LP and stapes, a new technique was employed that is based on tracking the changes recorded by a camera attached to a stereo microscope. This motion, which mostly takes place in one plane, was captured at a viewing angle

nearly orthogonal to this plane, with a high temporal and spatial resolution. In this section, the animal preparation method and the experiment design to measure these motions is described.

3.3.1 Animal preparation

We used adult male Mongolian gerbils (*Meriones unguiculatus*) provided by Charles River Laboratories (St-Constant, Québec). For the design and initial testing of the experiment setup, we used ten frozen and then thawed gerbils that had previously been used in eardrum vibrometry experiments by Kose (2017), and two freshly euthanized animals. The finalized experimental procedure was performed on two gerbils, G1 and G2 (three ears in total), with body weights of 79.5 and 77.8 g respectively.

Each gerbil was euthanized by anaesthetic overdose with CO_2 gas and then decapitated. Incisions on the posterior side of the ear were made to remove the pinna, cartilaginous ear canal, and soft tissues to expose the opening of the bony meatus and the bulla surface. Two lines indicating the soft-tissue attachments on the surface of the bulla are visible as shown in Figure 3.10.B. These lines divide the bulla surface into three segments that facilitated finding the same location in different ears. Using a drill, a very small hole was carefully made in the most posterior part of the middle segment of the bulla surface. Drilling produces a powder of tiny bone particles that may get into the bulla. To minimize the possibility of this powder entering the cavity, a suction probe was used right next to the drilling location while the hole is being made. Afterward, the middle segment of the bulla surface was carefully removed with tweezers, from the hole made by the drill to the edge of the bony meatus opening, leaving a small bone piece between the hole and the bony meatus opening. This prevented small bone particles from entering the bulla and sticking to the IS joint. Steps in the animal-preparation procedure are shown in Figure 3.10.

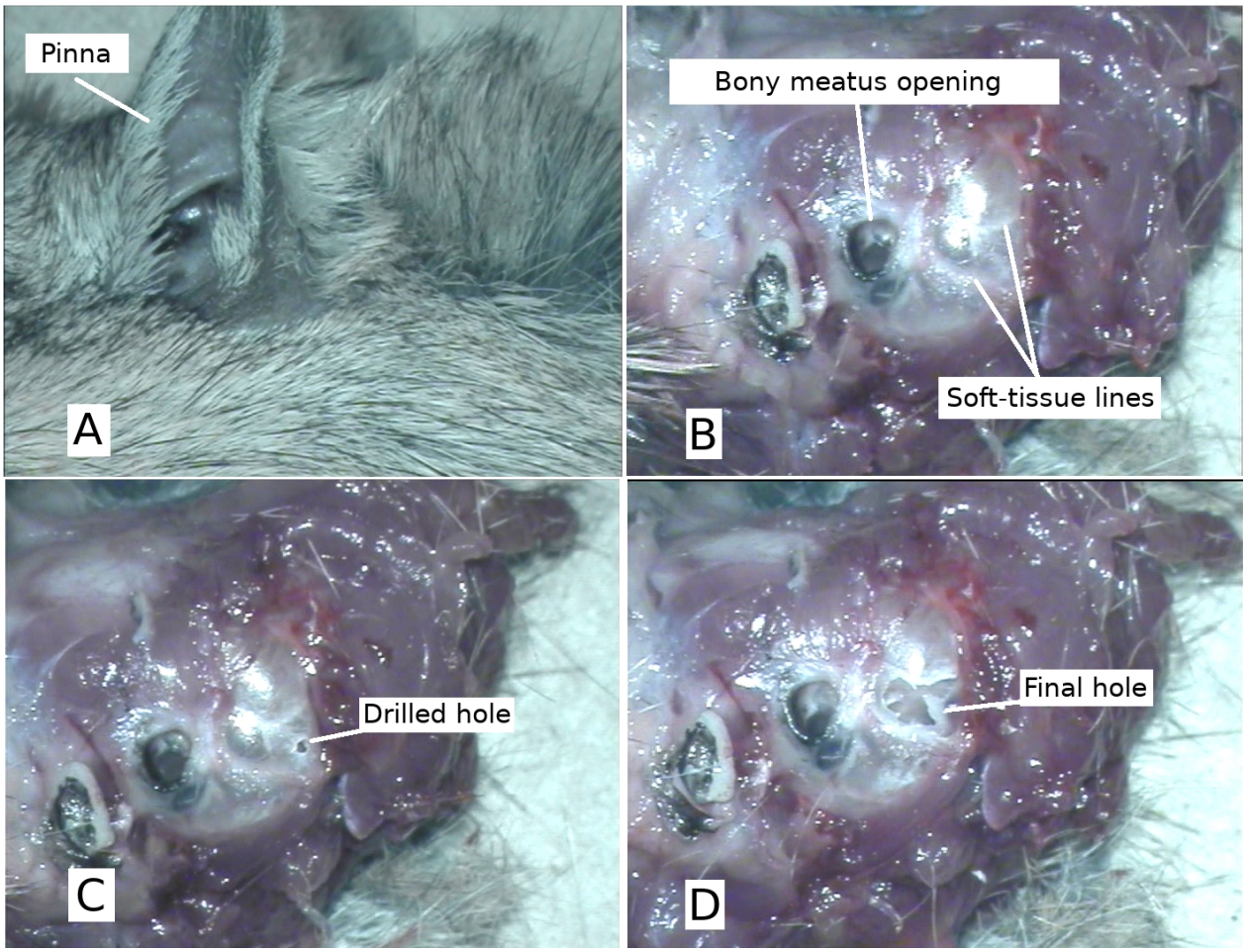

Figure 3.10: Animal preparation procedure. A: Orientation of head. B: Pinna and soft tissues are removed and the bulla is exposed. Two soft-tissue lines are indicated. C: The location of the drilled hole. D: The final hole after removing the middle segment.

After the hole had been made in the bulla, the gerbil head was transferred to a head fixture. During the rest of the preparation procedure, an ultrasound humidifier was used next to the sample to decrease drying of the middle-ear cavity due to post-mortem effects and the opened bulla. Since the middle-ear cavity is open, its pressure is the same as the ambient pressure.

To deform the TM and move the middle-ear structures, the ear-canal pressure was changed using a tube attached to the pressurization system. The ear canal with the inserted tube was completely sealed by applying dental cement. The meatus opening is relatively large; therefore, the dental cement, which is in a liquid form at first then gradually solidifies, might enter the ear canal and touch the TM. To address this problem, sealing the ear canal was done in two steps. First, a layer of dental cement was applied to the surface of the bulla, around the edges of the ear

canal opening. By doing that, a support for the pressurization tube on the edge of the ear canal opening was created, and the ear-canal hole became smaller. Then, after about five minutes during which the dental cement solidified slightly, the pressurization tube was inserted in the ear canal and secured with more dental cement. Inserting the tube in the ear canal was performed with a great care in order to avoid perforating the TM. The tube was inserted at an angle with respect to the ear canal direction, pointing to the anterior wall of the bony meatus which has a larger distance from the TM. As mentioned earlier, the pressurization tube is supported by the edge of the ear canal opening where there is the slightly solidified dental cement that was applied in the first step. This allows the tube to remain in its place, while the newly applied dental cement is solidifying. Figure 3.11 shows a cross-sectional view of the bulla with the applied dental cement, and the pressurization tube inserted into the ear canal.

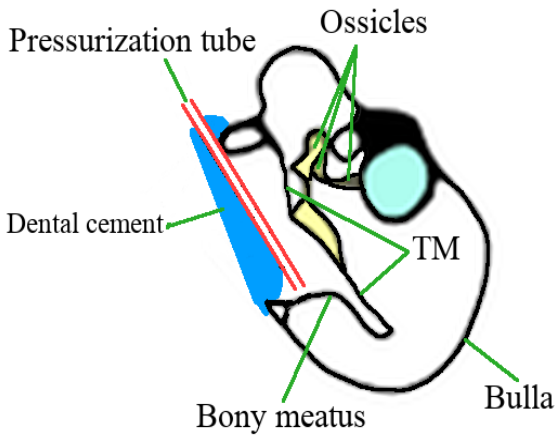

Figure 3.11: A cross-sectional view of the bulla with the pressurization tube and the dental cement (Adapted from: http://audilab.bme.mcgill.ca/AudiLab/teach/me_saf/me_saf.html, accessed on: 2019 July 22)

In our tests, we observed that solidifying the dental cement in the closed volume of the ear canal causes a small negative pressure build-up. Therefore, the pressurization tube was kept open while the dental cement is solidifying for 15 to 20 minutes.

The whole process of preparation takes about 45 minutes from the sacrifice to curing the dental cement and making the animal ready to start the measurements.

3.3.2 Experimental setup

Figure 3.12 shows the experimental setup. After the animal was prepared, the head fixture was adjusted so that we had a clear view of the IS joint through the posterior bulla opening. The IS joint area was aligned horizontally, with the stapes on the right and the incus on the left side of the image. The external Leica light was also adjusted to properly illuminate the inside of the bulla. Since the depth of focus is not enough to completely cover the LP and stapes, the focus was adjusted so that a part of the pedicle-LP attachment and a part of the stapes head are in focus. Adjustments were done using a display screen that was connected to the microscope camera via an HDMI cable. In order to reduce dehydration of the bulla during the experiment, moist cotton was placed on the surface of the bulla and surrounding tissues, and the ultrasonic humidifier was regularly used with an attached tube to directly channel the water vapour into the bulla.

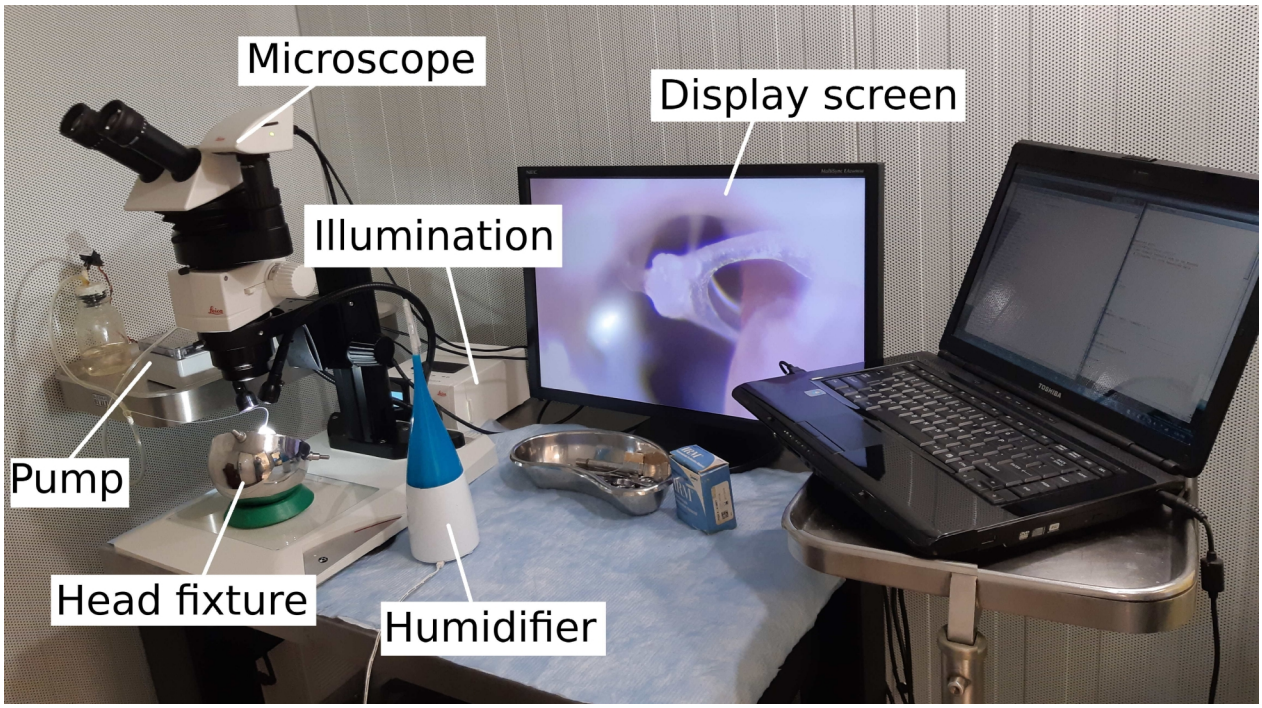

Figure 3.12: Experimental setup.

3.3.3 Experimental protocol

The duration of a full cycle of pressure steps is significantly longer than for a ramp, which in turn increases drying of the bulla. Therefore, different protocols were used for the step and ramp pressure signals.

Step pressure signal protocol: To synchronize the pressure signal and the videos, and to set a start point in our data for processing, the pressurization was started 5 seconds after the start of the recording of the video. The ear canal was pressurized for at least 2 sets, each having 2 full cycles of step signals. In every cycle, the pressure was started from 0 Pa, then increased in 500-Pa steps to 500, 1000, 1500, 2000 and 2500 Pa, being maintained for 5 seconds at each level. Then, the pressure was dropped in 500-Pa steps to −2500 Pa in the same pattern, and increased back to 0 Pa. The recording was stopped afterward and the humidifier was used for 2 minutes to directly re-humidify the bulla after each set.

Ramp pressure signal protocol: The pump is started to maintain the pressure at 0 Pa before starting the pressurization. The video recording is started 5 seconds before the pressurization is started. The ear canal is pressurized for at least 2 sets, each set consisting of 4 consecutive full cycles. Each cycle starts with loading from 0 Pa to 2500 Pa, then unloading to 0 Pa, followed by loading in the negative pressures from 0 to −2500 Pa, and finally unloading to 0 Pa. Both sets have the same pressurization speed, set to a value between 180 Pa/s and 360 Pa/s. At the end of each set, recording is stopped and the humidifier is applied directly into the bulla for 2 minutes. The pressure is kept at 0 Pa during humidification.

3.4 Microstructural study

In the works reviewed in Chapter 2, different tissue-processing methods were used for each imaging modality. Since the middle-ear structures are suspended in air and are sensitive to very small forces, the tissue processing causes unwanted deformations and displacements in all of

the components of the middle ear. These small changes are negligible in some studies, but they become significant relative to small structures such as the IS joint. As an example, variations in the size of the joint gap, and the angle between the LP and the stapes head, have been observed in different studies (e.g., Karmody et al., 2009).

In order to investigate the microstructural changes of the IS joint under static pressures, a new sample-preparation technique was developed to preserve the position of the joint during the tissue-processing procedures. This method was performed on the sample after we finished recording displacements in the last step.

3.4.1 Specimen preparation

This step was a continuation of the preparation described in Section 3.3.1, and started with drilling a hole in the superior side of the bony meatus, which opens a window to the superior aspect of the malleus and incus at the IM joint. With the tube still inserted in the ear canal from the last stage, a static pressure with a constant value was applied to the ear canal, and the pump was set to maintain that constant static pressure in the ear canal. The ossicles were then immobilized at two points using an adhesive. We used an all-purpose ‘instant’ cyanoacrylate (Krazy Glue, USA) glue and a 1-ml syringe. We first glued the IM joint to the cavity wall using the drilled hole in the superior side of the bony meatus. After about 5 minutes, when that glue had completely cured, the stapes footplate and crura were glued to the oval window using the posterior bulla hole that we made to observe the IS joint. The locations of the applied adhesive are shown in Figure 3.13.

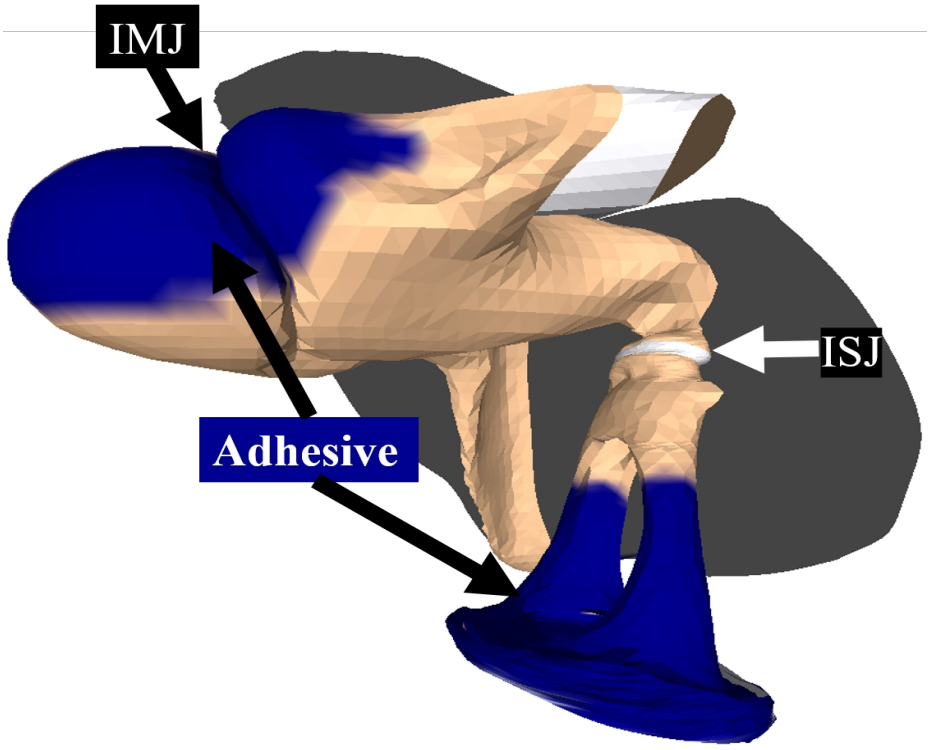

Figure 3.13: Locations of the adhesive application on the ossicles are highlighted in blue (Adapted from Maftoon (2014)).

After about 5 minutes, the pressure in the ear canal was removed, with the immobilized ossicles keeping their positions. This process was done using the stereoscopic microscope, with great care taken to avoid having the adhesive reach the IS joint and damage it. At this point, the bulla is safe for extraction. The head was cut in two pieces along the median plane. Then, the attachment of the bulla and jaw bone was cut and cleaned of soft tissues using tweezers. Immediately after the extraction, 4% PFA in 10× PBS solution was used to fix the sample overnight.

3.4.2 NanoCT scanning

In addition to the extraction and initial fixation, to gain a high-quality scan we need to perform extra procedures for sample preparation and for determining scanner parameters.

3.4.2.1 Sample preparation for imaging

As discussed in Chapter 1, an important limitation of X-ray imaging is its insufficient contrast for soft-tissue visualization. In order to see soft tissues as well as hard tissues in nanoCT scans, either phase-contrast imaging or a contrast agent can be used. We tried to scan several samples using phase contrast but the results were not satisfactory. The reason is that, to get a strong X-ray phase-shift effect, we need to place the source and detector at large distances from the sample, which results in significant attenuation of the X-rays and thus a noisy scan. We therefore used a contrast agent. Of the various options, we used PTA (introduced in Section 2.3.2) since it penetrates better in connective tissues such as the ones that are found in the IS joint. It is also affordable and non-toxic.

To stain our sample, the extracted and chemically fixed middle ear is rinsed with increasing concentrations of ethanol (25%, 50%, 70% and 100%). Then, a 1% PTA in 70% ethanol solution is used to stain the joint for two days. At the end, the sample was rinsed again in the same sequence of increasing ethanol concentrations.

Scanning a sample in air, with its very low X-ray attenuation, provides the best contrast with the middle-ear structures However, the long scanning times dry out the sample. To avoid that, we filled a small portion of the sample tube with 70% ethanol, and sealed it completely with parafilm. This way, the space inside the tube is saturated with ethanol and the moisture in the tissue remains in the sample during the scan.

3.4.2.2 Determining imaging parameters

A number of parameters of the nanoCT scanner can be adjusted to improve the image contrast and reduce the noise. To determine these important parameters, which were described in Section 3.2.3, we scanned a few samples and changed parameters to find the best settings.

We found that the source voltage gave us good results when it is set to around 60 kV. With voltages of 80 kV and above, the bone-air contrast decreased, and with 40 kV and below the images looked darker.

Long exposure times led to saturation of the detector and a loss of contrast, while short durations resulted in more noise in the scans. The exposure time was set to around 10 seconds to keep *counts* (see Section 3.2.3) in the recommended range between 5000 and 6000.

The maximum number of projections that the nanoCT scanner can acquire is 3200 in a full 360° rotation of a sample. It is possible to only take 2-D projections of a sample through a 180° rotation, and to then use mirrored projections for the other 180° of rotation. A large number of projections helped us to reconstruct images with less noise. By using 180° rotations with a total of 1600 projections for our scans, we made the scan time reasonably short (6 hours) with the highest possible number of projections.

To determine the field of view (FOV) and the resolution, we first scanned the sample, with dimensions of about 1 cm^3, with a roughly 13-µm voxel size to locate the IS joint. With a subsequent FOV of about 700 μm^3 containing the pedicle, LP, and a part of the stapes head, we achieved a 0.7-µm voxel size.

3.4.3 Light-sheet sample preparation

The most important step in light-sheet microscopy is making the sample transparent. Previous middle-ear studies using OPFOS employed procedures similar to those used here. We used the X-CLARITY system as a base and modified its protocol to make our samples transparent. The major difference between the middle ear and soft tissues such as brain is the calcium ions found in bone. There are a number of methods, such as Bone CLARITY (Greenbaum et al., 2017) and polyethylene glycol (PEG)-associated solvent system (PEGASOS) (Jing et al., 2018), that have been proposed to make a full mouse transparent, including its hard

tissues. Unlike methods that were developed to make the whole carcass transparent, we only needed to clear the bulla. Therefore, the major modification that we made to the original X-CLARITY protocol was the addition of a decalcification step. The following is our tissue-clearing protocol:

1. Polymerization: This step is done in the same way as mentioned in Section 3.2.5 for the original X-CLARITY protocol, since it helps to preserve the integrity of the structures.

2. Decalcification: This step is added to remove the calcium atoms of the bones. We used 8% EDTA in 1% glutaraldehyde for decalcification The bulla was submerged in the solution and kept under constant stirring at 4°C for 48 hours, changing the solution after 24 hours.

3. Electrophoretic tissue clearing : This step is also done in the same way as in the original X-CLARITY protocol. However, since the bulla does not have large amounts of lipids, this step can be skipped without a significant change in the transparency of the samples. We observed no change in a sample for which this step was skipped.

4. Refractive index matching: We put the bulla in the refractive index matching solution (RIMS) for 24 hours to make it transparent for the scanning with the light-sheet microscope that was done the next day.

After completing the tissue clearing, the sample (still in RIMS) is mounted on the holder of the microscope and is scanned with a 20× objective lens under both green and red light-sheet lasers. After a scan is finished, the sample is transferred into PBS solution. If another scan of the same sample is needed, the sample should be submerged in RIMS again for 24 hours beforehand.

3.5 Data analysis

The last section explained the experiment design and instruments by which we acquired the videos containing displacements of the LP and stapes, and the nanoCT and light-sheet scans revealing the structural changes of the IS joint. This section will describe the methods

implemented to extract information from our displacement videos (Section 3.3) and from our nanoCT and light-sheet imaging (Section 3.4).

3.5.1 Processing displacement videos

As described in Section 3.3, the videos from the stereoscopic-microscope camera have 1920×1080 pixels in each frame, with three-colour channels (RGB) that are recorded at 30 frames per second. The recorded videos are transferred from the SD card to a computer. We needed to locate the LP and stapes over time in every frame to obtain the displacement data. It would be a very time-consuming process to do it manually in all of the frames, so we implemented an automatic object-tracking algorithm.

This algorithm consists of three steps: preprocessing, object tracking, and data visualization. For the preprocessing and object tracking we developed Python code using the OpenCV library, and for data visualization we used MATLAB. In the following sections we explain each step individually.

3.5.1.1 Pre-processing

Before applying the automatic algorithm to the videos, the quality was enhanced for better performance, and a set of manual data was produced in order to validate the outputs of the algorithm.

3.5.1.1.1 Contrast enhancement

Among the three colour channels of a frame, the green one is chosen for the analysis, because it is brighter and has better contrast than the red and blue channels. The enhancement of the contrast is done locally in an area of a video containing a part of the object that is tracked. It has two stages: spreading out grey levels, and mapping them to new values using a power function.

The pixels have grey-level values between 0 and 255. A simple way of increasing the contrast is to stretch the range of grey levels of a low-contrast image to values between 0 to 255 using the function in Equation 3.3:

$$I_{\text{out}} = (I - \min(I)) \frac{255}{\max(I) - \min(I)} \tag{3.3}$$

I is the set of grey levels of the original image, min(I) and max(I) are the minimum and maximum grey levels in the image, respectively, and I_{out} is the set of grey levels of the output image.

Grey levels of the pedicle and background range between 0 and about 160, and for the LP they range between about 140 and 255. To maximize the distinction between the LP and pedicle, especially at their connection surface, a 7th-order function is used that starts changing the values steeply around 150 and makes an acceptable contrast for the tracking. We used the power transformation in Equation 3.4, which non-linearly intensifies grey values (Gonzalez, 2009):

$$I_{\text{out}} = \frac{I^7}{255^6} \tag{3.4}$$

3.5.1.1.2 Image interpolation

The displacements of the LP and stapes are very small, corresponding to only about 30-pixel changes in the videos. By enlarging the selected area, these motions take place in more pixels. This helps the automatic algorithm to perform better, and also manual tracking can be done with a better accuracy in a larger image. We used a built-in OpenCV function that employs the bicubic interpolation method (Keys, 1981) to double the size of the selected area. This method determines a new pixel value using a set of equations derived from a 16-pixel neighbourhood. Compared to other common methods, its results are smoother and have fewer interpolation artifacts, but it takes more time.

3.5.1.1.3 Manual data tracking

A point in the focal plane on either the LP or stapes is tracked every 50 frames to produce data used to validate the automatic algorithm. The point for the LP is selected around the boundary between the pedicle and LP, where it has the highest contrast, and for the stapes it is picked from the posterior side of the stapes head. These areas are shown in Figure 3.14.

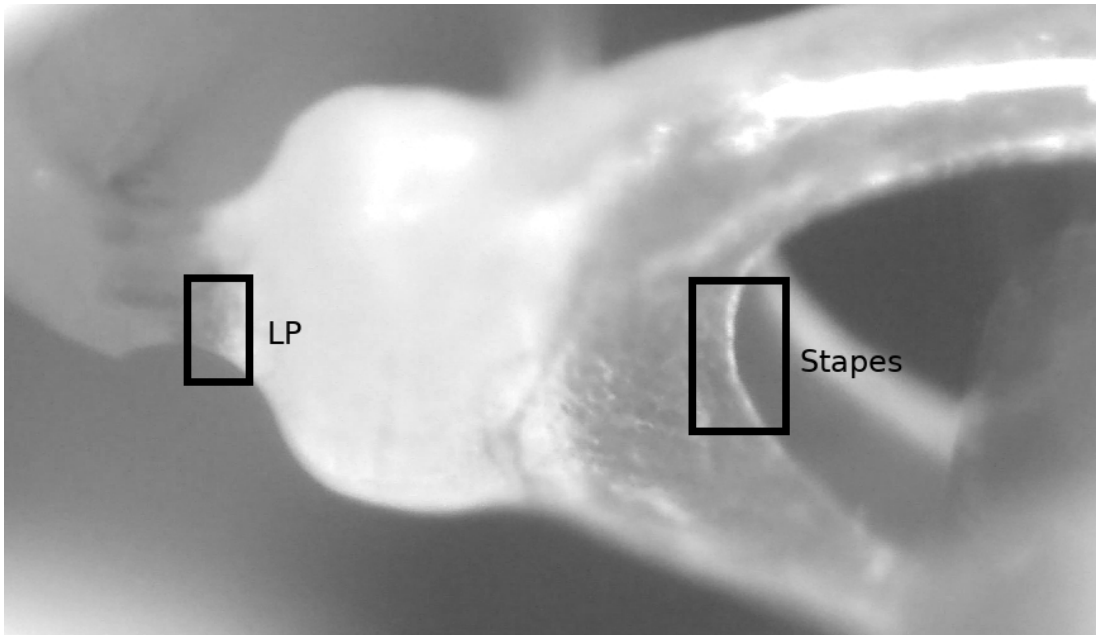

Figure 3.14: Green channel of an image used for the tracking. One point is selected and tracked from inside the specified regions. Left area is used for the LP, and the right area for the stapes.

To confirm that the displacements are consistent in the specified neighbourhoods, we track multiple points in these areas, and compare the results. A magnified area of the image within which a single point is tracked manually after the preprocessing step is shown in Figure 3.15.

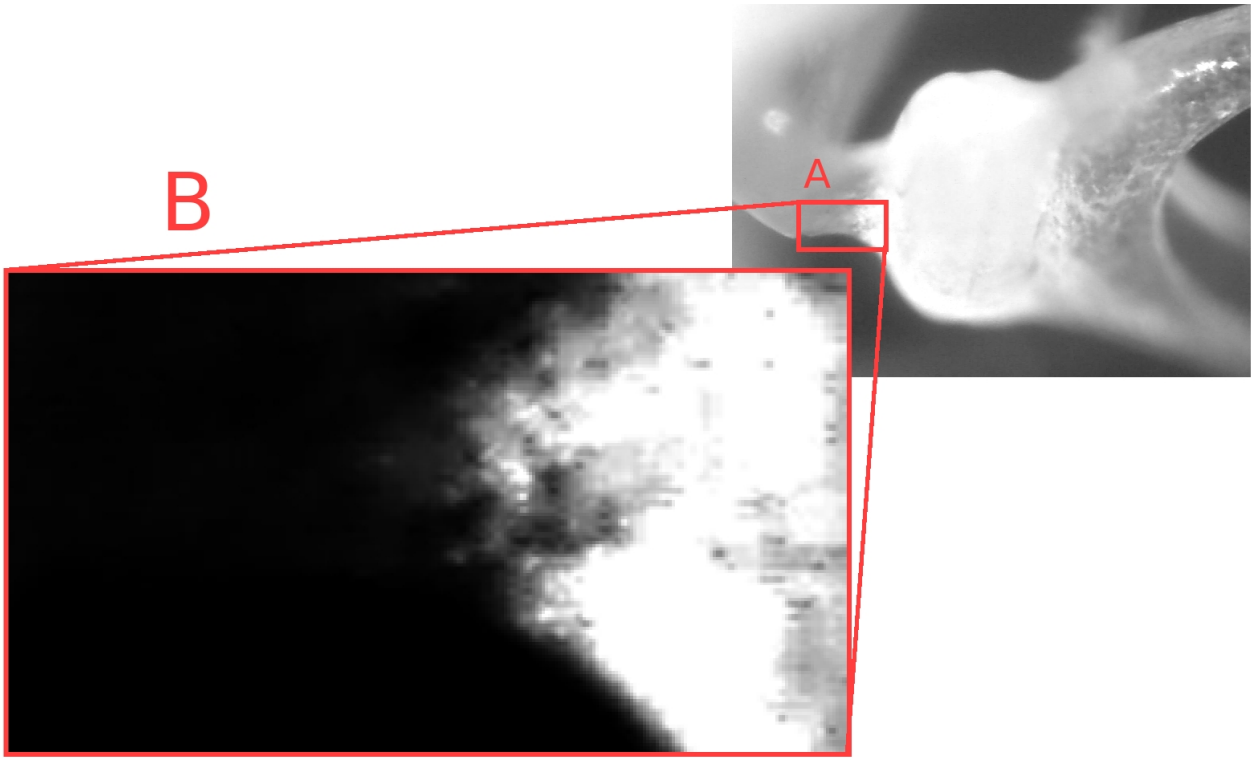

Figure 3.15: B is the magnified selected region of A in the green channel of an image after preprocessing. A point is selected in B and tracked every 50 frames to produce the manual data.

3.5.1.2 Automatic object tracking

We used an automatic object-tracking algorithm based on optical-flow measurement using the Lucas-Kanade method. First we explain the theory of this method, and then describe the procedure that we used to obtain our results.

3.5.1.2.1 Optical flow measurement with Lucas-Kanade algorithm

Optical flow is a method of describing the motions of objects in a scene between two consecutive frames. It is expressed by a vector for each pixel showing the direction and the magnitude of its motion. Optical flow works on two assumptions: the pixel values of an object do not change between two consecutive frames, and neighbouring pixels have similar motions (Paragios et al., 2006).

The first assumption is written as a function in Equation 3.5. It shows that a pixel in the first frame, $I(x,y,t)$, has moved by the distance (dx,dy) in the next frame after time dt:

$$I(x, y, t) = I(x + dx, y + dy, t + dt) \quad . \tag{3.5}$$

Using the Taylor-series approximation of the right side we can write

$$I(x + dx, y + dy, t + dt) = I(x, y, t) + \frac{\partial I}{\partial x} dx + \frac{\partial I}{\partial y} dy + \frac{\partial I}{\partial t} dt \quad . \tag{3.6}$$

From Equations 2.5 and 3.6,

$$\frac{\partial I}{\partial x} dx + \frac{\partial I}{\partial y} dy + \frac{\partial I}{\partial t} dt = 0 \quad . \tag{3.7}$$

If we divide Equation 3.7 by *dt*, we can write

$$\frac{\partial I}{\partial x} \frac{dx}{dt} + \frac{\partial I}{\partial y} \frac{dy}{dt} + \frac{\partial I}{\partial t} \frac{dt}{dt} = 0 \quad . \tag{3.8}$$

Finally, we rewrite Equation 3.8 to get the optical flow equation:

$$I_x V_x + I_y V_y + I_t = 0 \quad . \tag{3.9}$$

I_x, I_y and I_t are derivatives of the image at (x,y,t) in the corresponding directions. This equation has two unknowns, which means we cannot solve it with only one equation. Therefore, several methods have been proposed to solve this problem, and one of them is the Lucas-Kanade algorithm (Lucas & Kanade, 1981). This algorithm uses the second assumption of optical flow, that is, having a similar motion in the neighbourhood of a point. Within a window centred on a point *P* and containing pixels $p_1, p_2, \ldots, p_n$, the local flow satisfies

$$\begin{aligned} I_x(p_1) V_x + I_y(p_1) V_y + I_t(p_1) &= 0 \\ I_x(p_2) V_x + I_y(p_2) V_y + I_t(p_2) &= 0 \\ &\vdots \\ I_x(p_n) V_x + I_y(p_n) V_y + I_t(p_n) &= 0 \end{aligned} \tag{3.10}$$

For this problem, there are now more equations than unknowns, so it is over-determined. The Lucas-Kanade method uses the least-square principle to obtain the solution by minimizing the sum of squared errors of the equations in 3.10. To find the minimum, derivatives of the error function are calculated as shown in Equation 3.11:

$$\min \sum_{i=1}^{n} (I_{xi}V_x + I_{yi}V_y + I_{ti})^2$$

$$\frac{\partial}{\partial V_x} \sum_{i=1}^{n} (I_{xi}V_x + I_{yi}V_y + I_{ti})^2 = \sum_{i=1}^{n} (I_{xi}V_x + I_{yi}V_y + I_{ti}) I_{xi} = 0 \tag{3.11}$$

$$\frac{\partial}{\partial V_y} \sum_{i=1}^{n} (I_{xi}V_x + I_{yi}V_y + I_{ti})^2 = \sum_{i=1}^{n} (I_{xi}V_x + I_{yi}V_y + I_{ti}) I_{yi} = 0$$

Now we have two unknowns with two equations that solve the optical flow problem. The matrix form of the solution is Equation 3.12:

$$\begin{bmatrix} V_x \\ V_y \end{bmatrix} = \begin{bmatrix} \sum_i^n I_{xi}^2 & \sum_i^n I_{xi} I_{yi} \\ \sum_i^n I_{yi} I_{xi} & \sum_i^n I_{yi}^2 \end{bmatrix}^{-1} \begin{bmatrix} -\sum_i^n I_{xi} I_{ti} \\ -\sum_i^n I_{yi} I_{ti} \end{bmatrix} . \tag{3.12}$$

As mentioned earlier, I_{xi}, I_{yi}, and I_{ti} are derivatives of the pixels in corresponding directions (x,y,t), and V_x and V_y are the optical flow values in the x and y directions.

The method is only applicable to small motions having a length of a few pixels and fails when there is a large motion between video frames. To address this issue, the frames are processed using the pyramid method.

3.5.1.2.2 Pyramid representation

A pyramid representation is a resampling of an image to produce smaller versions of the original image, forming a full pyramid as shown in Figure 3.16 (Anderson et al., 1984).

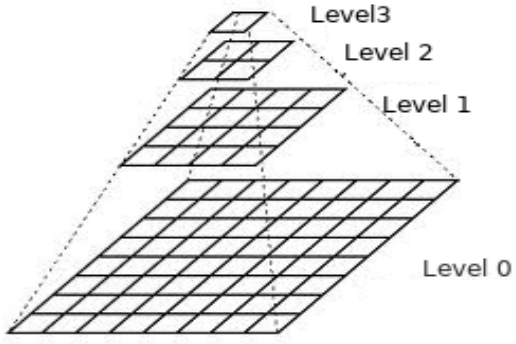

Figure 3.16: The pyramid algorithm applied in three levels. The size of the image is halved in each level (Adapted from:https://docs.opencv.org/2.4/doc/tutorials/imgproc/pyramids/pyramids.html accessed on: 2019 July 29).

The pyramid method produces each level using a kernel with a specific effect on the image. The most popular kernel is the Gaussian pyramid with the kernel shown in Equation 3.13 (OpenCV, n.d.):

$$G=\frac{1}{16}\begin{bmatrix}1 & 4 & 6 & 4 & 1\\ 4 & 16 & 24 & 16 & 4\\ 6 & 24 & 36 & 24 & 6\\ 4 & 16 & 24 & 16 & 4\\ 1 & 4 & 6 & 4 & 1\end{bmatrix} . \quad (3.13)$$

This kernel is convolved with an image at level i of the pyramid, then even-numbered rows of the result are removed to produce the level at $i+1$.

By applying the pyramid method to consecutive frames of a video, at each level, large motions become smaller, until they are reduced to motions with magnitudes of only a few pixels at higher levels. This way, all displacements are measured by applying the Lucas-Kanade algorithm to different levels.

3.5.1.2.3 Automatic object-tracking algorithm

The parameters of the Lucas-Kanade algorithm and the pyramid representation need to be determined. Points that are tracked by the automatic algorithm are selected from the same region used in the manual tracking method. Usually, this region contains 20 to 30 transitional pixels from the high LP grey levels to the low pedicle grey values with the same motions. We set the size of the window in the Lucas-Kanade algorithm to 30 pixels in order to include these points in the optical flow calculations for a better approximation. Another parameter is the number of pyramid levels. We observed that the maximum displacement between two consecutive frames in different samples is about 2 pixels. Therefore, we set the number of pyramid levels to 6 in order to ensure that the Lucas-Kanade method detects all displacements that are doubled in the preprocessing step due to enlarging frames (considering 1 extra pixel in displacements).

The tracking process starts with choosing one of the recorded videos as the input. Then, an area of the video is selected that includes at least a part of the object that needs to be followed. This region is roughly the same area where the manual data were produced.

We use an OpenCV function for the Lucas-Kanade algorithm that gets the coordinates of points in the input, and gives the new coordinates of those points in the next frame in the output. An initial set of points is selected using a rectangular selection tool. Each of the pixels that falls inside the rectangle is individually tracked by the algorithm. When the tracking is finished in all of the frames, the output is an array whose number of rows is equal to the number of points, and the number of columns is the same as the number of frames. Each of the rows contains the coordinates of a point tracked over the frames.

In order to calculate the displacements of the points, each row is subtracted from its first value. By doing that, the initial location of the followed point is set to zero, and all other values show displacements from the initial position without dependence on any reference point.

Finally, for each point, the differences between displacements determined by the automatic and manual methods in the same frames (every 50 frames) are calculated as an error array. Then, the maximum value in this array is considered as an error measure. The best point is the one with the minimum error and it is saved in a text file.

3.5.1.3 Data visualization

A MATLAB script is used to extract data, and to categorize and present the results. The displacement data of the LP and stapes obtained in Section 3.5.1.2.3 are loaded. Then, the first 5 seconds of this data, recorded to synchronize with the pressure signal, are removed. The gap changes of the IS joint are indirectly measured by subtracting the stapes and LP displacements. The loading and unloading parts of the data are then extracted and used to plot figures.

3.5.2 NanoCT and light-sheet scan analysis

There are a number of important anatomical features of the joint which was measured in the nanoCT and light-sheet scans: the gap size, capsule length, and cartilage thickness. These characteristics need to be measured at the same locations of the IS joint in all samples to be comparable. Therefore, in addition to the reference frame used for displaying displacements, a longitudinal plane that includes anterior and posterior crura and the superior side of the stapedial tendon was determined as the reference plane, as shown in Figure 3.17.

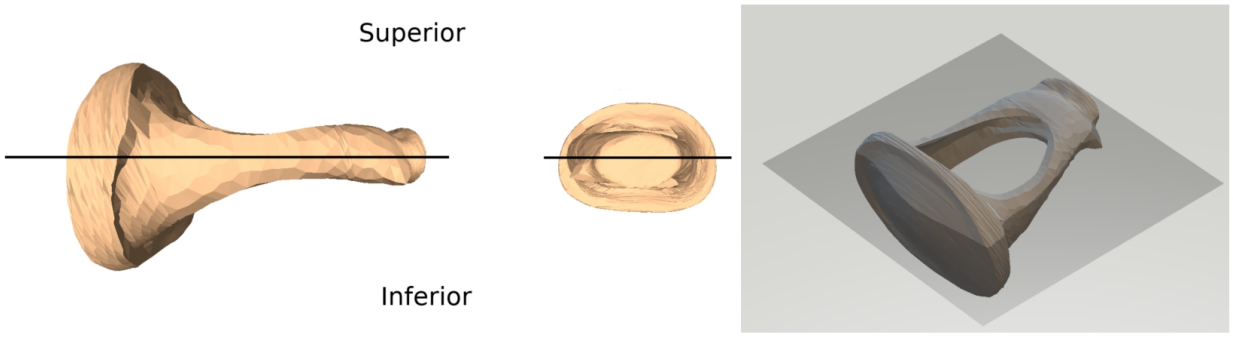

Figure 3.17: Reference plane for nanoCT and light-sheet scan measurements (derived from model of Maftoon (2014)).

Volume rendering, manual registration and measurements of the nanoCT and light-sheet scans were done with tools provided in Dragonfly (https://www.theobjects.com/dragonfly/).

Chapter 4. Results

4.1 Introduction

In this chapter we present the results obtained using the methods described in Chapter 3. First, in Section 4.2 the video-analysis outputs are presented. Then, in Sections 4.3 and 4.4 nanoCT scan and light-sheet images are presented, respectively. Finally, in section 4.5, the results are discussed and compared with previous findings. The results with step pressure signals are not included; steps were used during development but not with the final protocol.

4.2 Video-analysis results

In this section, first we show the preprocessing outputs, then the results obtained from our video-analysis method are presented.

4.2.1 Preprocessing

As an example, Figure 4.1a shows a region of the green channel of the first frame of a video, selected such that it includes a part of the LP (in this case) or stapes and covers its complete range of motion throughout the video. This area is selected in nearly the same location for both manual and automatic methods. In Figure 4.1b, c and d, the result of each preprocessing step is displayed, with its image histogram at the bottom.

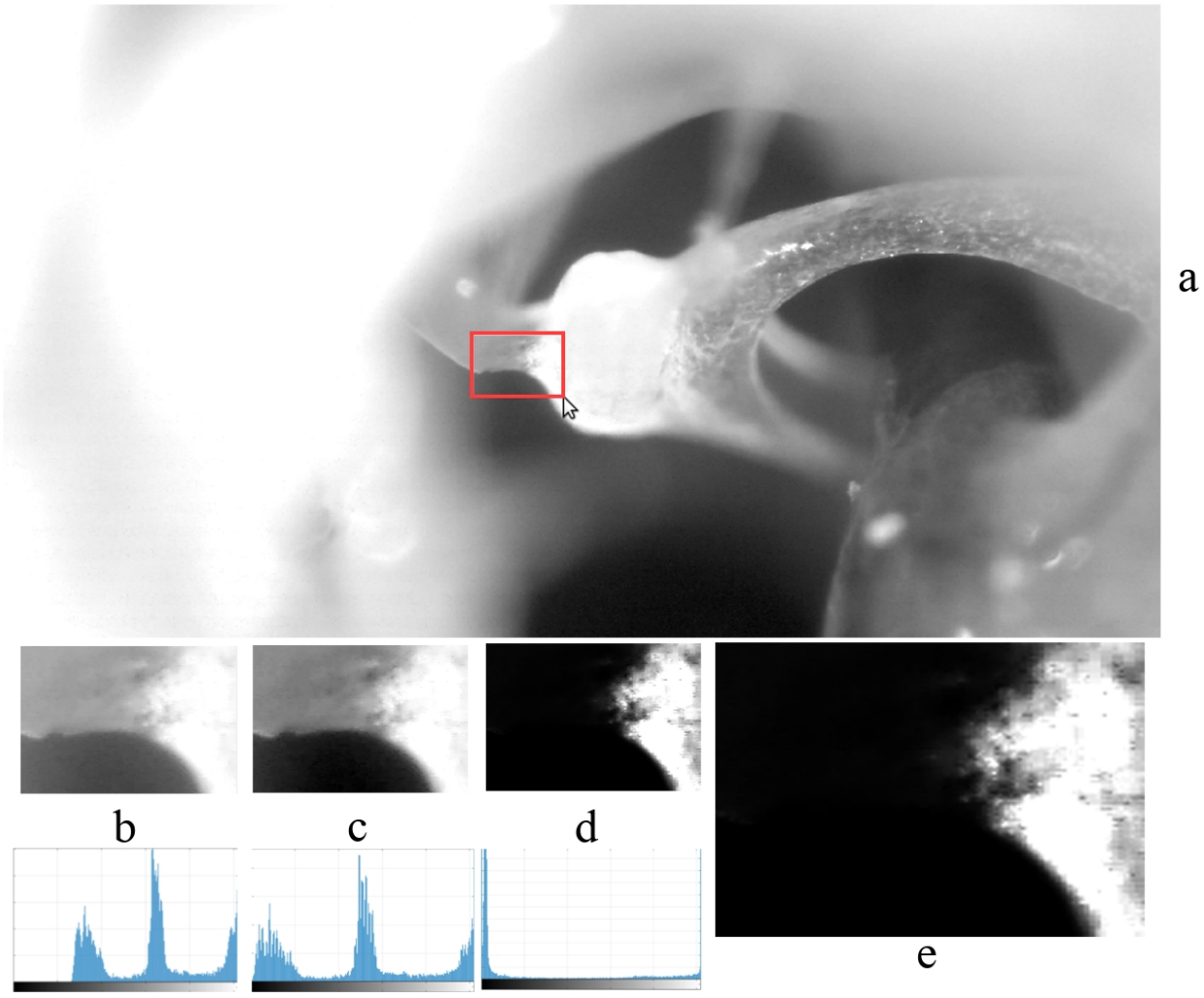

Figure 4.1: Preprocessing steps to track the LP: (a) is the green channel of the original frame, (b) shows selected area specified in (a) with its image histogram at the bottom, (c) is the result after stretching grey levels between 0 to 255, with its image histogram at the bottom, (d) is after applying the 7th-order power function to (c), with its histogram at the bottom, and (e) is a resized version of (d) with double height and width.

4.2.2 Displacement results

We obtained our data using the finalized experiment explained in Chapter 3, from the left ear of gerbil G1 (G1L) and both ears of gerbil G2 (G2L and G2R). The pressurization speeds of the ramp signals were 340 Pa/s for G1L, 180 Pa/s for G2R, and 180, 240, and 360 Pa/s for G2L. The first measurement in G1L was done 108 min after sacrifice, and in G2L and G2R the first measurements were done 53 min and 112 min after sacrifice, respectively. The LP displacements are presented first, followed by the results of the stapes motions, and the changes of the IS joint

gap afterwards. An apparent sliding motion between the LP and stapes is presented in Section 4.2.3.

4.2.2.1 Lenticular-plate displacements

Figures 4.2 and 4.3 show the horizontal and vertical displacements, respectively, of the LP of G2L for a full pressurization cycle, plotted against both time and pressure. The average pressurization speed of the pressure ramp over the cycle was 185.6 Pa/s and its duration was 53.87 s. As expected, the range of piston-like displacements (in the horizontal direction) is much larger than the range in the vertical direction. The loading and unloading parts of the negative and positive pressures are shown in different colours in the displacement-versus-pressure figures. For the positive pressures the displacements are limited to less than 5 μm for the horizontal direction, and 2 μm in the vertical direction, quickly reaching their maxima. On the other hand, in the loading part of the negative pressures, the LP moves almost linearly with the changes of the pressure signal, having its maximum around 13 μm horizontally, and 3 μm vertically; in the unloading part, however, the displacement stays almost constant before dropping quickly to 0 Pa.

In the areas indicated by green rectangles in Figure 4.2, in the range between +1400 Pa and +2500 Pa, the LP reverse direction and moves slightly laterally (outward), when the ear-canal pressure increases, and then medially when the ear-canal pressure decreases. We think this behaviour might be associated with the buckling motion of the eardrum reported previously by some groups (e.g., Dirckx et al., 1998; Ladak et al., 2004) and simulated by our group (Choukir, 2017). Further investigation is needed to clarify the origin of this motion.

Red circles in Figure 4.2 indicate small disturbances in the displacements of the LP. This disturbance is also seen in other results. It will be discussed in Section 4.2.3, where it is interpreted as an effect of sliding motion of the stapes relative to the LP. As seen in Figure 4.3, the effect of the stapes sliding motion is not visible in the vertical displacements.

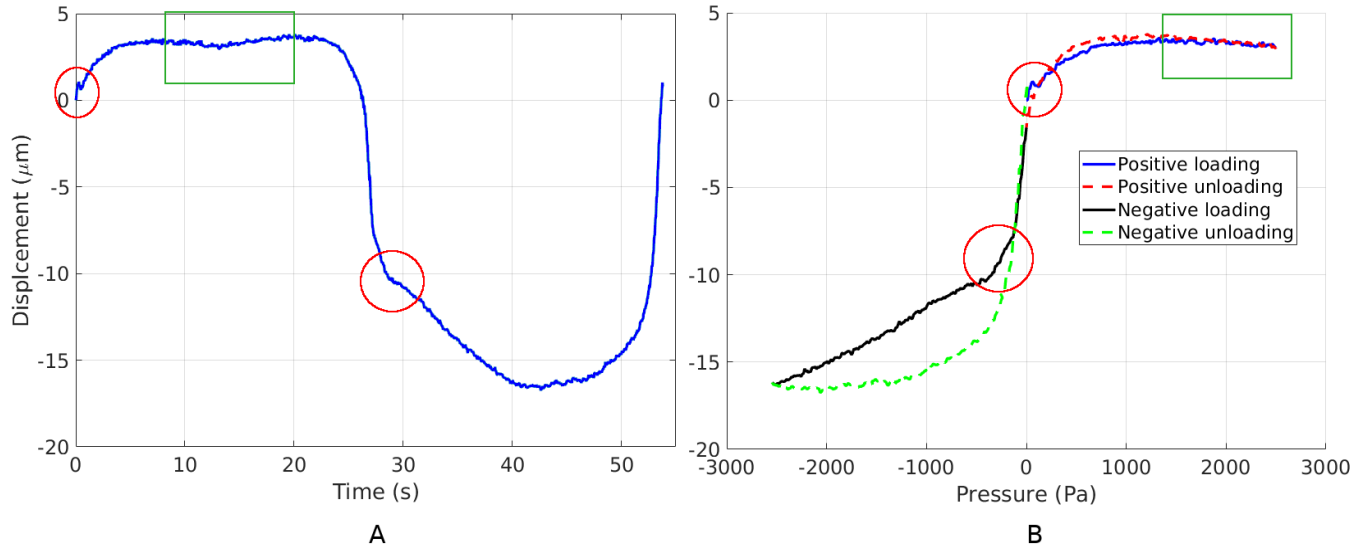

Figure 4.2: Horizontal displacements of the LP of G2L. A: as a function of time. B: as a function of pressure; loading and unloading parts of the pressurization are shown in different colours. The green rectangles and red circles indicate features discussed in the text.

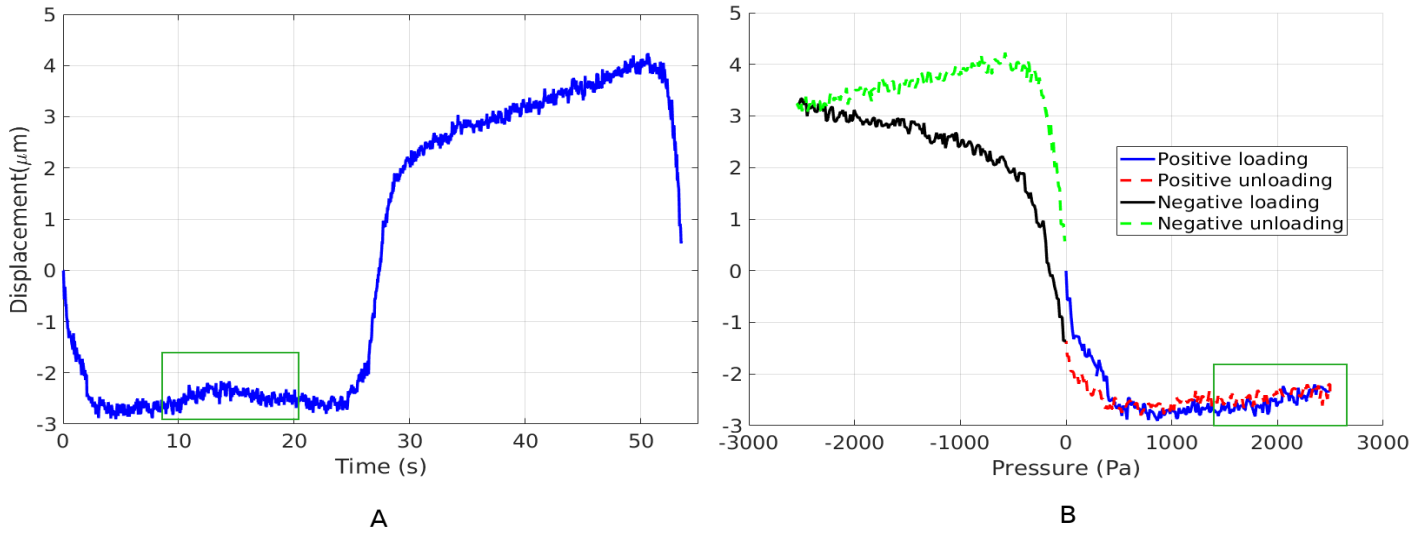

Figure 4.3: Vertical displacements of the LP of G2L. A: as a function of time. B: as a function of pressure; loading and unloading parts of the pressurization are shown in different colours. The green rectangles indicate a feature discussed in the text.

In our protocol as described in Chapter 3, the ear canal is pressurized in four consecutive cycles in a set. In Figures 4.4 and 4.5, displacements of a set of G2L cycles are shown versus time and pressure, respectively. The duration of this set, with a pressurization speed of 186.13 Pa/s, is 214.9 s. Each cycle of this set is shown in a different colour in Figure 4.5. In both figures,

the cycles show a quite consistent pattern except for the first cycle. In Figure 4.4 there is a small shift (about 2 µm) in the baselines. This may be due to some inaccuracy of the automatic tracking algorithm and/or a small change of the sample position over the duration of the experiment. To decrease the effect of the drift, for the displacement-versus-pressure figure (Figure 4.5) we individually extracted each cycle and subtracted it from its first value, thus setting the baseline to zero for each cycle. We observed in most sets that the first cycle is different from the other three cycles, with a larger offset in the vertical direction; we interpret this as an effect of preconditioning.

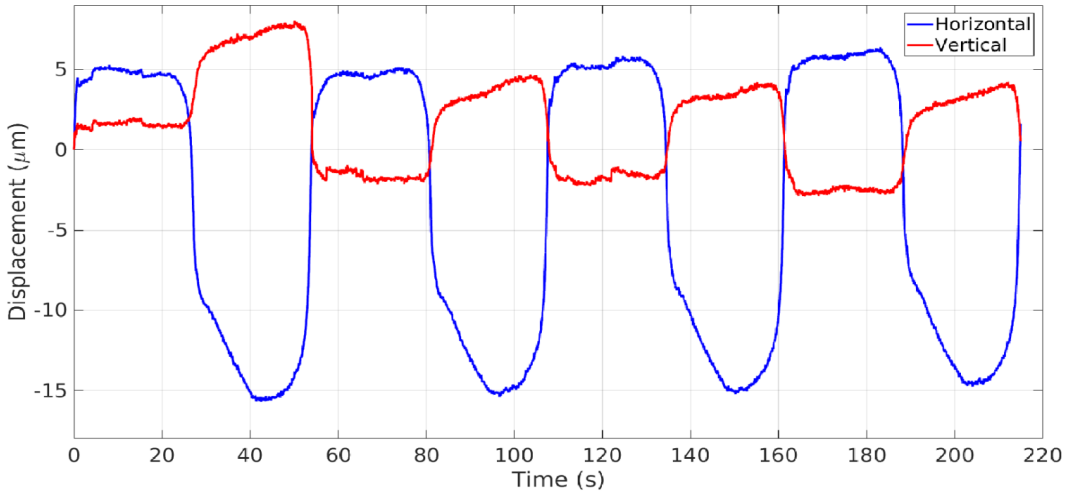

Figure 4.4: One set (four full cycles) of the LP horizontal (in blue) and vertical (in red) displacements versus time in G2L.

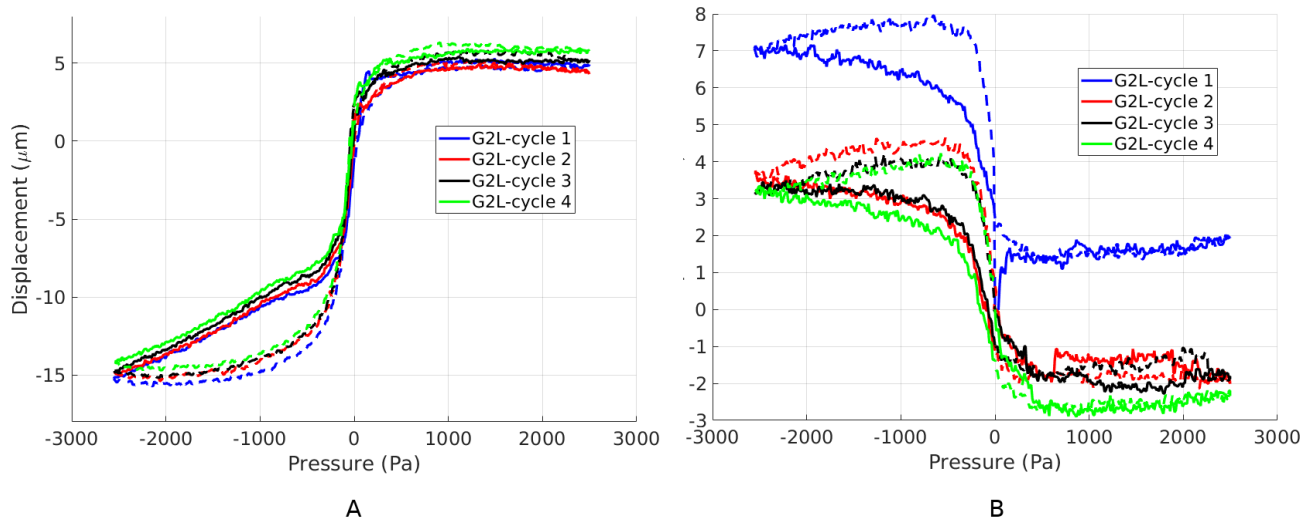

Figure 4.5: One set (four full cycles) of the LP displacements versus pressure in G2L. A: horizontal displacements. B: vertical displacements. Solid lines show loading, and dotted ones unloading.

Two sets of pressurization were done on G2L, with the same pressurization speed of 180 Pa/s. The results are shown in 4.6. The same pattern is clearly visible and repeated in both sets, with subtle differences presumably due to the reasons mentioned earlier. It is clearly visible that estimates for the vertical displacements are noisier than those for the horizontal ones. This is because of the small range of the vertical motions, which makes the tracking harder for the automatic algorithm.

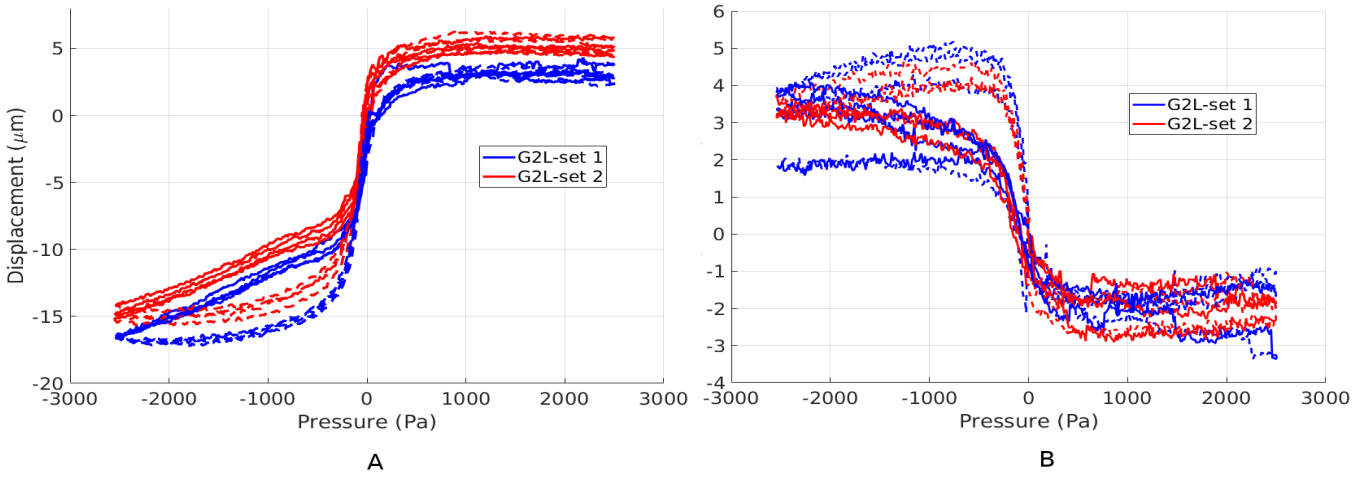

Figure 4.6: The LP displacements versus pressure for two pressurization sets for G2L. A: Horizontal displacements. B: Vertical displacements. Solid lines show loading, and dotted ones unloading.

Figure 4.7 shows the displacements of G2R for 6 sets. In this sample, three different speeds were used; 180 Pa/s for sets 1 and 2, 240 Pa/s for sets 3 and 4, and 360 Pa/s for sets 5 and 6. The last set was measured with no re-hydration between two sets, and that caused a smaller range in motions. The effect of the pressurization speed is not significant among the sets; this might be because of the relatively small range of speeds (a factor of two) that was used. The vertical motions in Figure 4.7B are flipped around a horizontal axis compared to the G2L motions, because the measurements were done in the right ear.

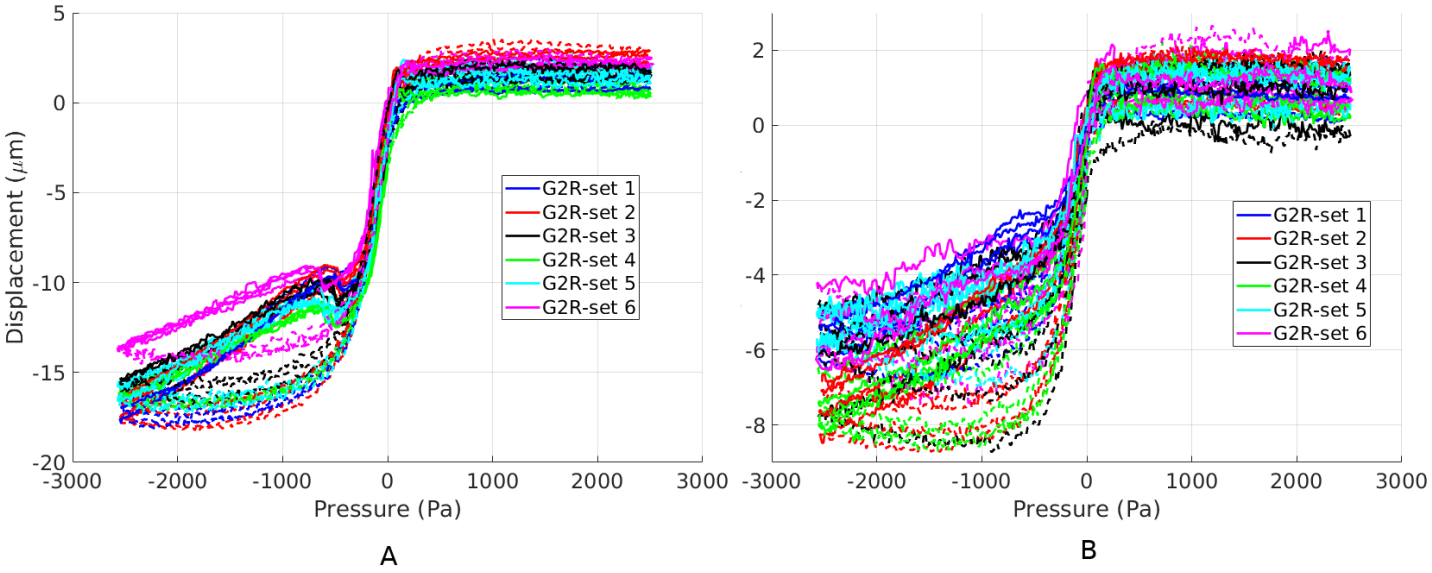

Figure 4.7: Displacements of the LP in G2R. A: Horizontal displacements. B: Vertical displacements. Solid lines show loading, and dotted ones unloading.

Figure 4.8 shows the horizontal and vertical displacements for the two sets for G1L, with a speed of 340 Pa/s. The algorithm could not accurately estimate the very small vertical motions in this sample.

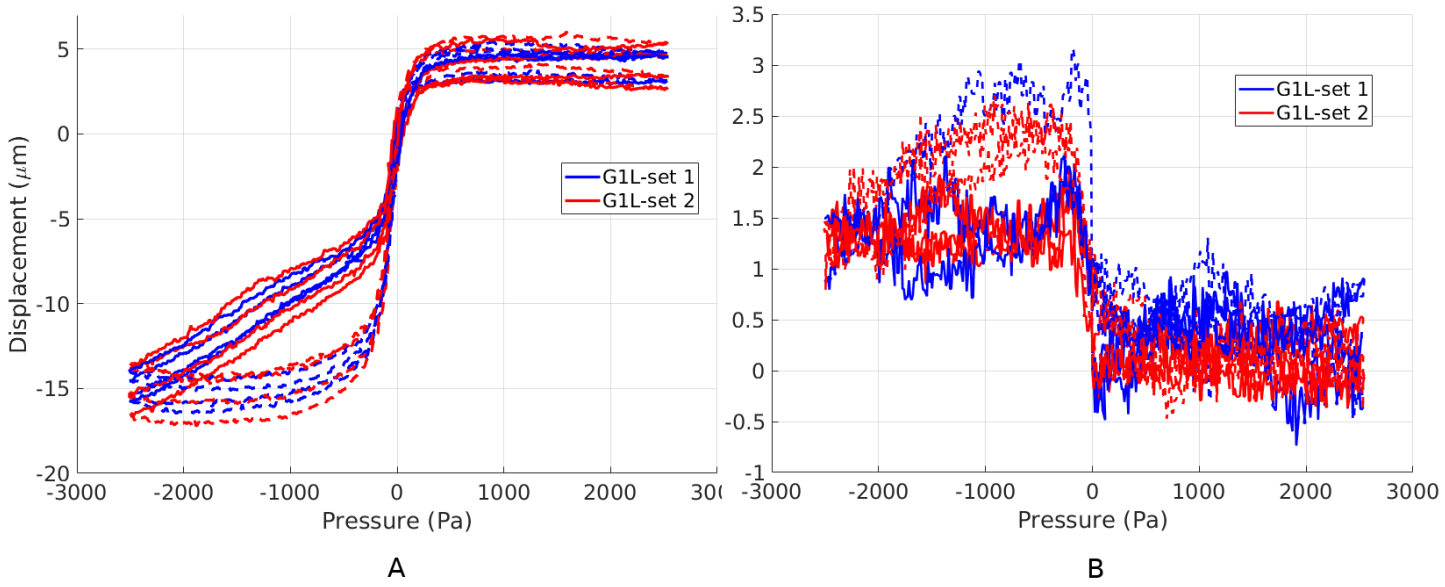

Figure 4.8: The LP displacements of G1L in two sets. A: horizontal displacements. B: vertical displacements. Solid lines show loading, and dotted ones unloading.

Figure 4.9 shows the second cycles of each of G1L, G2R, and G2L. There are two significant differences that are noticeable between ears. First, the effect of the stapes sliding motion on the LP varies among the samples. In G2R, there is a quite substantial stapes sliding-motion effect on the LP around −430 Pa in the negative loading part, while there is a smaller change in G1L and G2L. Another difference is in the baseline of these displacements, which is

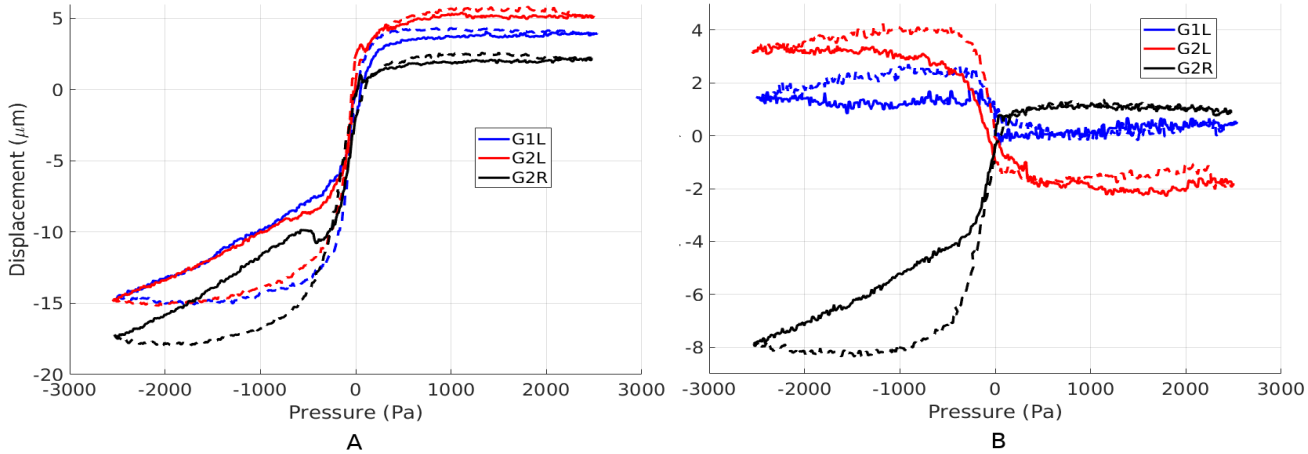

Figure 4.9: Displacement versus pressure for three different cycles of G1L, G2L, and G2R. A: Horizontal displacements. B: Vertical displacements. Solid lines show loading, and dotted ones unloading. Solid lines show loading, and dotted ones unloading.

expected due to the variability among animals. There is also a difference of about 1 µm between the peak-to-peak amplitudes of G1L and G2L.

Figures 4.10 and 4.11 show results from all 4 cycles of 10 sets, from all three ears, in the horizontal and vertical directions, respectively. A very similar pattern is clearly visible in all of the samples. G2L and G2R are more similar, because they are measured from one animal. Here it is also obvious that vertical displacements have more variations.

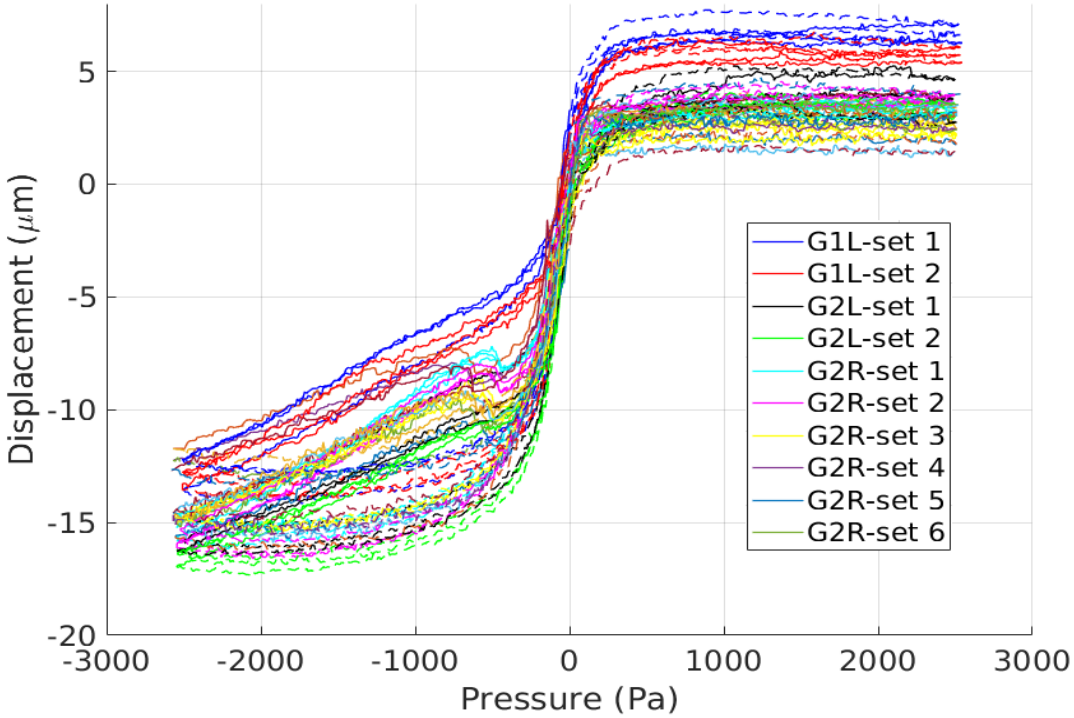

Figure 4.10: Horizontal displacements for 10 sets of three samples. Solid lines show loading, and dotted ones unloading.

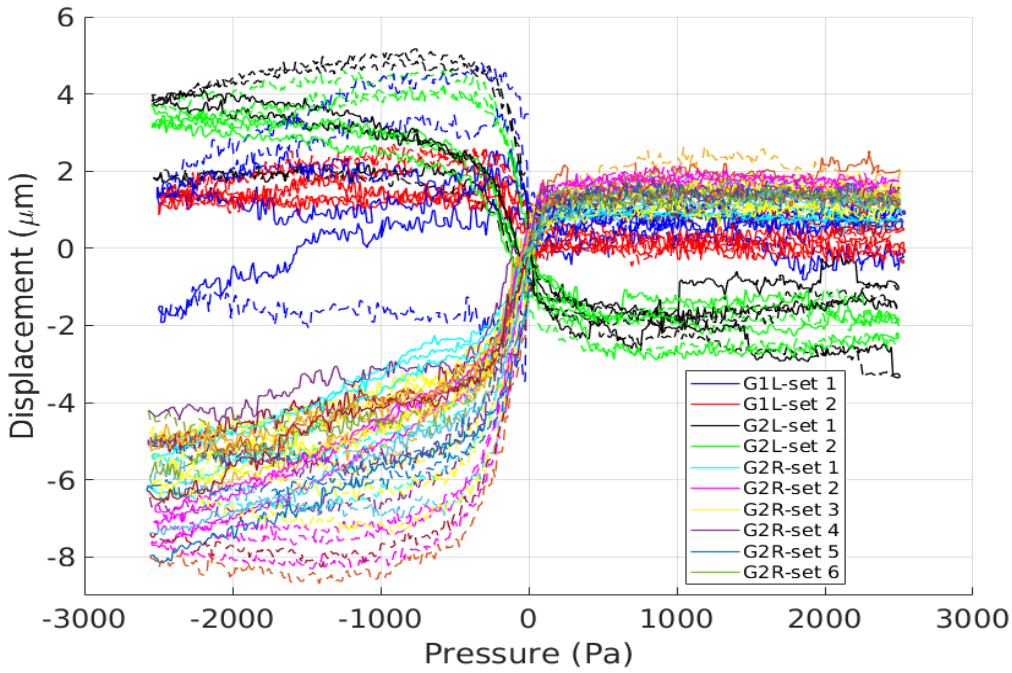

Figure 4.11: Vertical displacements of 10 sets of three samples. Solid lines show loading, and dotted ones unloading.

We measured the peak-to-peak amplitude of the horizontal and vertical displacements in each cycle for all samples. Table 1 shows the horizontal displacement amplitudes, and averages and standard deviations. The average (±standard deviation) over all cycles is 19.6±1.2 µm. The low standard deviation shows that the variations observed in different cycles and sets are mostly because of the differences in their baselines and not in the amplitudes.

Table 2 shows peak-to-peak amplitudes for the vertical displacements. There is consistency within every set, but to a lesser extent among the samples. A noticeable difference is that the amplitudes of G2R and G2L were about twice that of G1L. This might be because of real variability between animals.

Table 1: Peak-to-peak amplitudes of horizontal displacements for all cycles

		Peak-to-peak amplitude (µm)					
Sample	**Set number**	**Cycle 1**	**Cycle 2**	**Cycle 3**	**Cycle 4**	**Mean±standard deviation**	
G1L	**Set 1**	20	21	20	19	20.4±0.5	20.3±0.4
	Set 2	20	20	19	20	20.3±0.5	
G2L	**Set 1**	21	20	20	20	20.6±0.6	20.7±0.4
	Set 2	20	20	21	21	20.9±0.2	
G2R	**Set 1**	19	19	19	18	19.4±0.4	18.9±1.1
	Set 2	20	20	20	20	20.6±0.1	
	Set 3	18	18	18	18	18.5±0.2	
	Set 4	18	18	18	18	18.2±0.2	
	Set 5	19	19	19	19	19.4±0.1	
	Set 6	17	17	17	17	17.1±0.1	
Mean±standard deviation		19.7±1.3	19.6±1.2	19.5±1.2	19.4±1.2	**19.6±1.2**	

Table 2: Peak-to-peak amplitudes of vertical displacements for all cycles

		Peak-to-peak amplitude (µm)					
Sample	**Set number**	**Cycle 1**	**Cycle 2**	**Cycle 3**	**Cycle 4**	**Mean±standard deviation deviation**	
G1L	**Set 1**	4	4	4	5	4.7±0.1	3.9±0.8
	Set 2	3	3	3	3	3.1±0.2	
G2L	**Set 1**	7	4	7	8	7.1±1.7	7.3±1.3
	Set 2	8	6	8	7	7.6±0.7	
G2R	**Set 1**	6	7	8	6	7.25±0.5	8.5±1.1
	Set 2	9	10	9	9	9.78±1	
	Set 3	9	8	8	8	8.6±5	
	Set 4	9	9	9	10	9.7±3	
	Set 5	7	8	9	7	8.0±6	
	Set 6	8	7	7	8	7.9±7	
Mean±standard deviation		7.5±2.0	6.9±2.23	7.5±2.1	7.5±2.1	**7.4±2.1**	

We select the best point to use by comparing multiple points with manual data. Only the horizontal displacements are compared, since they are less noisy. In Table 3, differences between the manual result and the automatic result for the best point are shown.

Table 3: Differences between the manual data and automatic outputs of the selected point

Sample	Set number	Difference (µm)	Average	
G1L	Set 1	4	3.3±1.1	**1.9±0.9**
	Set 2	2		
G2L	Set 1	2	2.1±0.5	
	Set 2	1		
G2R	Set 1	2	1.3±0.4	
	Set 2	1		
	Set 3	1		
	Set 4	1		
	Set 5	0		
	Set 6	1		

4.2.2.2 Stapes displacements

Displacements of the G2L stapes in the horizontal and vertical directions in one cycle are shown in Figure 4.12 and 4.13. The duration of the cycle is 53.87 s with an average speed of 185.6 Pa/s. The displacements in the horizontal direction are between about 2 and 14 µm, while in the vertical direction they are limited to between about 1.75 and 3 µm. For the positive pressures, the stapes settles down quickly, and for the negative pressures we see almost symmetric horizontal displacements in the loading and unloading parts with a small peak at the minimum pressure. In the displacement-versus-pressure figure, we see a strong non-linearity for both positive and negative pressures.

At the start of the pressurization with positive pressures, the stapes sliding-motion is indicated by the red circles, in both directions, and the possible buckling effect of the eardrum around 1100 Pa is pointed out in the figures with green rectangles.

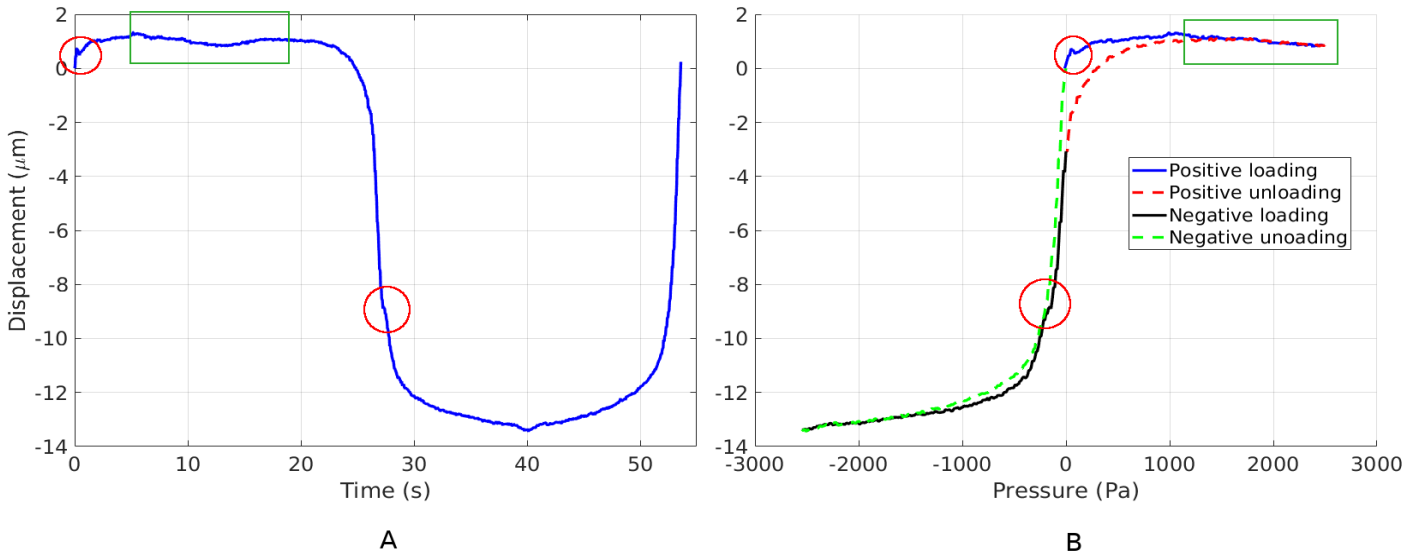

Figure 4.12: Horizontal displacements of the G2L stapes. A: Displacement versus time. B: Displacement as a function of pressure. Green rectangles are possibly due to the eardrum buckling, and red circles are the effect of sliding motion. Solid lines show loading, and dotted ones unloading.

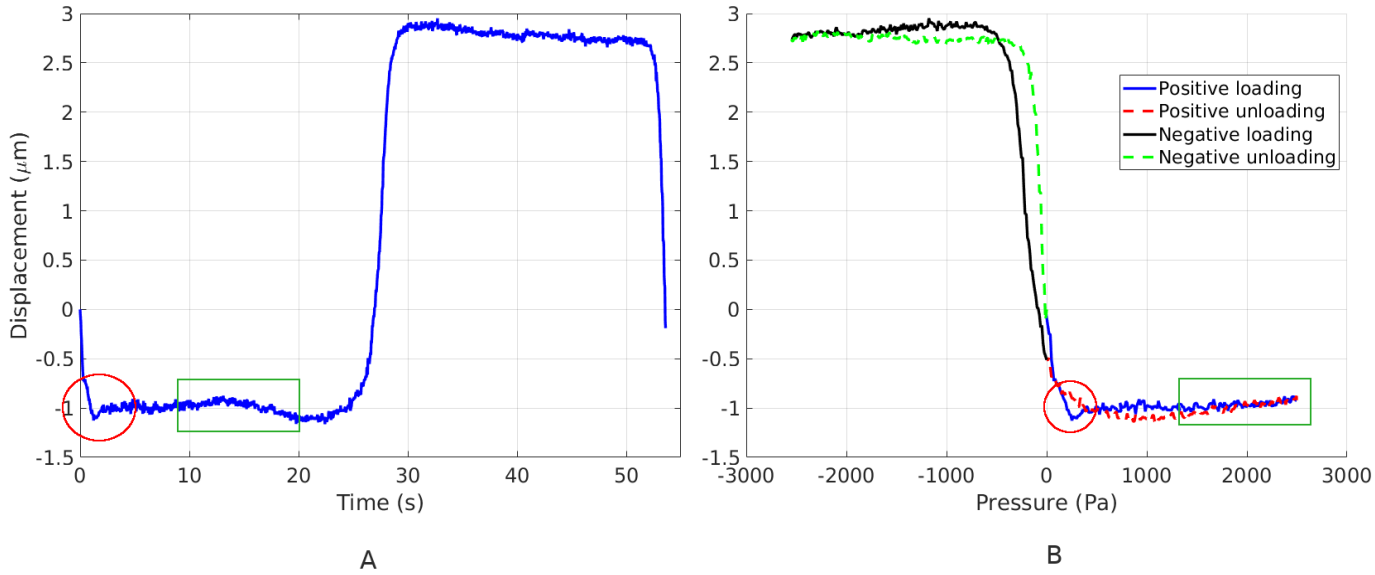

Figure 4.13: Vertical displacements of the G2L stapes. A: Displacement versus time. B: Displacement versus pressure. Green rectangles are possibly due to the eardrum buckling, and red circles are the effect of sliding motion. Solid lines show loading, and dotted ones unloading.

Figure 4.14 and 4.15 show the results for displacements in both directions for a set as a function of time and pressure respectively. There is a 3-µm drift as mentioned earlier in Section 4.2.2.1, which is visible in the horizontal direction, presumably due to a change of the sample position during the experiment. We decreased its effect in the same way we did for the LP displacements. There is a consistency in the pattern among the cycles, except for the first cycle which is considered as preconditioning.

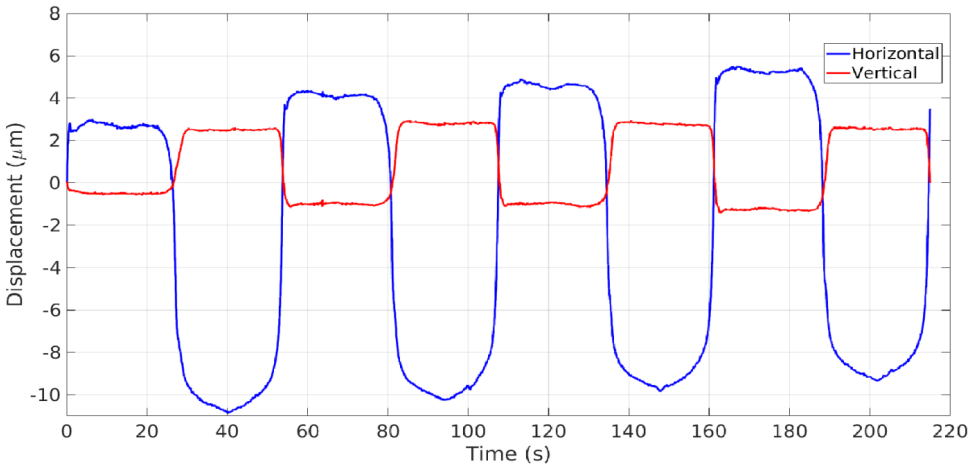

Figure 4.14: One set of the stapes displacements of G2L.

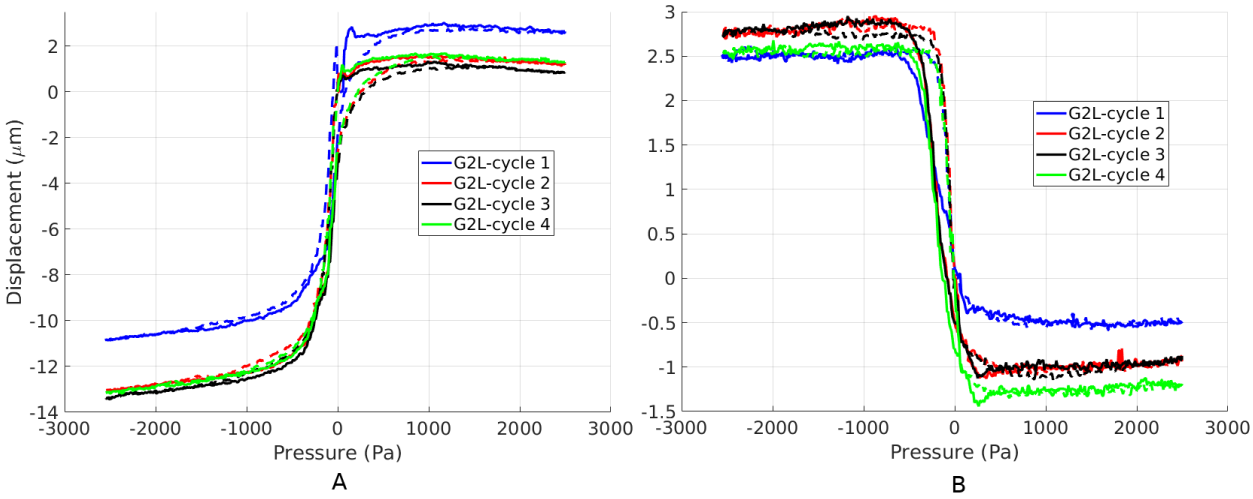

Figure 4.15: Displacements of a set of G2L. A: Horizontal displacements. B: Vertical displacements. Solid lines show loading, and dotted ones unloading.

Two pressurization sets of the G2L are shown in Figure 4.16. Patterns in both sets are repeated with small shifts in the baseline.

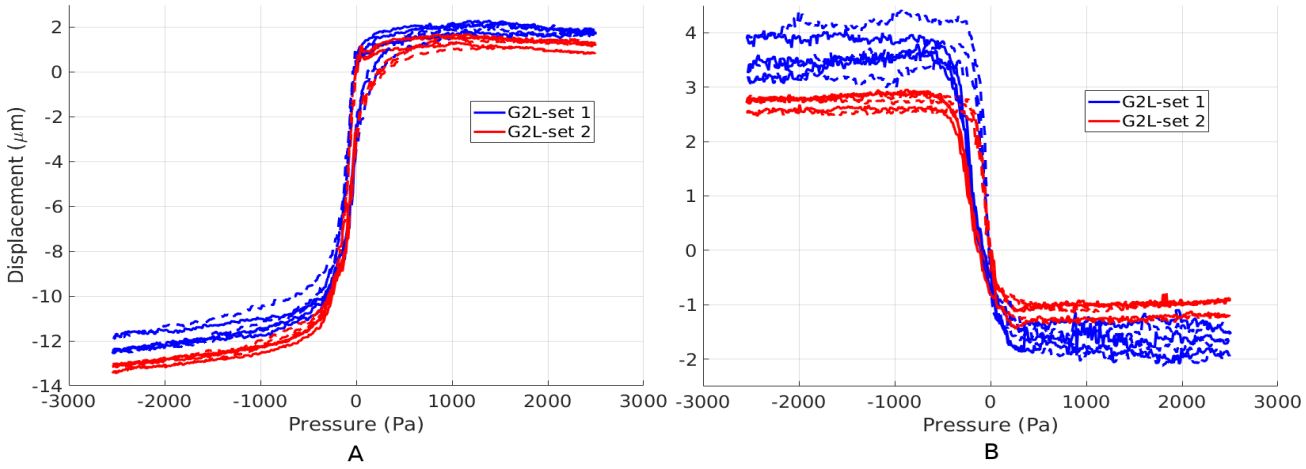

Figure 4.16: Displacements of two sets of G2L. A: Horizontal displacements. B: Vertical displacements. Solid lines show loading, and dotted ones unloading.

Figure 4.17 shows the vertical and horizontal displacements for the 6 sets of G2R. There is an exception in the pattern in the first set in the horizontal direction, with two strong sliding-motions, one around +72 Pa, and the other around −430 Pa. A bad estimation of the vertical displacements is visible for the first set of G2R.

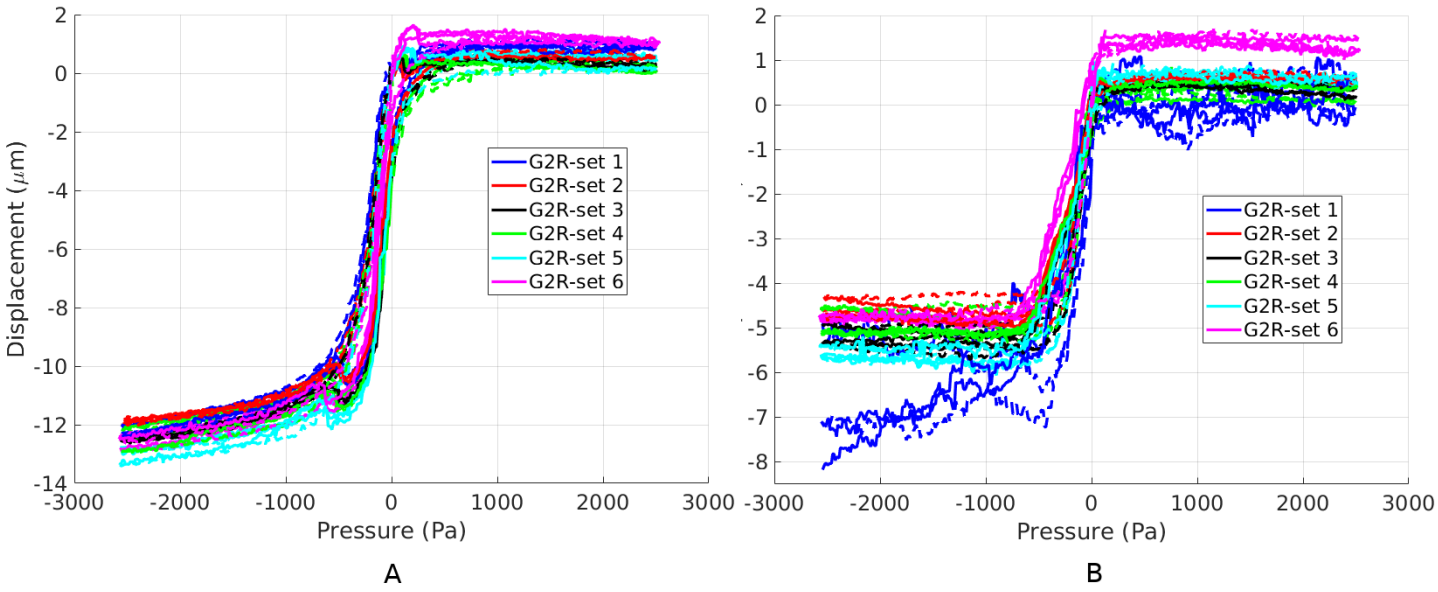

Figure 4.17: Displacements of G2R for 6 sets. A: Horizontal displacements. B: Vertical displacements. Solid lines show loading, and dotted ones unloading.

The horizontal and vertical motions of G1L are shown in Figure 4.18. The displacements are consistent in all cycles in the horizontal direction, but the results are very noisy and inconsistent for the vertical direction. There is also a small stapes sliding motion visible around +50 Pa in the horizontal direction.

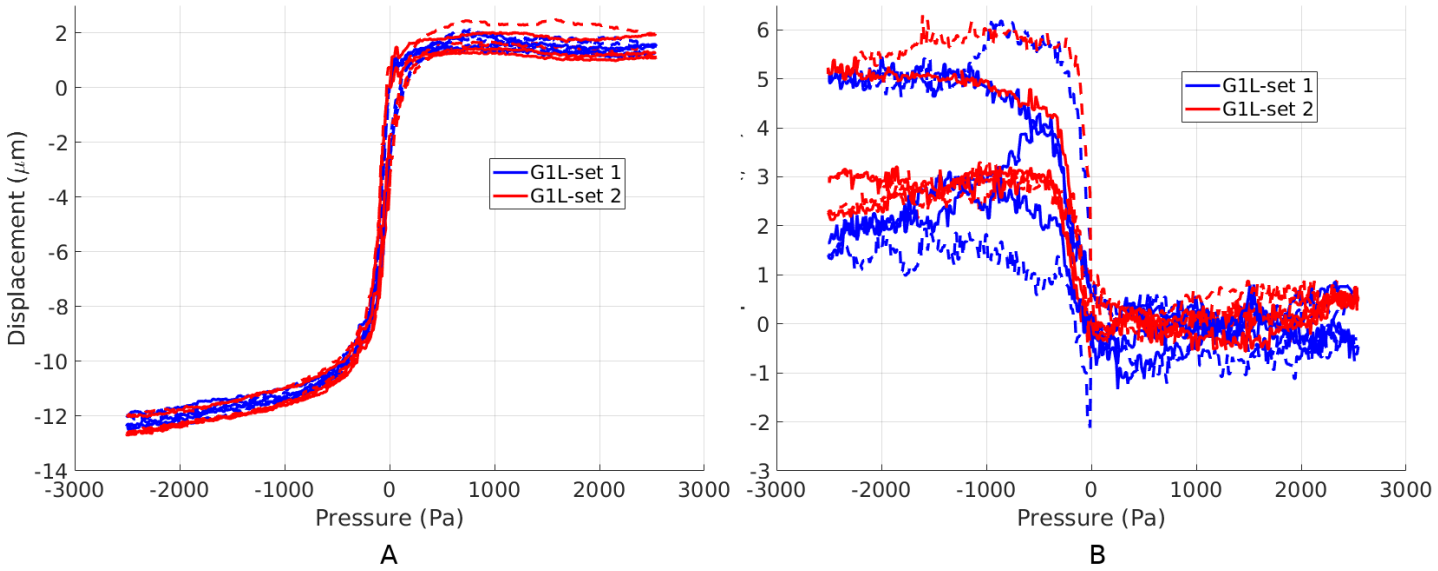

Figure 4.18: Displacements of G1L for two sets. A: Horizontal displacements. B: Vertical displacements. Solid lines show loading, and dotted ones unloading.

Figure 4.19 shows displacements in one cycle for each of the three samples. The overall non-linear pattern is repeated in all ears and for both motion directions. The vertical displacements have more variations between different cycles, but the overall pattern is reproduced. In G2R, the displacements in the vertical direction are mirrored, because the measurements were made in the right ear and the others are from the left ear. In the horizontal displacements, the TM buckling effect appears in all three ears, and also the stapes sliding motion in the loading part of the positive pressures is clearly repeated in all of the ears, between about +48 and +72 Pa. A notable change in G2R is its strong sliding motion at −430 Pa that changes its displacement pattern and causes more difference between the loading and unloading parts.

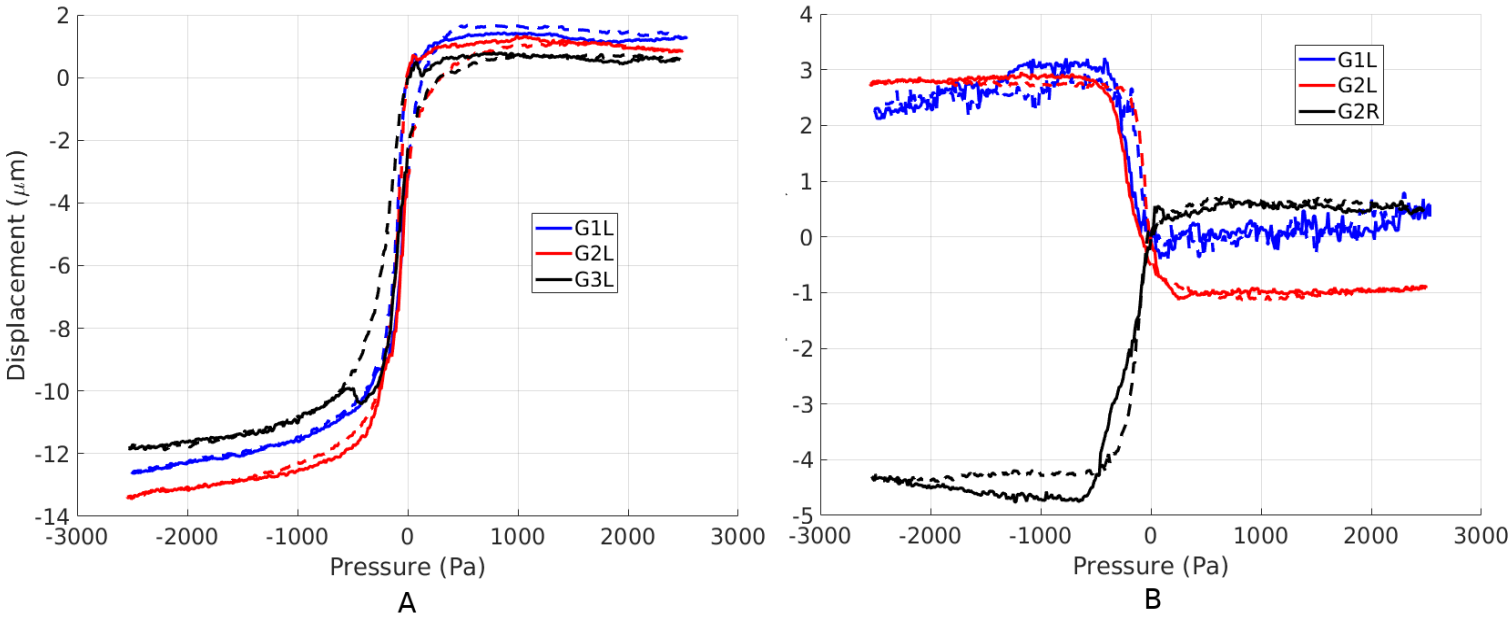

Figure 4.19: Displacements of three cycles of G1L, G2L, and G2R.A: Horizontal displacements. B: Vertical displacements. Solid lines show loading, and dotted ones unloading.

Figure 4.20 and 4.21 show the stapes displacements of all 10 sets from the three samples in the horizontal and vertical directions, respectively. The stapes almost stops its horizontal displacements above around 200 Pa, and its displacements are small below about −500 Pa. The vertical displacements show a similar behaviour for positive pressures, but for negative pressures the stapes almost stops moving below about −500 Pa.

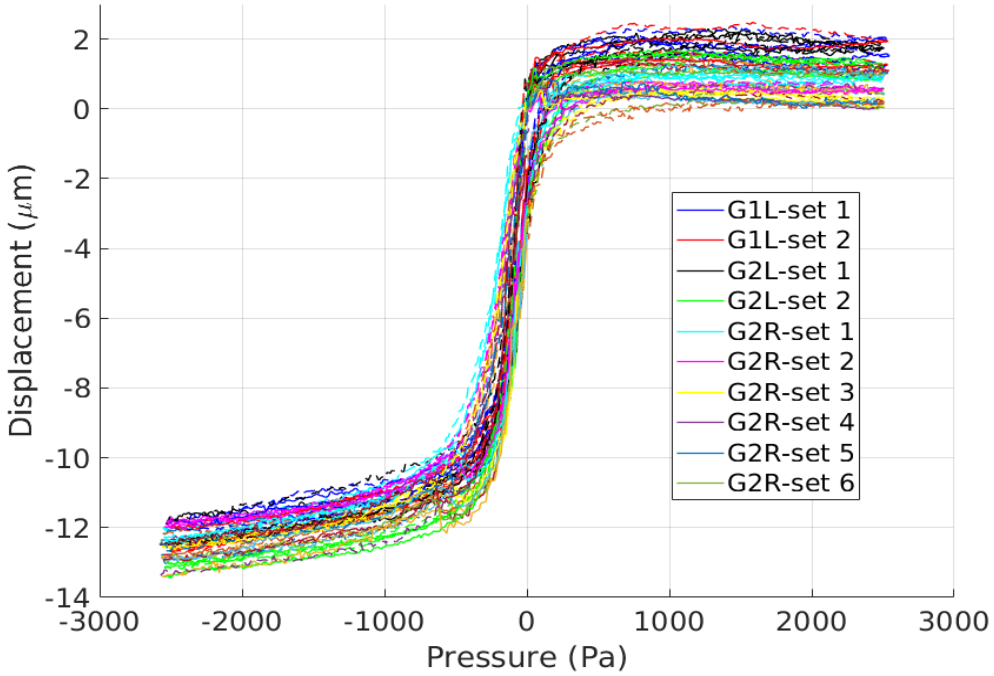

Figure 4.20: Horizontal displacements of 10 sets in all of the samples. Solid lines show loading, and dotted ones unloading.

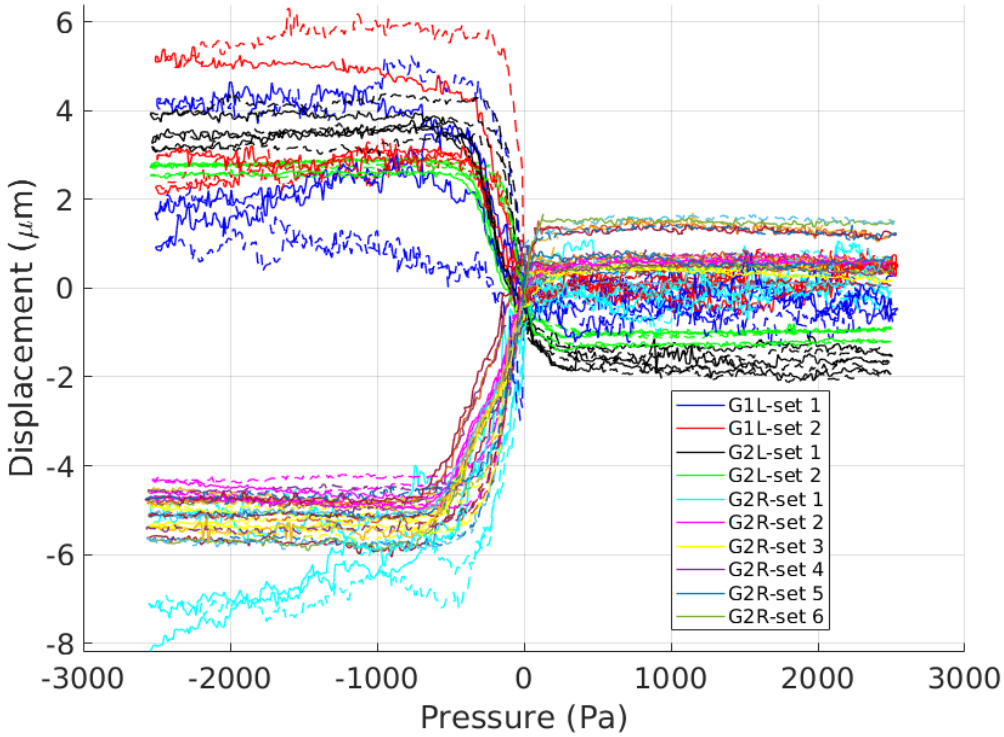

Figure 4.21: Vertical displacements of all 10 sets of the samples. Solid lines show loading, and dotted ones unloading.

The measured peak-to-peak amplitudes of the horizontal displacements of all samples are shown in Table 4. The average of all cycles is 13.4 μm with standard deviation of 0.7 μm. This shows that differences between the range of displacements seen in the figures are mostly changes in the baselines, and the peak-to-peak amplitudes are very similar.

Table 4: Peak-to-peak amplitudes of horizontal displacements for all cycles

		Peak-to-peak amplitude (μm)					
Sample	**Set number**	**Cycle 1**	**Cycle 2**	**Cycle 3**	**Cycle 4**	**Mean±standard deviation**	
G1L	**Set 1**	13	14	14	14	14.1±0.1	14.2±0.1
	Set 2	14	14	14	14	14.3±0.0	
G2L	**Set 1**	15	14	14	14	14.7±0.5	14.6±0.4
	Set 2	13	14	14	14	14.5±0.4	
G2R	**Set 1**	13	13	13	13	13.5±0.1	13.4±0.5
	Set 2	12	12	12	12	12.7±0.1	
	Set 3	13	13	13	13	13.1±0.0	
	Set 4	12	13	12	13	13.0±0.3	
	Set 5	13	13	13	14	13.9±0.2	
	Set 6	14	14	14	13	14.2±0.2	
Mean±standard deviation		13.7±0.9	13.8±0.6	13.7±0.7	13.9±0.6	**13.9±0.7**	

Table 5 shows the peak-to-peak amplitudes of the vertical displacements. The standard deviation of 1.8 μm is greater than for the horizontal results. The first set of G2R shows the highest standard deviation, which corresponds to a bad estimate by the algorithm which is visible in Figure 4.21.

Table 5: Peak-to-peak amplitudes of vertical displacements for all cycles

		Peak-to-peak amplitude (µm)					
Sample	**Set number**	**Cycle 1**	**Cycle 2**	**Cycle 3**	**Cycle 4**	**Mean±standard deviation**	
G1L	**Set 1**	5	6	6	6	6.3±0.3	5.7±1.2
	Set 2	6	6	3	4	5.2±1.6	
G2L	**Set 1**	6	5	6	6	6.3±0.4	5.1±1.3
	Set 2	3	4	4	4	3.8±0.4	
G2R	**Set 1**	6	7	8	10	8.2±1.8	6.4±1.1
	Set 2	5	5	5	5	5.6±0.2	
	Set 3	5	6	5	6	6.0±0.2	
	Set 4	5	5	5	5	5.6±0.4	
	Set 5	6	6	6	6	6.7±0.1	
	Set 6	6	6	6	6	6.6±0.1	
Mean±standard deviation		5.8±1.1	6.2±0.9	5.9±1.3	6.2±1.8	**5.7±1.8**	

Finally, the differences between the manual outputs and automatic results are shown in Table 6. On average, the difference between the manual and automatic results is 1.93 µm with its highest value of 4.63 for set 4 of G2R.

Table 6: Differences between the manual data and automatic outputs of the selected point

Sample	**Set number**	**Difference (µm)**	**Average (µm)**	
G1L	**Set 1**	1	1.6±0.0	**1.9±1.0**
	Set 2	1		
G2L	**Set 1**	2	2.0±0.6	
	Set 2	1		
G2R	**Set 1**	1	1.9±1.3	
	Set 2	1		
	Set 3	1		
	Set 4	4		
	Set 5	1		
	Set 6	1		

4.2.2.3 Incudostapedial joint gap changes

At positive ear-canal pressures, the IS joint is compressed and the size of the gap is decreased from its initial 0-Pa value. At negative pressures the joint is stretched and the gap between the LP and stapes is increased. These changes in the IS joint's gap can be estimated by subtracting the stapes displacements from the LP displacements. The result starts from 0, and a negative value shows the amount of decrease in the initial length of the gap, and a positive value means the joint is stretched and its initial length is increased by that value.

Figure 4.22 shows the changes of the gap as a function of time and pressure in one pressurization cycle for G2L. From the beginning of the motions of the LP and stapes, the joint is compressed and the gap length is reduced to about 2 μm less than its initial size. At the negative loading pressures, however, the gap is stretched and reaches about 3 μm more than its initial size. Then in the negative unloading part, it returns to its initial value non-linearly, with a slight increase at first.

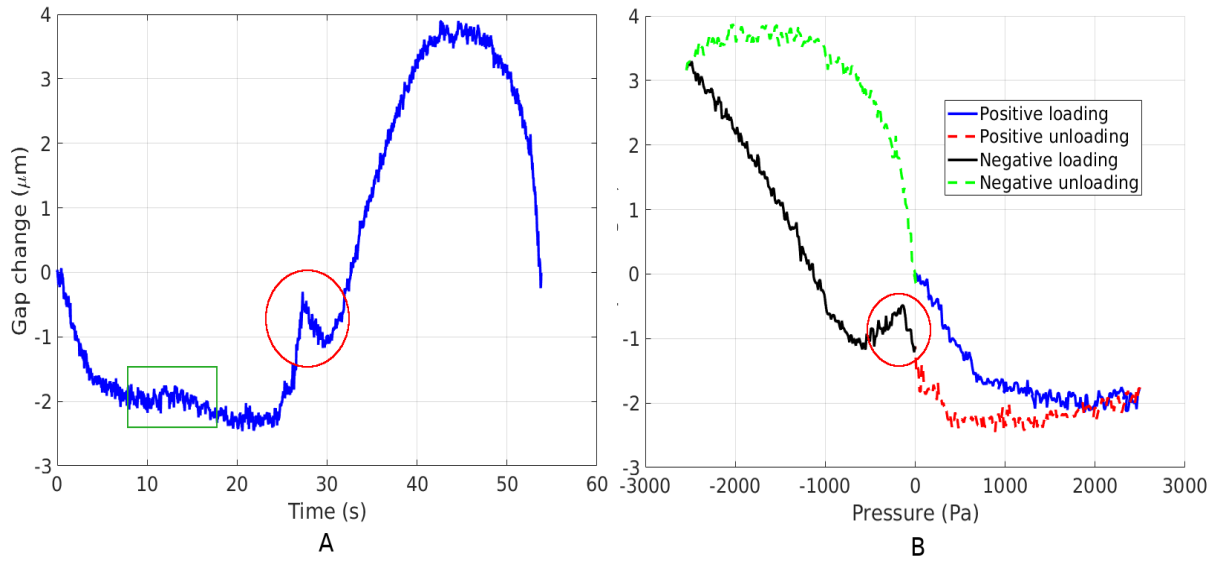

Figure 4.22: Changes of the IS joint gap of G2L. A: as a function of time. B: changes as a function of pressure. Red circles indicate the sliding-motion effect, and the green rectangle in A indicates a possible TM buckling effect. Solid lines show loading, and dotted ones unloading.

The result of the stapes sliding motion on the IS joint gap is visible in the red circles in the negative loading parts, which shows that the stapes and LP do not have the same sliding motion along the horizontal axis, which would cancel out the effect on the IS joint gap. There is also a slight hint of the TM-buckling effect at the joint, indicated by the green rectangle; this might be caused by inaccuracy of the tracking results for the LP and stapes.

Figure 4.23 shows changes of the gap within a set for G2L. We see a difference in the first cycle, and then after that the gap changes consistently between about −2.5 and 4 μm. Figure 4.24 shows these changes as a function of pressure. As can be seen, except for the first cycle (preconditioning), the pattern of the gap changes in this set are consistently repeated. Because we subtracted the LP and stapes displacements, which have the same signal drift, for gap changes we do not need to correct each cycle separately.

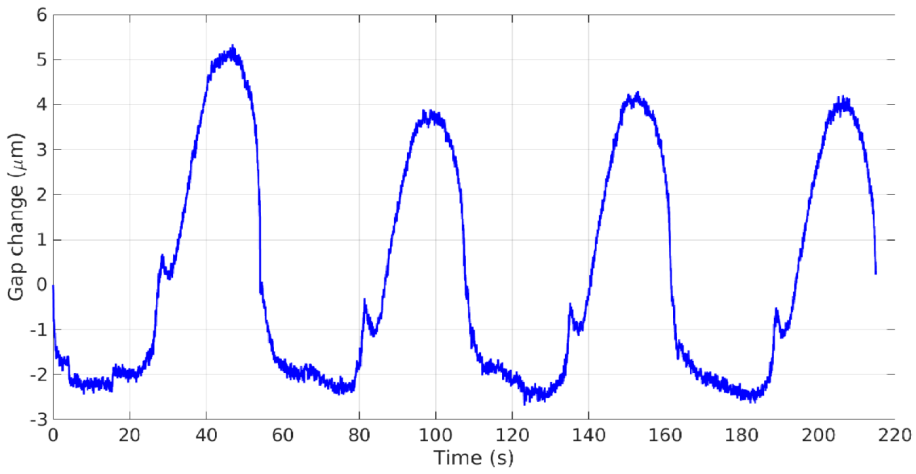

Figure 4.23: Gap changes in one set of G2L versus time.

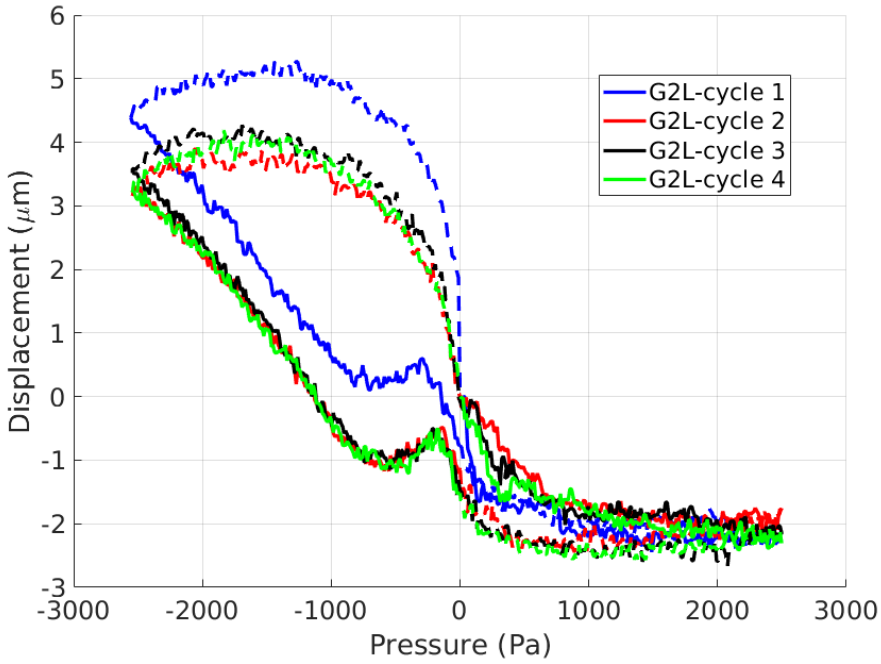

Figure 4.24: Gap changes of one set in G2L versus pressure. Solid lines show loading, and dotted ones unloading.

Both of the two sets for G2L are shown in Figure 4.25. In the first set (blue), the displacements of the stapes in the second set shows a significant difference, which we think might be inaccuracy in the displacement estimation, or a transient effect, since the other cycles are consistent among themselves.

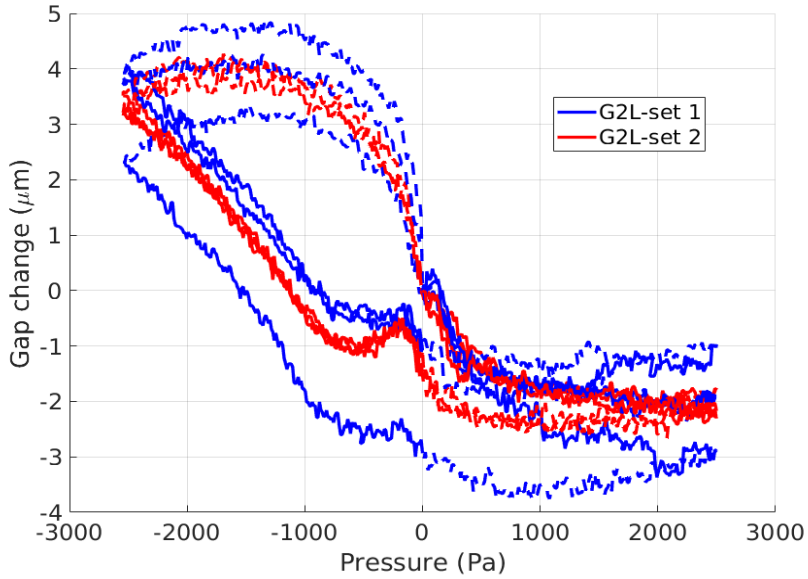

Figure 4.25: The gap changes in G2L for two sets. Solid lines show loading, and dotted ones unloading.

All 6 sets of G2R are shown in Figure 4.26. As mentioned earlier, measurements of the 6th set were done without humidification, which might be the reason for the differences in its pattern, associated with the drying of the sample. Other than that, there is a cycle in the 4th set which shows a different negative loading pattern in one cycle. This change originates from a bad approximation of the stapes displacement, in which the algorithm could not find the correct result.

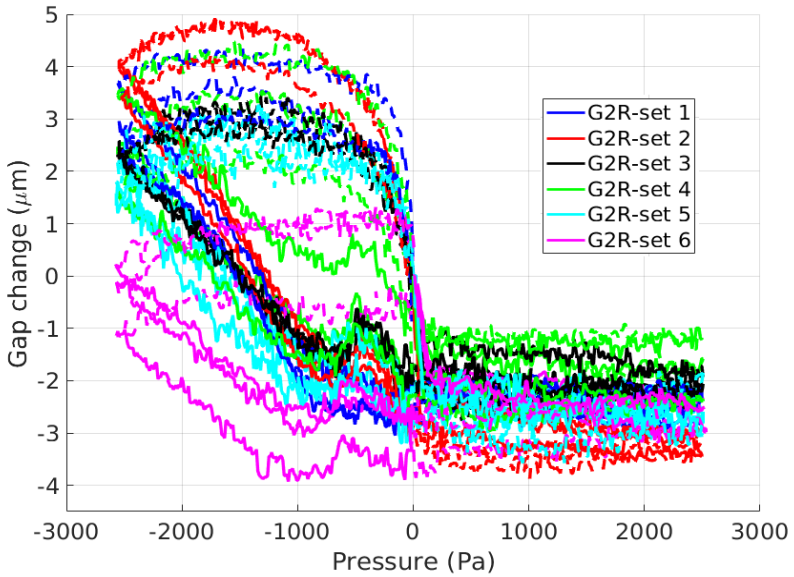

Figure 4.26: Gap changes in 6 sets of G2R. Solid lines show loading, and dotted ones unloading.

Th two sets of pressurization for G1L are shown in Figure 4.27. The gap is compressed to about 2 μm less than its initial value for positive pressures, and is stretched to about 6 μm greater than its initial value for negative pressures. The sets are quite consistent with small variations in the baselines.

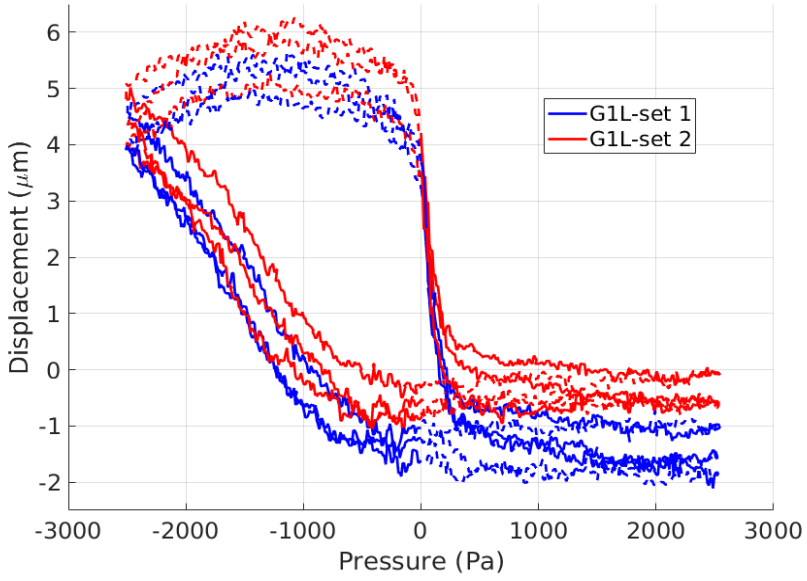

Figure 4.27: The gap changes of two sets of G1L. Solid lines show loading, and dotted ones unloading.

Figure 4.28 shows the second cycle of G1L, G2L, and G2R. The patterns and the amplitudes are similar among all samples.

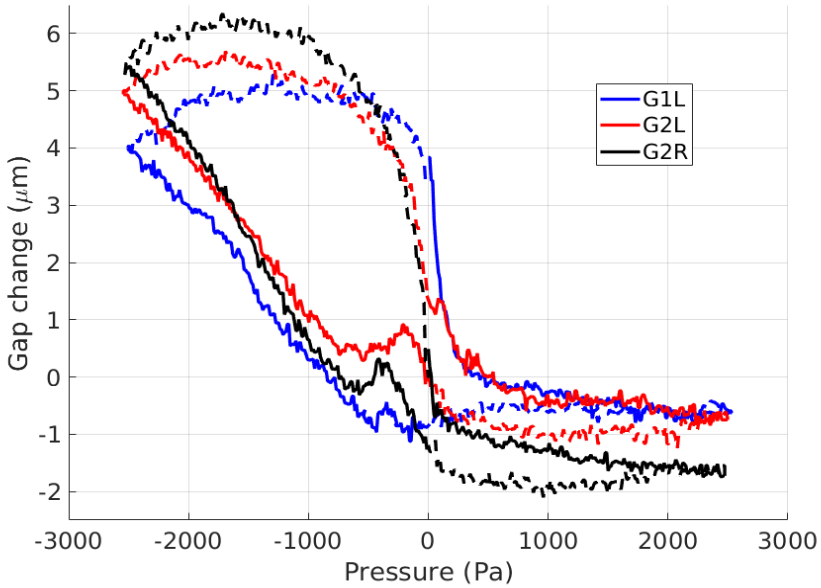

Figure 4.28: Three cycles of G1L, G2L, and G2R. Solid lines show loading, and dotted ones unloading.

Figure 4.29 shows all cycles of 10 sets in all samples. The gap changes range between about −2 and 6 µm, which means that the joint stretches by up to 8 µm from its compressed position.

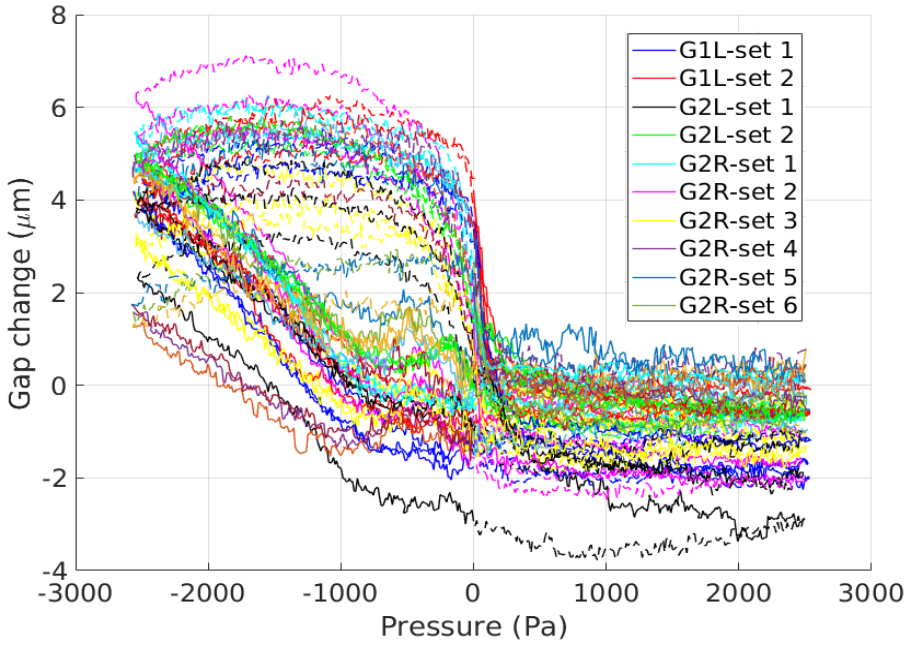

Figure 4.29: All sets of G1L,G2L,and G2R. Solid lines show loading, and dotted ones unloading.

Peak-to-peak amplitudes were also measured and the results are presented in Table 7. The average and standard deviation of all peak-to-peak amplitudes are 6.6±1.1 µm. The 6th set of G2R has a lower amplitude which might indicate that the middle ear was dried and the movements were limited. If those data are eliminated from our calculations, the average amplitudes of G2R would be 6.7 µm instead of 6.3 µm, and the total average would change to 6.9 µm.

Table 7: The peak-to-peak amplitudes of gap changes in all sets

		Peak-to-peak amplitude (μm)					
Sample	**Set number**	**Cycle 1**	**Cycle 2**	**Cycle 3**	**Cycle 4**	**Mean±standard deviation**	
G1L	**Set 1**	7	7	7	6	7.3±0.6	7.1±0.5
	Set 2	7	6	6	7	6.8±0.4	
G2L	**Set 1**	7	7	7	6	7.1±0.6	7.0±0.5
	Set 2	7	6	6	6	7.0±0.5	
G2R	**Set 1**	6	6	7	6	6.7±0.3	6.3±1.2
	Set 2	8	8	8	8	8.4±0.2	
	Set 3	6	6	6	5	6.0±0.2	
	Set 4	6	6	6	5	6.1±0.5	
	Set 5	6	6	6	6	6.4±0.3	
	Set 6	4	4	3	4	4.2±0.2	
Mean±standard deviation		7.0±1.1	6.6±1.0	6.6±1.2	6.2±0.9	**6.6±1.1**	

4.2.3 Lenticular-plate and stapes sliding motion

We noticed a subtle disturbance in the motion of the stapes and LP happening when the ear-canal pressure passed either from negative to positive, or from positive to negative values. In Figure 4.30, for each of the three ears, two frames of a video, about 1 s apart, are overlaid such that the first channel of the image is the green channel of the first frame, the second channel of the image is the green channel of the second frame, and the third channel of the image is again the green channel of the first frame. This image shows the LP and stapes positions before and after this motion when the pressure is changing from positive (the IS joint is compressed) to negative (the IS joint is stretched). The magenta and green shadows show differences between the two frames. The green colour indicates the parts that are only in the second frame, and the magenta indicates the parts that are only in the first frame. Thus, we see from this viewing angle that the stapes was sliding on the LP surface toward the side opposite the stapedial tendon attachment in all three samples (i.e., downward in panels A and C, upward in panel B). Then,

right after this motion, a sudden movement of the LP was observed that is probably caused by the abrupt stapes sliding motion. Unlike the sudden sliding motion shown here for the positive-to-negative direction of the pressure change, the stapes head returned gradually when the pressure changed from negative to positive.

We roughly measured the abrupt vertical motions of the stapes head in the positive-to-negative transition to obtain the magnitude of this sliding motion. These changes were about 5.6 μm for G1L, 4 μm for G2L, and 6.4 μm for G2R.

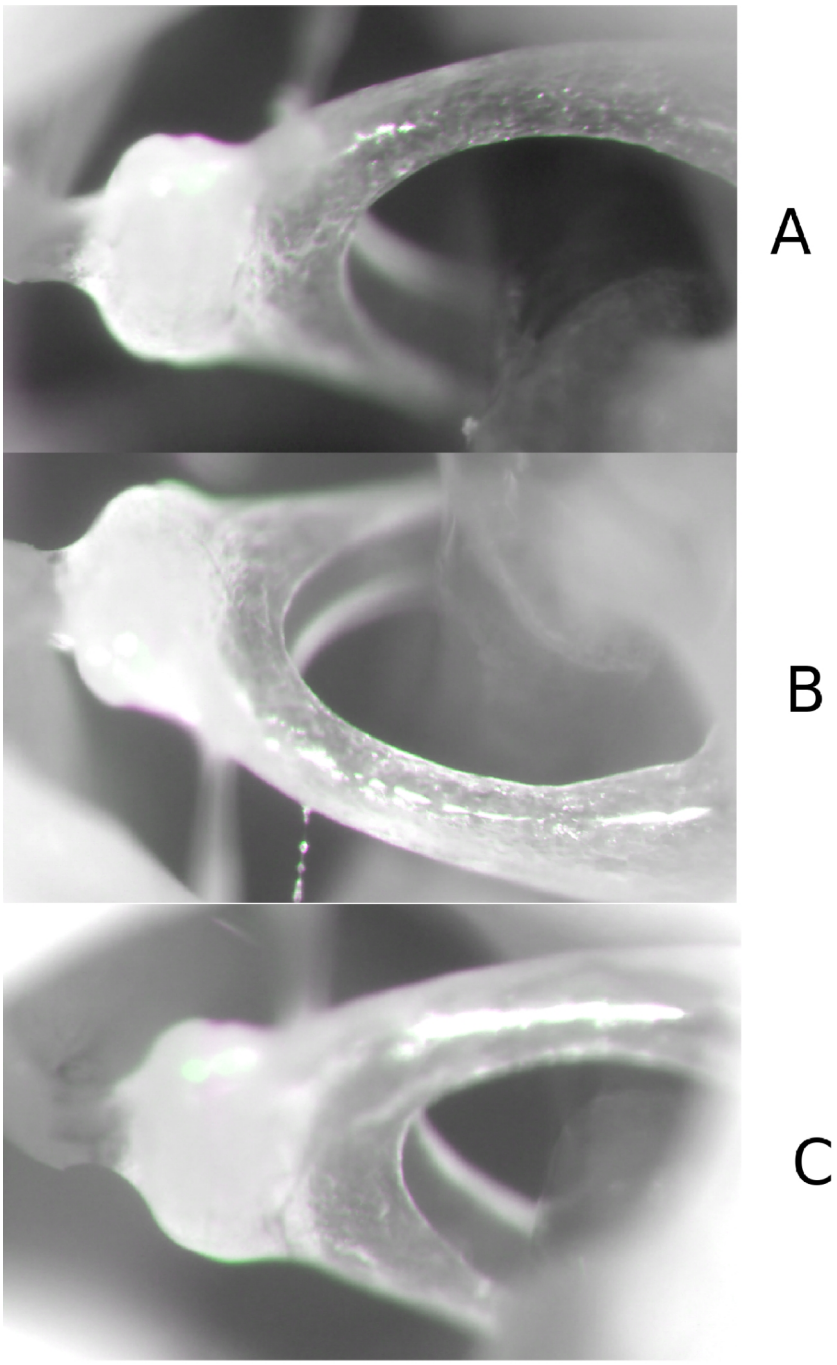

Figure 4.30: Overlaid frames of a video showing subtle movement of the stapes in the opposite direction of the stapedial tendon attachment. A is G2L, B is G2R, and C is G1L. Note the opposite places of the green and magenta shadows in the left and right ears showing the same sliding direction in all samples.

4.3 NanoCT scan

We used 12 middle ears, each scanned at least twice, to develop our final sample-preparation method for the imaging which preserves the joint's shape under static pressures. The results for three samples prepared with the finalized method are presented in this section. Two of them were prepared under 0 Pa (S1, S2) from one animal, and the other was a previously frozen sample prepared under −2500 Pa (S3). All three ears were stained and then scanned, except for S1, which was also scanned before staining. NanoCT parameters that we used to scan these samples are shown in Table 8.

Table 8: NanoCT parameters

Parameters	**Values**
Source voltage	80 kV
Source current	86 µA
Resolution	0.70 µm
Exposure time	10 s
Number of projections	1600
Sample rotation angle	180°
Number of *counts*	4000-5000

4.3.1 Volume rendering

A set of cross-sectional images was loaded into the Dragonfly software and a 3-D model is represented. The field of view is selected so that it covers the full area of the stapes head and LP. Figure 4.31 shows multiple views of the unstained S1 scan in order to visualize the gap clearly.

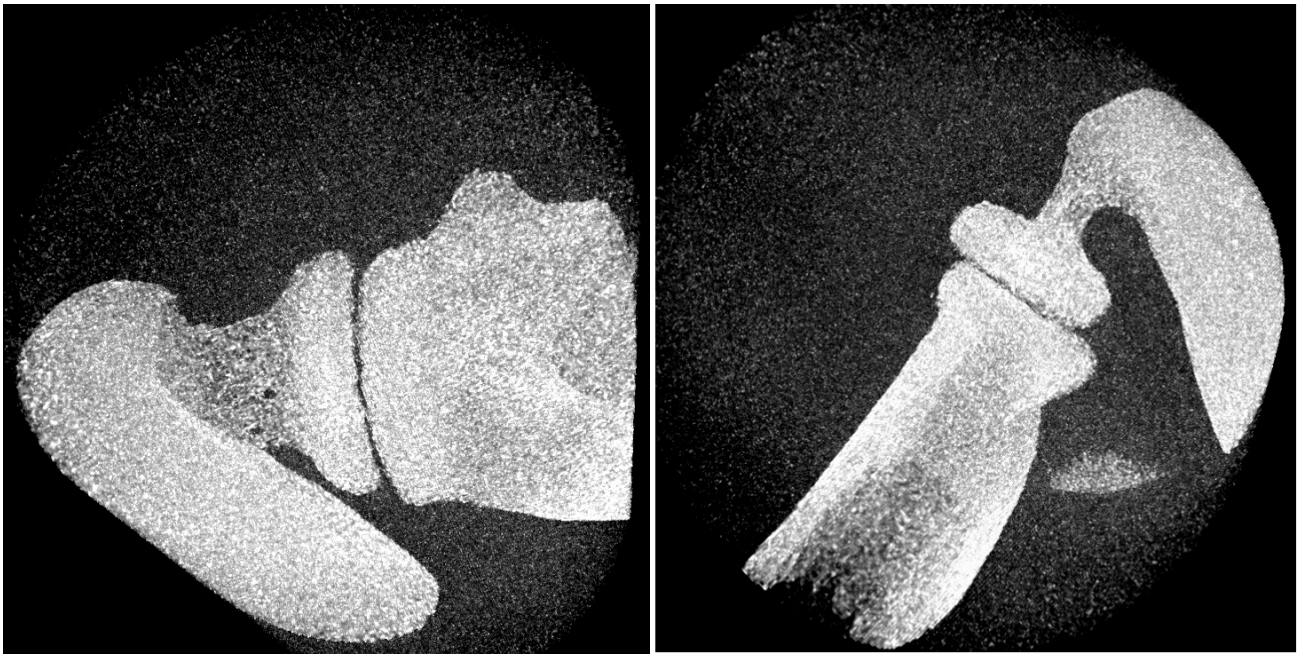

Figure 4.31: Multiple views of the reconstructed 3-D model of S1.

4.3.2 Measurements

We measured the gap in the reference plane as explained in Section 3.4.2. Since there are small variations in the gap size, we measured it at multiple places along the joint as shown in Figure 4.32 for S1. (The curved lines on the upper side of the pedicle in the S1 and S2 scans are the remains of the ethanol used to rinse samples after staining.)

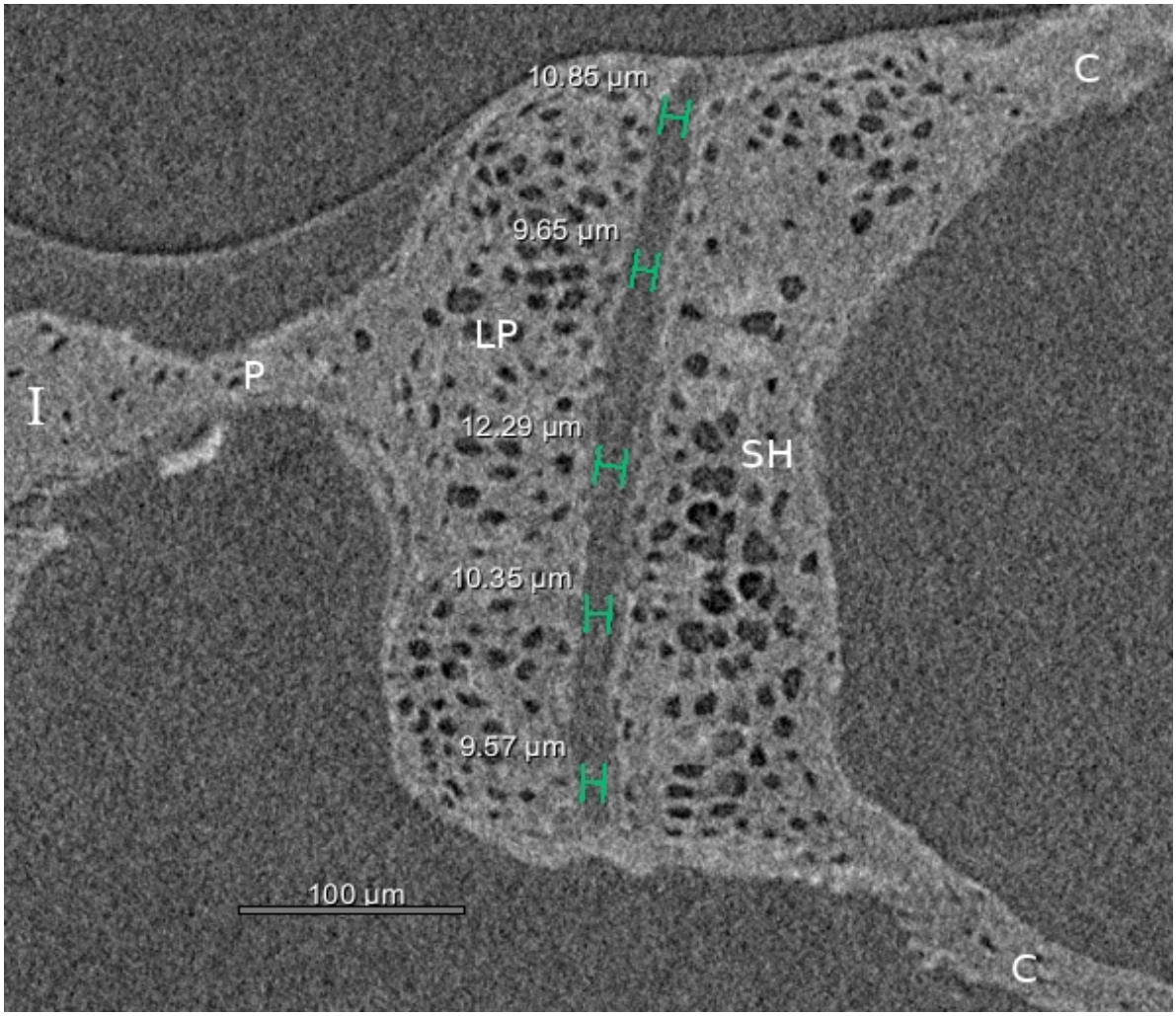

Figure 4.32: The length of the gap in S1 at multiple points. C: crus, SH: stapes head, LP: lenticular plate, P: pedicle, I: incus.

In Figure 4.33, measurements of S2 are shown.

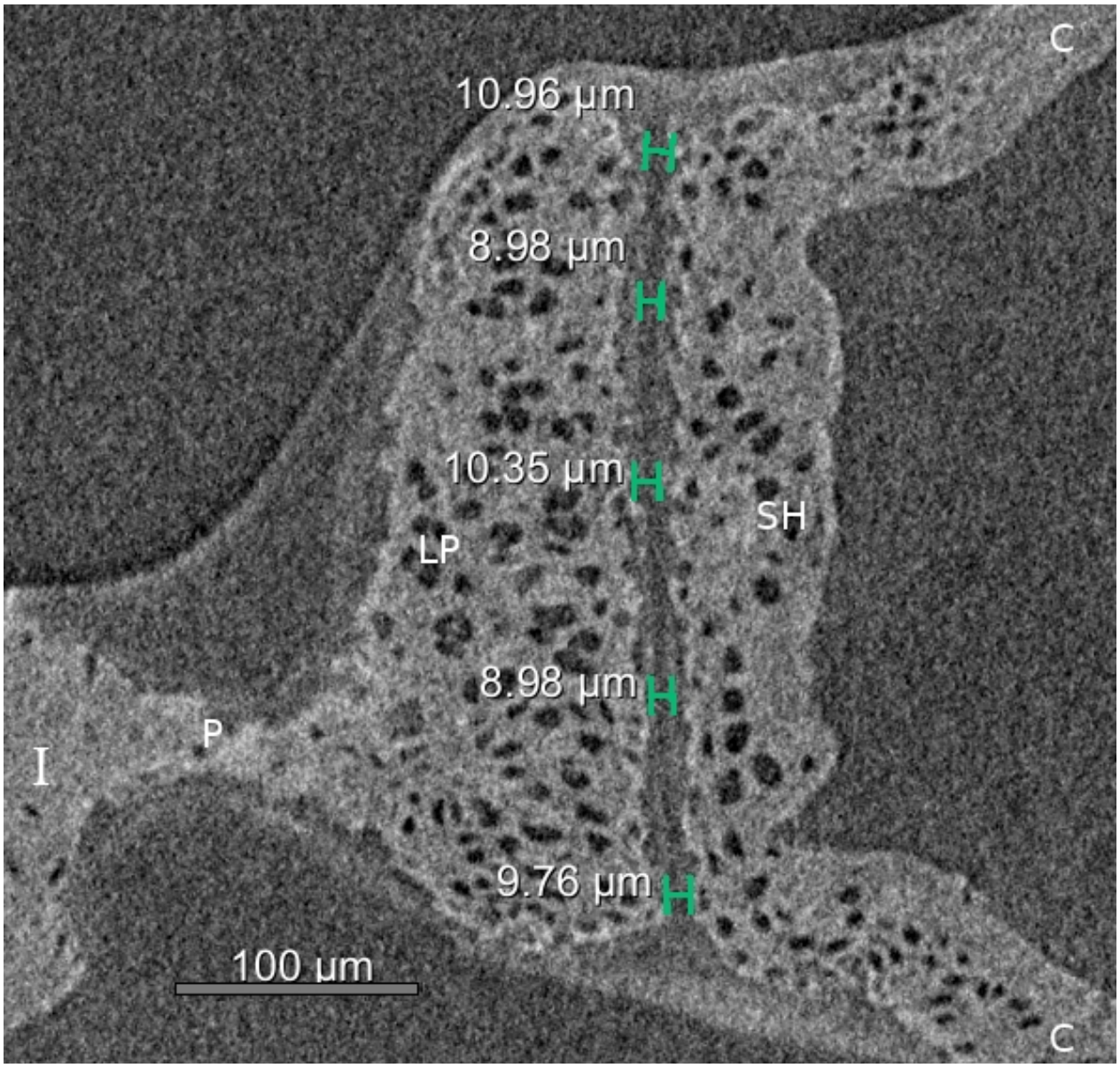

Figure 4.33: The length of the gap in S2 at multiple points. C: crus, SH: stapes head, LP: lenticular plate, P: pedicle, I: incus.

Figure 4.34 shows S3 prepared under −2500 Pa pressure. The capsule is damaged and the gap length is significantly increased.

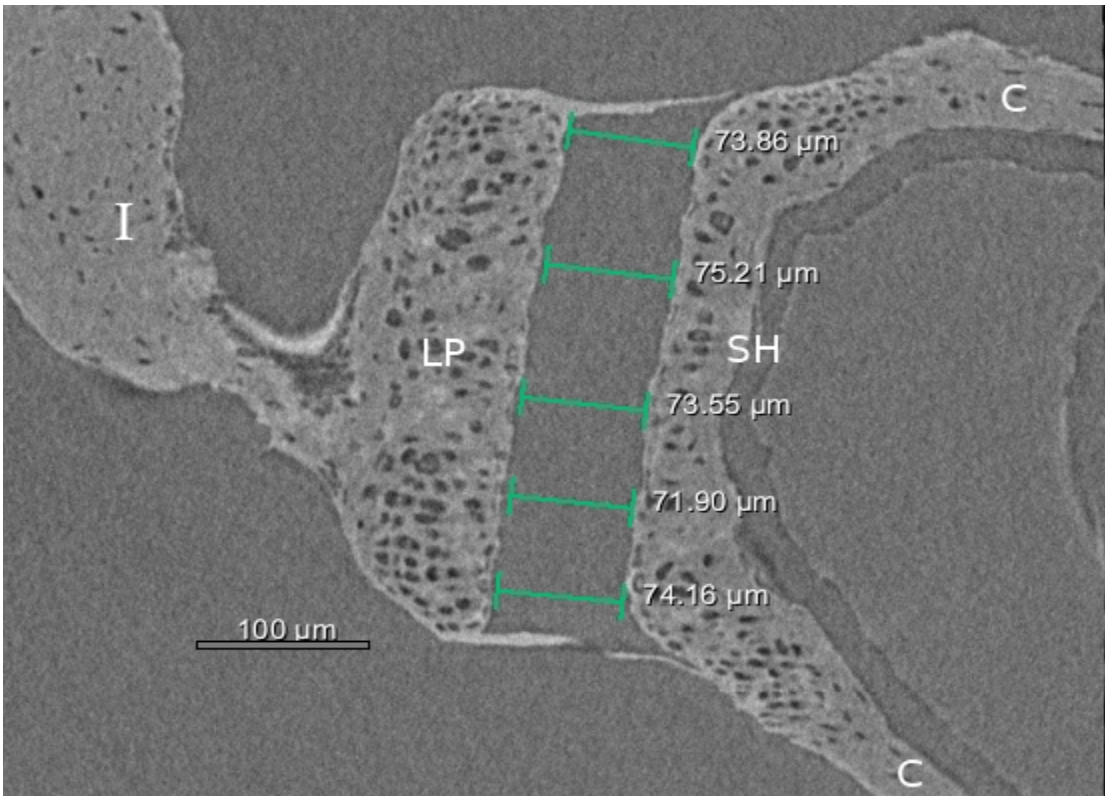

Figure 4.34: The length of the gap in S3 at multiple points. C: crus, SH: stapes head, LP: lenticular plate, P: pedicle, I: incus.

Table 9 shows the gap sizes of the samples in Figures 4.32-4.34. The averages of the two samples prepared under 0 Pa pressure are similar, with a difference of only about 0.8 µm (about 10%).

Table 9: The gap length of S1, S2, and S3

Sample	**Measured gap length (µm)**					**Average**
S1	10	9	12	10	9	10
S2	10	8	10	8	9	9
S3	73	75	73	71	74	73

4.4 Light-sheet microscopy

In order to develop a tissue-clearing method to make a bulla transparent, one sample was used for initial testing. The results for a second ear using the final procedure under 0 Pa pressure (S4) are presented in this section.

4.4.1 Sample preparation results

The tissue-processing procedure described in Section 3.3.2.3 is performed in multiple stages: fixation, polymerization, decalcification, and refractive-index matching. Figure 4.35 shows the sample after each step, with bars behind it to show the amount of sample transparency. The final sample in Figure 4.35C has some remaining red colour, due to red blood cells that are not cleared well in the procedure.

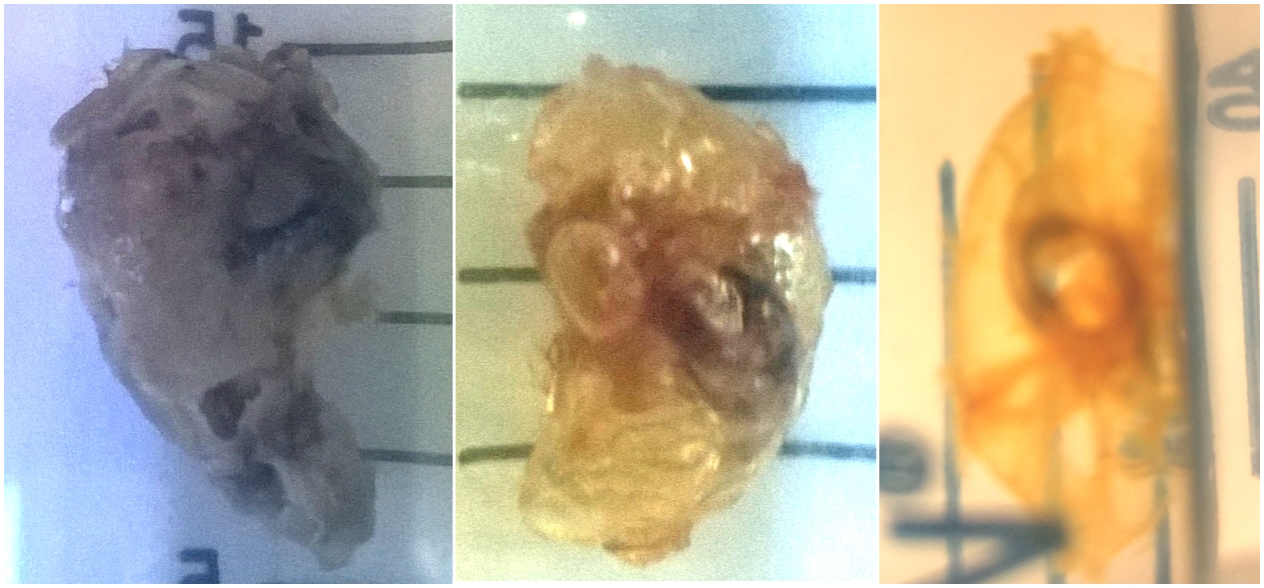

Figure 4.35: Result of each tissue-clearing process. A: After fixation. B: After decalcification. C: After refractive index matching

4.4.2 Light-sheet scans

We used two lasers, red and green, to scan our samples. Figure 4.36 shows the sample prepared at 0 Pa pressure in two different images. The image produced with the green laser is slightly saturated in some areas and details cannot be seen clearly. The joint's capsule and cartilage are distinguishable better in the image prepared with the red laser.

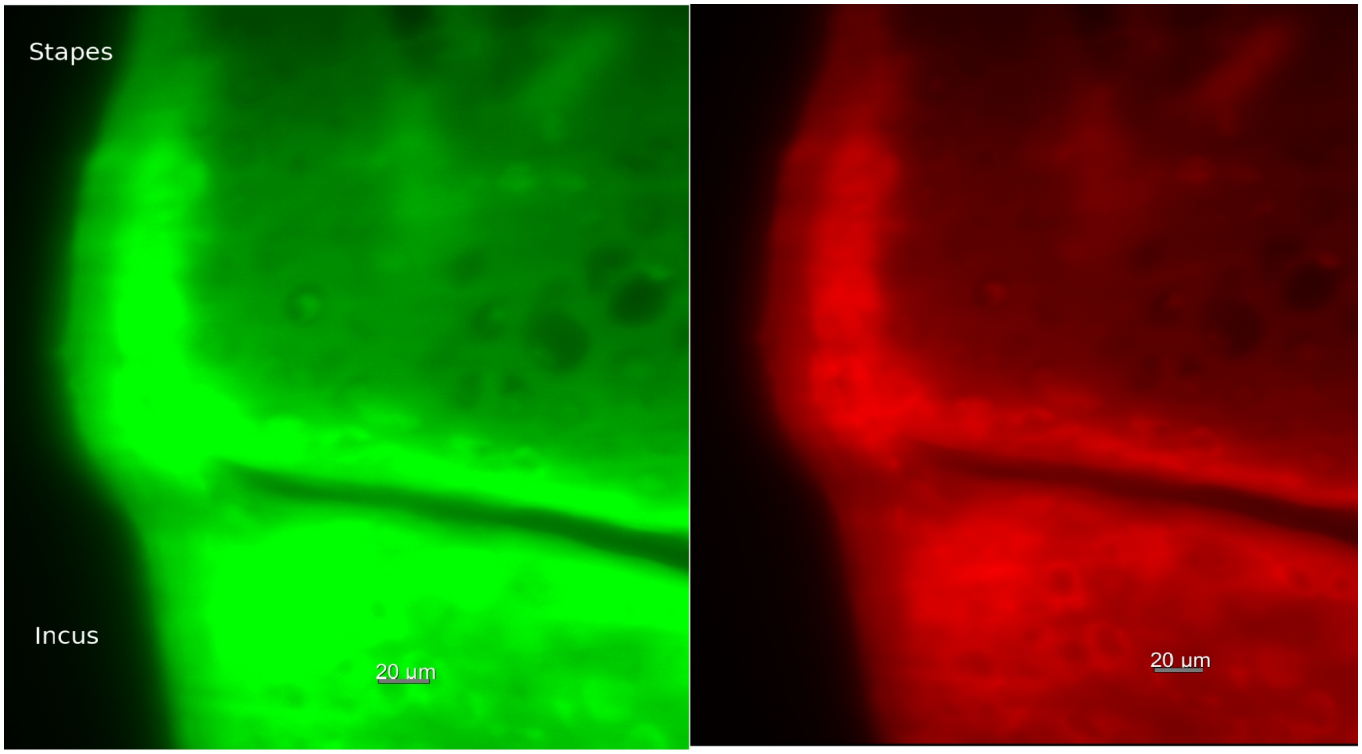

Figure 4.36: Light-sheet scan of S4 prepared under 0 Pa. A: Green laser excitation. B: Red laser excitation.

4.4.3 Measurements

Using Dragonfly we measured dimensions of the joint as shown in Figure 4.37. In addition to the gap size, the thickness of the capsule in the LP and stapes were measured. The gap length is similar to the nanoCT results, ranging between about 11 µm and 8 µm, with an average of 9.1 µm. The capsule thicknesses were very similar at the two measurement locations where the capsule is attached to the stapes and LP, at about 22 µm, and is about 45 µm at the gap.

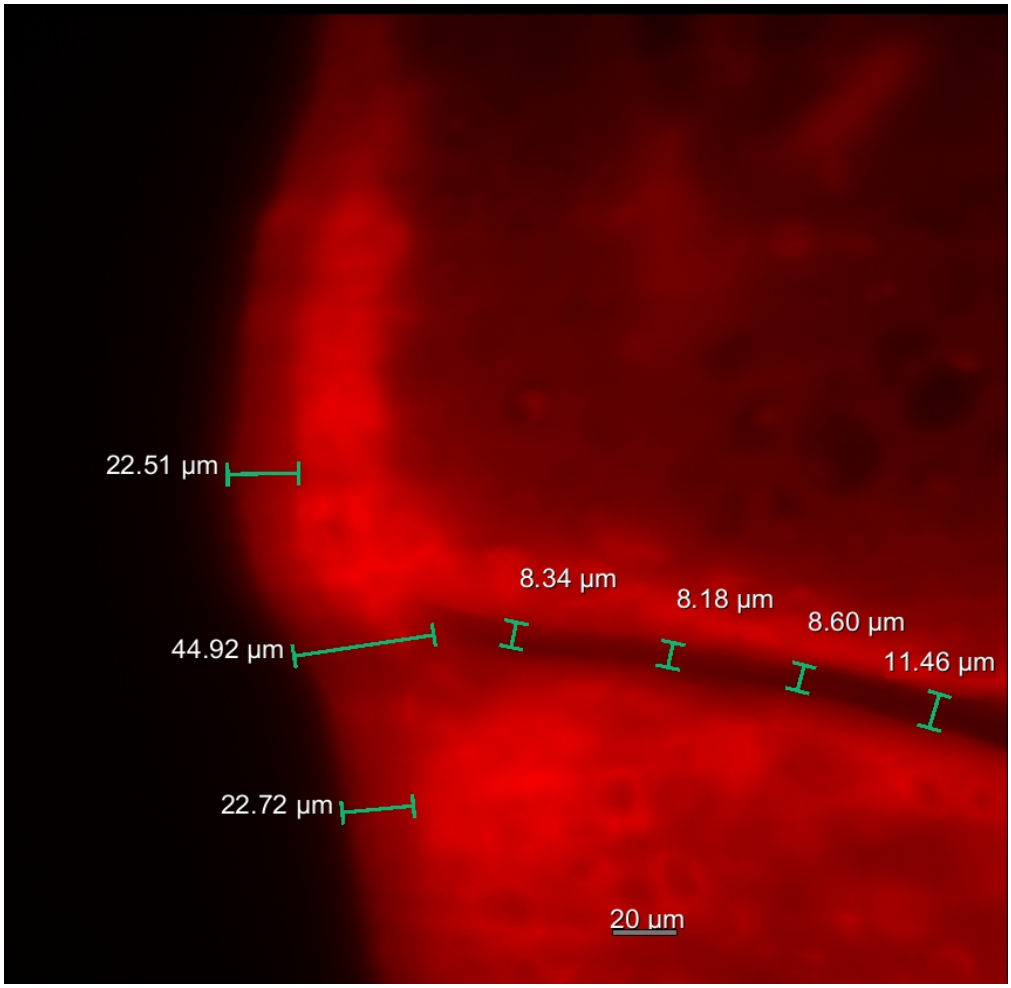

Figure 4.37: Dimensions of the S4 IS joint using light-sheet imaging.

4.5 Discussion

Hüttenbrink (1988) measured displacements of the human ossicles in the intrinsic coordinate reference frame of the stapes by considering the inward/outward (piston-like) direction (a) as one axis, and combining front and rear (b) and upward/downward movements (c) using $\rho=\sqrt{b^2+c^2}$. For positive pressures ranging between 0 Pa and 400 Pa, the maximum incus displacement along (a) was reported to be 8 µm, and for ρ it was 25 µm. For negative pressures, these values were 36 µm and 49 µm respectively. The maximum stapes displacement was reported to be 8 µm for positive pressures in the (a) direction, and 20 µm for negative pressures. These values were 16 and 26 µm for ρ for positive and negative pressures, respectively. He then concluded that the inward/outward displacements of the LP and stapes were predominant. Later,

Gea (2012) measured displacements of the LP and stapes in the same reference frame and compared his results with those of Hüttenbrink, as shown in Figure 4.38. He drew the same conclusion about the dominance of the inward/outward displacements of the LP and stapes.

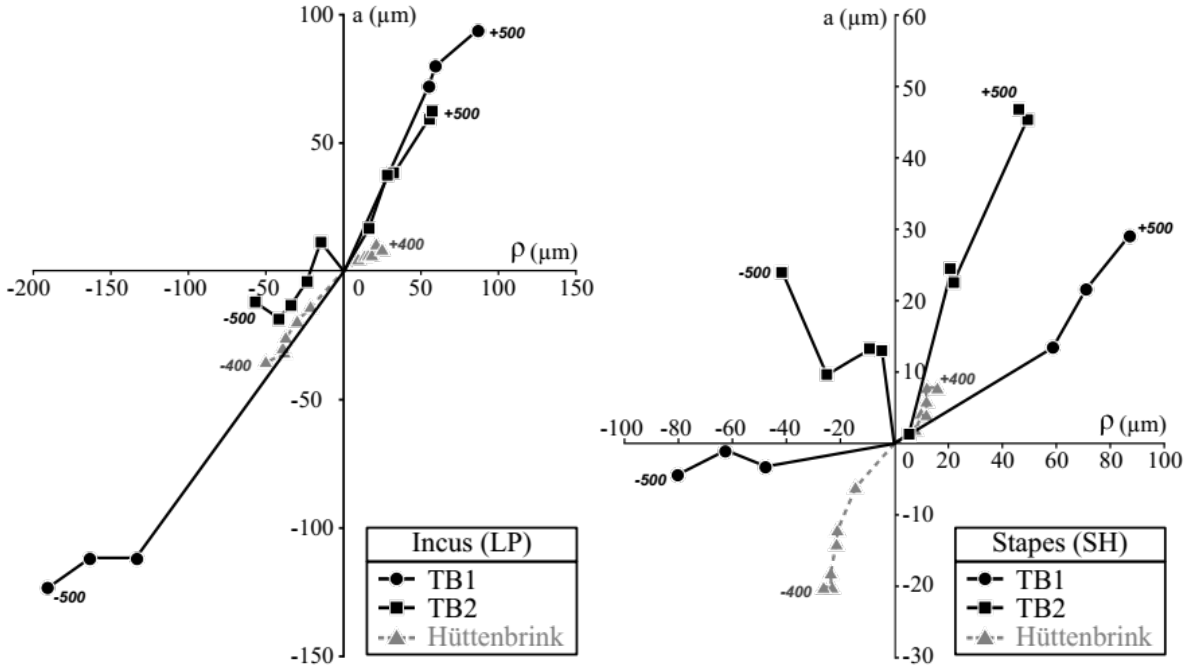

Figure 4.38: Comparison of the LP and stapes displacements measured by Gea (2012) with Hüttenbrink (1988) (Source: Fig. 5.23 of Gea (2012)).

Gea (2012) also measured these displacements for gerbil under step static pressures. He reported a 64-μm displacement in one gerbil in an inward/outward direction for LP, and 25 μm for the stapes. His results are shown in Figure 4.39.

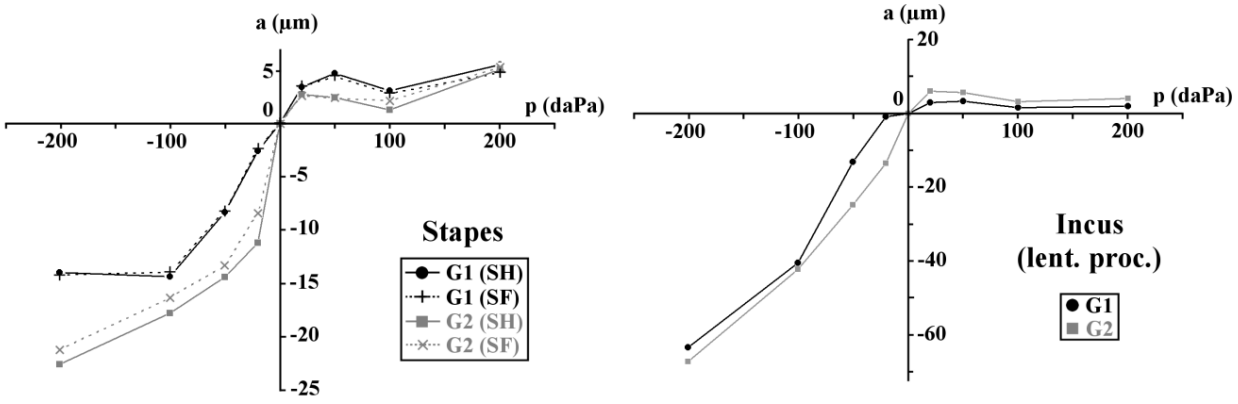

Figure 4.39: Gea's (2012) results of displacements of the stapes (left) and LP (right) as a function of pressure.(Source: derived from Fig. 4.13 Gea (2012))

Also, Salih et al. (2016) reported a 78 µm displacement of the stapes in rabbits under quasi-static pressures with a pattern shown in Figure 4.40.

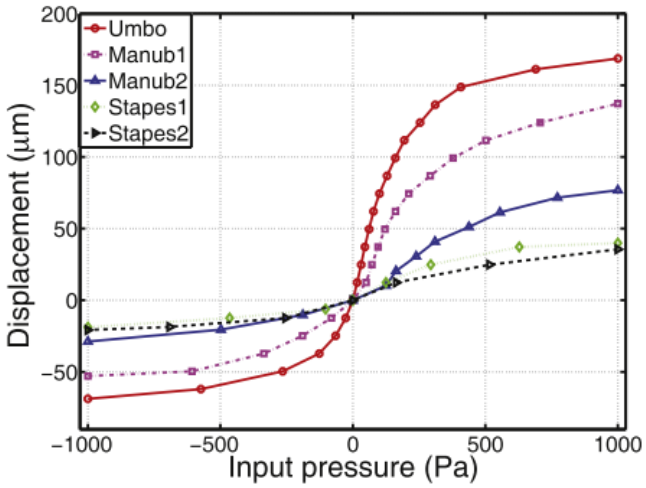

Figure 4.40: Displacements of the umbo, manubrium, and stapes under quasi-static pressure at 0.5 Hz (Source: derived from Fig. 8 of Salih et al. (2016)).

To the best of our knowledge, there has been no displacement-measurement study that was conducted under ramp static pressures, since a method is needed that is able to track fast-changing motions. Our results show that the LP has a linear behaviour for negative loading pressures and a non-linear behaviour for negative unloading pressures and for positive pressures. The linear and non-linear patterns for negative pressures are not comparable with other findings, possibly since all of them used step pressures. For positive pressures, the non-linearity in the loading and unloading parts is also observed in Gea's measurements in gerbil. We measured 19.6

μm for the average LP displacement, which is about a third of Gea's measurements with step pressures. We think that a part of the difference might be because of a small difference in the measurement axes. Another possible reason is based on our observations when we used a step pressure: after a few cycles of pressurizing with a step pressure signal, we saw an abrupt elongation of the joint, with a bubble inside the synovial space which might be an indication of the breakage of the capsule. The LP moved over a much larger range than in the preceding pressurization cycles. The displacement results are not included here, since they were a part of the tests made while developing the final experiment setup. However, the nanoCT scan discussed in Section 4.3.2, that was prepared at −2500 Pa, displays a broken joint capsule and shows displacement results similar to those reported by Gea.

In previous work by Gea and by Salih, a strong non-linearity was observed in stapes displacements, which is consistent with our findings. The pressure resolution in the previous work was not good enough to find the exact threshold where the stapes starts to have very small movements, but we found that it roughly happens at pressures above 200 Pa and below −400 Pa. The amplitude of the stapes displacement range in Gea's work was reported as 25 μm. In our measurements its average is 13.85 μm. The difference is not as significant as for the LP, and we think it may be mostly because of the different pressurization signals that were used.

Gea reported an average 10-μm distance for the synovial gap in its rest state, which is also confirmed in our findings by nanoCT and light-sheet scans at 0 Pa. However, he found that this gap broadened to an average distance of 56 μm under static pressures from its initial 10 μm gap size. We measured 6.6 μm as the full range of its changes from a full compression at 2500 Pa to a full tension at −2500 Pa. This difference might again be related to the observation of the capsule breakage that we made for step pressures. More studies need to be done on changes of the IS joint under step pressures.

A notable observation is the sliding motion of the LP and stapes which happens around 70 Pa and −400 Pa, with varying amplitudes of around 5 μm in different ears. This motion takes place in less than a second. Its transient effects on displacements of the LP and stapes are considerable, but affects on the behaviour of the LP and stapes afterward are not clear.

Based on the promising results of our nanoCT scans and light-sheet images, we think our sample-preparation method is effective in preserving the shape of the IS joint under static pressures. The gap length in both nanoCT scans and light-sheet images is about 10 μm in three different samples prepared at 0 Pa. To the best of our knowledge, there has not previously been any sample-preparation method specifically developed to investigate the changes of the IS joint on a microscopic scale. Further experiments under different static pressures should be done to obtain more information about the IS joint changes. Additionally, improvements need to be made on the tissue-clearing method to eliminate the effects of red blood cells, which make the images blurry and unclear; using perfusion fixation helps remove blood from the animal's body in the first place (Greenbaum et al., 2017) and may be applicable here.

Chapter 5. Conclusion

5.1 Summary

In this study, we developed new techniques to investigate the mechanical behaviour of the LP, stapes and IS joint by measuring their displacements and structural changes at a microscopic level under static pressures. Our work provide new insights into middle-ear mechanics, and offer new approaches to investigating its behaviour.

First, we modified our existing pressurization system to produce an accurate ramp pressure signal. Then, an experiment was designed in which displacements of the LP and stapes under static pressures were recorded using a microscope and a video camera. The preparation procedure for the experiment included making a hole in the bulla, inserting the pressurization tube in the ear canal, and sealing the ear-canal opening using dental cement. A set of pressurizations was defined which consisted of four consecutive ramp signals with a constant pressurization speed between 180 Pa/s and 360 Pa/s. A pressure ramp signal consisted of loading and unloading parts for both positive and negative pressures, with maximum and minimum values of +2500 Pa and −2500 Pa. Each ear was pressurized with at least two sets of ramps with the same speed, while displacements were being captured by the camera.

We implemented an automatic object-tracking algorithm based on optical flow to extract motions of the LP and stapes from the recorded videos. A single point on the LP or stapes was followed over the duration of the video and its location in each frame was given as an output by the algorithm. The displacements in two directions, horizontal and vertical, were then obtained.

Our pressure-ramp displacement-recording results for the LP showed that for positive pressures it had subtle motions, apparently due to the TM buckling effect, while for negative pressures it showed mostly linear displacements in the loading part but non-linear ones in the unloading part.

Our stapes motion results showed a strong non-linear behaviour in both negative and positive pressures. This finding is consistent with previous results.

We found a sliding motion of the stapes on the LP and consequent effects on the LP displacements and on the IS joint gap. This motion had rapid transient effects on the displacements of the stapes and LP around −400 Pa and +70 Pa with different amplitudes in different ears. Another observation, possibly related to buckling of the TM, was visible in the LP and stapes displacements above about +1200 Pa for the loading and unloading parts for positive pressures.

We used nanoCT and light-sheet microscopy to investigate changes of the joint under static pressures. This involved immobilizing the ossicles using an adhesive while the ear-canal static pressure was kept constant. NanoCT scans were acquired for three ears stained with PTA. The average sizes of the joint gaps in the two samples prepared at 0 Pa were about 10 µm. In the sample at −2500 Pa it was 73 µm, but the IS joint was damaged and elongated abnormally. Light-sheet imaging was performed on a cleared sample prepared at 0 Pa. The size of the joint gap was consistent with our observations by nanoCT and with previous observations. The spatial resolution of the structures visible in the scans was 0.7 µm for nanoCT and 0.2 µm for the light-sheet microscope.

5.2 Future work

Our study can be extended in three areas: experiment, imaging method, and software. Three ears were used to acquire our data in this study. In future, more samples should be used to confirm the repeatability of our results. (At the time of writing this thesis, two more ears have been measured. Their preliminary results show similar patterns, with small variations in the transient sliding-motion effect).

In this study, we measured displacements of the LP and stapes in post-mortem animals. Important limitations that prevented an in-vivo experiment were the places where the holes were

drilled in the bulla (close to important blood vessels), and a steep viewing angle that required decapitation of the animal. Perhaps an endoscope could be used in vivo to indirectly observe the joint. In our experiment, the middle ear dried quickly because of the holes made in the bulla. A transparent covering might be designed to close the openings, without reducing the quality of the videos. We observed considerable changes happening between +1000 Pa and −1000 Pa; an experiment with a smaller pressure range, slower speeds and better pressure resolution could be conducted to capture all of the changes in this range. We performed measurements with different speeds between 180 Pa/s and 360 Pa/s, but no significant change was observed in this range; a larger speed range could be used to investigate the effects of speed on the displacements.

Our object-tracking method showed promising results in obtaining displacements. It can be applied to other middle-ear structures such as the eardrum, to investigate their motions under static pressures. Currently, an important limitation of our method is that it records displacements in 2D, not 3D. Stereoscopic microscopes have shallow depth of field at high magnifications. This could be used as an advantage to estimate the depth of objects, and consequently movements in the third dimension. Our method tracks a single point in the video, but it could be extended to track multiple points, and ultimately provide a displacement map of the whole object. In order to improve accuracy and to measure motions in a third direction, tiny markers with a size of around a few microns could be placed on an object and used in the tracking algorithm.

Our object-tracking algorithm is based on calculating optical flow using the Lucas-Kanade algorithm. More accurate methods, such as convolutional neural networks (CNN) (Ilg et al., 2017), could be implemented to improve the displacement estimation. Currently, we select the best point to use by comparing multiple points with manual data. It would be desirable to develop a reliable automatic algorithm, to remove any dependency on user input.

5.3 Significance

This study provides a couple of outcomes that are beneficial for middle-ear studies. First, our technique of using a video camera to record motions, and extracting displacement information by implementing image-processing algorithms, had not been employed before in middle-ear studies. We could observe and measure the subtle sliding motion of the LP and stapes in 2D with a high precision, something about which there was little information previously.

Our displacement measurements of the LP and stapes can be directly used to validate finite-element models of the middle ear, and of the IS joint in particular. To the best of our knowledge, these results are the first that provide a high temporal and spatial resolution, and also the first experiment in which a ramp pressure signal was used for the pressurization. This method can also be used in other displacement measurements in the middle ear.

Second, the sample-preparation method developed for our microstructural study is the only method to date that has been proposed to preserve the shape of the IS joint for a long time and under any tissue-processing procedure.

This was the first time that nanoCT was used to study the IS joint microstructure under static pressures. We could observe details of the joint in an X-ray scan that were not reported in other studies. Moreover, the spatial resolution that we achieved for the IS joint with light-sheet microscopy had not been reported in other studies.

Finally, in addition to helping to understand gerbil hearing mechanics, the proposed measurement method using an optical microscope, a camera and optical-flow processing can be translated to human cadaver studies, to give us accurate information about structural properties and natural displacements of the middle-ear components. Based on the data obtained from such studies, and subsequent improvements in our understanding, the status of the middle ear may be better assessed in clinical tests such as tympanometry. Pathological studies of middle-ear disorders can also benefit from the methods developed here.

References

Achromatic lens. (2019). In *Wikipedia*. Retrieved from https://en.wikipedia.org/w/index.php?title=Achromatic_lens&oldid=908080287

Allen, J. R. (n.d.). Light sheet fluorescence microscopy [Nikon]. Retrieved August 1, 2019, from https://www.microscopyu.com/techniques/light-sheet/light-sheet-fluorescence-microscopy

Anderson, C. H., Bergen, J. R., Burt, P. J., & Ogden, J. M. (1984). *Pyramid methods in image processing*.

Bancroft, J. D. (2018). *Theory and practice of histological techniques* (8th ed.). Elsevier Health Sciences.

Berg, J. M., & Dallas, T. (2008). Peristaltic pumps. In D. Li (Ed.), *Encyclopedia of Microfluidics and Nanofluidics* (pp. 1626–1633). https://doi.org/10.1007/978-0-387-48998-8_1198

Blayney, A. W., Williams, K. R., & Rice, H. J. (1997). A dynamic and harmonic damped finite element analysis model of stapedotomy. *Acta Oto-Laryngologica*, *117*(2), 269–273.

Bradel, S., Doniga-Crivat, L., Besdo, S., Lexow, F., Fehr, M., Lenarz, T., … Brandes, G. (2017). Innovative 3D model of the human middle ear in high resolution with a histological microgrinding method: A feasibility study and comparison with µCT. *International Journal of Otolaryngology*, *2017*. https://doi.org/10.1155/2017/6753604

Bushberg, J. T., Seibert, J. A., Leidholdt, E. M., & Boone, J. M. (2011). *The Essential physics of medical imaging*. Lippincott Williams & Wilkins.

Buytaert, J. A. N., & Dirckx, J. J. J. (2007). Design and quantitative resolution measurements of an optical virtual sectioning three-dimensional imaging technique for biomedical

specimens, featuring two-micrometer slicing resolution. *Journal of Biomedical Optics*, *12*(1), 014039. https://doi.org/10.1117/1.2671712

Buytaert, J. A. N., & Dirckx, J. J. J. (2009). Tomographic imaging of macroscopic biomedical objects in high resolution and three dimensions using orthogonal-plane fluorescence optical sectioning. *Applied Optics*, *48*(5), 941–948. https://doi.org/10.1364/AO.48.000941

Buytaert, J. A. N., Goyens, J., Greef, D. D., Aerts, P., & Dirckx, J. (2014). Volume shrinkage of bone, brain and muscle tissue in sample preparation for micro-CT and light sheet fluorescence microscopy (LSFM). *Microscopy and Microanalysis*, *20*(4), 1208–1217. https://doi.org/10.1017/S1431927614001329

Buytaert, J. A. N., Salih, W. H. M., Dierick, M., Jacobs, P., & Dirckx, J. J. J. (2011). Realistic 3D computer model of the gerbil middle ear, featuring accurate morphology of bone and soft tissue structures. *JARO: Journal of the Association for Research in Otolaryngology*, *12*(6), 681–696. https://doi.org/10.1007/s10162-011-0281-4

Callaghan, P. T. (1993). *Principles of nuclear magnetic resonance microscopy*. Clarendon Press.

Chou, C.-F., Yu, J.-F., & Chen, C.-K. (2011). The natural vibration characteristics of human ossicles. *Chang Gung Medical Journal*, *34*(2), 160–165. Retrieved from Scopus.

Choukir, S. (2017). *Finite-element modelling of tympanic-membrane vibrations under quasi-static pressurization*. Retrieved from http://digitool.library.mcgill.ca/R/-?func=dbin-jump-full&object_id=150868&silo_library=GEN01

Decraemer, Dirckx, J. J. J., & Funnell, W. R. J. (2003). Three-dimensional modelling of the middle-ear ossicular chain using a commercial high-resolution X-ray CT scanner. *Journal of the Association for Research in Otolaryngology: JARO*, *4*(2), 250–263. https://doi.org/10.1007/s10162-002-3030-x

Decraemer, & Khanna, S. M. (1999). *New insights in the functioning of the middle ear*.

Decraemer, & Khanna, S. M. (2000). Three-dimensional vibration of the ossicular chain in the cat. *Fourth International Conference on Vibration Measurements by Laser Techniques: Advances and Applications*, *4072*, 401–411. https://doi.org/10.1117/12.386747

Decraemer, Khanna, S. M., & Dirckx, J. J. J. (2002). The integration of detailed 3D anatomical data for the quantitative description of 3D vibration of a biological structure: An illustration from the middle ear. *Fifth International Conference on Vibration Measurements by Laser Techniques: Advances and Applications*, *4827*, 148–158. https://doi.org/10.1117/12.468136

Decraemer, W. F., Dirckx, J. J., & Funnell, W. R. (1991). Shape and derived geometrical parameters of the adult, human tympanic membrane measured with a phase-shift moiré interferometer. *Hearing Research*, *51*(1), 107–121.

Dirckx, J. J., Decraemer, W. F., von Unge, M., & Larsson, C. (1998). Volume displacement of the gerbil eardrum pars flaccida as a function of middle ear pressure. *Hearing Research*, *118*(1–2), 35–46.

Dirckx, J. J. J., & Decraemer, W. F. (1991). Human tympanic membrane deformation under static pressure. *Hearing Research*, *51*(1), 93–105. https://doi.org/10.1016/0378-5955(91)90009-X

Dirckx, J. J. J., & Decraemer, W. F. (2001). Effect of middle ear components on eardrum quasi-static deformation. *Hearing Research*, *157*(1), 124–137. https://doi.org/10.1016/S0378-5955(01)00290-8

Dirckx, J. J. J., Decraemer, W. F., von Unge, M., & Larsson, C. (1997). Measurement and modeling of boundary shape and surface deformation of the Mongolian gerbil pars flaccida. *Hearing Research*, *111*(1), 153–164. https://doi.org/10.1016/S0378-5955(97)00108-1

Djerić, D., Savić, D., & Polić, D. (1987). A scanning electron microscopic study of the incudostapedial joint. *Revue De Laryngologie - Otologie - Rhinologie*, *108*(5), 463–466.

Egolf, D. P., Nelson, D. K., Howell, H. C., & Larson, V. D. (1993). Quantifying ear-canal geometry with multiple computer-assisted tomographic scans. *The Journal of the Acoustical Society of America*, *93*(5), 2809–2819. https://doi.org/10.1121/1.405802

Eiber, A., Freitag, H. G., Burkhardt, C., Hemmert, W., Maassen, M., Rodriguez Jorge, J., & Zenner, H. P. (1999). Dynamics of middle ear prostheses—Simulations and measurements. *Audiology & Neuro-Otology*, *4*(3–4), 178–184. https://doi.org/10.1159/000013838

Elfarnawany, M., Rohani, S. A., Ghomashchi, S., Allen, D. G., Zhu, N., Agrawal, S. K., & Ladak, H. M. (2017). Improved middle-ear soft-tissue visualization using synchrotron radiation phase-contrast imaging. *Hearing Research*, *354*, 1–8. https://doi.org/10.1016/j.heares.2017.08.001

Elkhouri, N., Liu, H., & Funnell, W. RobertJ. (2006). Low-frequency finite-element modeling of the gerbil middle ear. *JARO: Journal of the Association for Research in Otolaryngology*, *7*(4), 399–411. https://doi.org/10.1007/s10162-006-0055-6

Eysell, A. (1970). *Beiträge zur Anatomie des Steigbügels und seiner Verbindungen*. *5*, 237–249. https://doi.org/10.1007/BF01804371

Funnell, W. R., & Decraemer, W. F. (1996). On the incorporation of moiré shape measurements in finite-element models of the cat eardrum. *The Journal of the Acoustical Society of America*, *100*(2 Pt 1), 925–932. https://doi.org/10.1121/1.416252

Funnell, W. R. J., Decraemer, von Unge, M., & Dirckx. (1999). *Finite-element modelling of the gerbil eardrum and middle ear*. Retrieved from http://audilab.bmed.mcgill.ca/~funnell/AudiLab/ARO2000g/

Funnell, W. R. J., Decraemer, von Unge, M., & Dirckx. (2000). *Finite-element modelling of the gerbil eardrum and middle ear*. Retrieved from http://audilab.bmed.mcgill.ca/~funnell/AudiLab/ARO2000g/

Funnell, W. R. J., Heng Siah, T., McKee, M. D., Daniel, S. J., & Decraemer. (2005). On the coupling between the incus and the stapes in the cat. *Journal of the Association for Research in Otolaryngology: JARO*, *6*(1), 9–18. https://doi.org/10.1007/s10162-004-5016-3

Funnell, W. R. J., Khanna, S. M., & Decraemer. (1992). On the degree of rigidity of the manubrium in a finite-element model of the cat eardrum. *The Journal of the Acoustical Society of America*, *91*(4), 2082–2090. https://doi.org/10.1121/1.403694

Funnell, W. R. J., & Laszlo, C. A. (1978). Modeling of the cat eardrum as a thin shell using the finite-element method. *The Journal of the Acoustical Society of America*, *63*(5), 1461–1467. https://doi.org/10.1121/1.381892

Funnell, W. R. J., & Phelan, K. E. (1981). Finite-element modeling of the middle-ear ossicles. *The Journal of the Acoustical Society of America*, *69*(S1), S14–S14. https://doi.org/10.1121/1.386393

Gan, R. Z., Feng, B., & Sun, Q. (2004). Three-dimensional finite element modeling of human ear for sound transmission. *Annals of Biomedical Engineering*, *32*(6), 847–859. https://doi.org/10.1023/B:ABME.0000030260.22737.53

Gan, R. Z., Sun, Q., Dyer, R., Chang, K.-H., & Dormer, K. (2002). Three-dimensional modeling of middle ear biomechanics and its applications. *Otology & Neurotology*, *23*(3), 271–280.

Gan, R. Z., Sun, Q., Feng, B., & Wood, M. W. (2006). Acoustic–structural coupled finite element analysis for sound transmission in human ear—Pressure distributions. *Medical Engineering & Physics*, *28*(5), 395–404. https://doi.org/10.1016/j.medengphy.2005.07.018

Gea. (2012). *The application of microtomography in research of middle ear mechanics of gerbil and human at static pressure changes*. Retrieved from https://hdl.handle.net/10067/826730151162165141

Gea, Decraemer, Funnell, R. W. J., Dirckx, J. J. J., & Maier, H. (2010). Tympanic membrane boundary deformations derived from static displacements observed with computerized tomography in human and gerbil. *Journal of the Association for Research in Otolaryngology*, *11*(1), 1–17. https://doi.org/10.1007/s10162-009-0192-9

Ghiz, A. F., Salt, A. N., DeMott, J. E., Henson, M. M., Henson, O. W., & Gewalt, S. L. (2001). Quantitative anatomy of the round window and cochlear aqueduct in guinea pigs. *Hearing Research*, *162*(1–2), 105–112.

Gonzalez, R. C. (2009). *Digital Image Processing*. Pearson Education.

Greef, D. D., Buytaert, J. A. N., Aerts, J. R. M., Hoorebeke, L. V., Dierick, M., & Dirckx, J. (2015). Details of human middle ear morphology based on micro-CT imaging of phosphotungstic acid stained samples. *Journal of Morphology*, *276*(9), 1025–1046. https://doi.org/10.1002/jmor.20392

Greenbaum, A., Chan, K. Y., Dobreva, T., Brown, D., Balani, D. H., Boyce, R., … Gradinaru, V. (2017). Bone CLARITY: Clearing, imaging, and computational analysis of osteoprogenitors within intact bone marrow. *Science Translational Medicine*, *9*(387), eaah6518. https://doi.org/10.1126/scitranslmed.aah6518

Gulya, A. J. (1995). Anatomy of the temporal bone with surgical implications. *Otolaryngology–Head and Neck Surgery*, *112*(5), P165–P165. https://doi.org/10.1016/S0194-5998(05)80437-1

H bridge. (2019). In *Wikipedia*. Retrieved from https://en.wikipedia.org/w/index.php?title=H_bridge&oldid=918542778

Henson, M. M., Henson, O. W., Gewalt, S. L., Wilson, J. L., & Johnson, G. A. (1994). Imaging the cochlea by magnetic resonance microscopy. *Hearing Research*, *75*(1–2), 75–80.

Henson, O. J., Hezel, Henson, M., Presson, Amour, Stancil, & Gewalt. (1999). *Comparative analysis of the vertebrate ear using magnetic resonance microscopy*. Presented at the ARO MidWinter Meeting.

Herman, G. T. (2009). *Fundamentals of computerized tomography: Image reconstruction from projections* (2nd ed.). Retrieved from https://www.springer.com/gp/book/9781852336172

Himi, T., Kataura, A., Sakata, M., Odawara, Y., Satoh, J. I., & Sawaishi, M. (1996). Three-dimensional imaging of the temporal bone using a helical CT scan and its application in patients with cochlear implantation. *ORL; Journal for Oto-Rhino-Laryngology and Its Related Specialties*, *58*(6), 298–300. https://doi.org/10.1159/000276857

Howard, J. D., Elster, A. D., & May, J. S. (1990a). Temporal bone: Three-dimensional CT. Part I. Normal anatomy, techniques, and limitations. *Radiology*, *177*(2), 421–425. https://doi.org/10.1148/radiology.177.2.2217779

Howard, J. D., Elster, A. D., & May, J. S. (1990b). Temporal bone: Three-dimensional CT. Part II. Pathologic alterations. *Radiology*, *177*(2), 427–430. https://doi.org/10.1148/radiology.177.2.2171013

Huisken, J., Swoger, J., Lindek, S., & Stelzer, E. H. K. (2006). Selective plane illumination microscopy. In J. B. Pawley (Ed.), *Handbook Of Biological Confocal Microscopy* (pp. 672–679). https://doi.org/10.1007/978-0-387-45524-2_37

Hunter, L. (2017, April). *3D X-ray microscopy characterization*. Retrieved from https://www.zeiss.com/content/dam/Microscopy/us/download/pdf/application-notes/x-ray-microscopy/en_44_013_041_additive_manufacturing.pdf

Hüttenbrink, K. B. (1988). The mechanics of the middle-ear at static air pressures: The role of the ossicular joints, the function of the middle-ear muscles and the behaviour of stapedial prostheses. *Acta Oto-Laryngologica. Supplementum*, *451*, 1–35.

Ilg, E., Mayer, N., Saikia, T., Keuper, M., Dosovitskiy, A., & Brox, T. (2017). *FlowNet 2.0: Evolution of Optical Flow estimation with Deep Networks*. 2462–2470. Retrieved from http://openaccess.thecvf.com/content_cvpr_2017/html/Ilg_FlowNet_2.html

Jing, D., Zhang, S., Luo, W., Gao, X., Men, Y., Ma, C., … Zhao, H. (2018). Tissue clearing of both hard and soft tissue organs with the PEGASOS method. *Cell Research*, *28*(8), 803. https://doi.org/10.1038/s41422-018-0049-z

Kanzaki, S., Takada, Y., Niida, S., Takeda, Y., Udagawa, N., Ogawa, K., … Matsuo, K. (2011). Impaired vibration of auditory ossicles in osteopetrotic mice. *The American Journal of Pathology*, *178*(3), 1270–1278. https://doi.org/10.1016/j.ajpath.2010.11.063

Karmody, C. S., Northrop, C. C., & Levine, S. R. (2009). The incudostapedial articulation: New concepts. *Otology & Neurotology: Official Publication of the American Otological Society, American Neurotology Society [and] European Academy of Otology and Neurotology*, *30*(7), 990–997. https://doi.org/10.1097/MAO.0b013e3181b0fff7

Keys, R. (1981). Cubic convolution interpolation for digital image processing. *IEEE Transactions on Acoustics, Speech, and Signal Processing*, *29*(6), 1153–1160. https://doi.org/10.1109/TASSP.1981.1163711

Koike, T., Wada, H., & Kobayashi, T. (2002). Modeling of the human middle ear using the finite-element method. *The Journal of the Acoustical Society of America*, *111*(3), 1306–1317. https://doi.org/10.1121/1.1451073

Kose, O., Funnell, W. R. J., & Daniel, S. J. (2017). In vivo experimental study of gerbil eardrum vibrations under static pressures. *Presented at the 40th MidWinter Meeting ,Association for Research in Otolaryngology, Baltimore*.

Kose, O., Funnell, W. R. J., & Daniel, S. J. (2019). Vibration measurements of the gerbil eardrum under quasi-static pressure steps. *JARO: Journal of the Association for Research in Otolaryngology*, *Under review*.

Kuypers, L. C., Dirckx, J. J. J., Decraemer, & Timmermans, J.-P. (2005). Thickness of the gerbil tympanic membrane measured with confocal microscopy. *Hearing Research*, *209*(1), 42–52. https://doi.org/10.1016/j.heares.2005.06.003

Ladak, H. M., Decraemer, W. F., Dirckx, J. J. J., & Funnell, W. R. J. (2004). Response of the cat eardrum to static pressures: Mobile versus immobile malleus. *The Journal of the Acoustical Society of America*, *116*(5), 3008–3021. https://doi.org/10.1121/1.1802673

Ladak, H. M., & Funnell, W. R. J. (1996). Finite-element modeling of the normal and surgically repaired cat middle ear. *The Journal of the Acoustical Society of America*, *100*(2), 933–944. https://doi.org/10.1121/1.416205

Lane, J. I., Witte, R. J., Driscoll, C. L. W., Camp, J. J., & Robb, R. A. (2004). Imaging microscopy of the middle and inner ear: Part I: CT microscopy. *Clinical Anatomy*, *17*(8), 607–612. https://doi.org/10.1002/ca.20059

Lane, J. I., Witte, R. J., Henson, O. W., Driscoll, C. L. W., Camp, J., & Robb, R. A. (2005). Imaging microscopy of the middle and inner ear: Part II: MR microscopy. *Clinical Anatomy*, *18*(6), 409–415. https://doi.org/10.1002/ca.20152

Lee, C. F., Chen, P.-R., Lee, W.-J., Chen, J.-H., & Liu, T.-C. (2006). Three-dimensional reconstruction and modeling of middle ear biomechanics by high-resolution computed tomography and finite element analysis. *Laryngoscope*, *116*(5), 711–716. https://doi.org/10.1097/01.mlg.0000204758.15877.34

Lee, D. H., Chan, S., Salisbury, C., Kim, N., Salisbury, K., Puria, S., & Blevins, N. H. (2010). Reconstruction and exploration of virtual middle-ear models derived from micro-CT datasets. *Hearing Research*, *263*(0), 198–203. https://doi.org/10.1016/j.heares.2010.01.007

Lesser, T. H., Williams, K. R., & Blayney, A. W. (1991). Mechanics and materials in middle ear reconstruction. *Clinical Otolaryngology and Allied Sciences*, *16*(1), 29–32.

Lim, D. J. (1968a). Tympanic membrane: Electron microscopic observation Part I: Pars tensa. *Acta Oto-Laryngologica*, *66*(1–6), 181–198. https://doi.org/10.3109/00016486809126286

Lim, D. J. (1968b). Tympanic membrane Part II.: Pars flaccida. *Acta Oto-Laryngologica*, *66*(1–6), 515–532. https://doi.org/10.3109/00016486809126316

Lucas, B. D., & Kanade, T. (1981). An iterative image registration technique with an application to stereo vision. *Proceedings of the 7th International Joint Conference on Artificial Intelligence - Volume 2*, 674–679. Retrieved from http://dl.acm.org/citation.cfm?id=1623264.1623280

Maftoon, N. (2014). *Experimental and modelling study of gerbil middle ear* (Ph.D. thesis, McGill University). Retrieved from http://digitool.library.mcgill.ca/thesisfile126973.pdf

Metscher, B. D. (2009). MicroCT for comparative morphology: Simple staining methods allow high-contrast 3D imaging of diverse non-mineralized animal tissues. *BMC Physiology*, *9*(1), 11. https://doi.org/10.1186/1472-6793-9-11

Motallebzadeh, H., Maftoon, N., Pitaro, J., Funnell, W. R. J., & Daniel, S. J. (2017a). Finite-Element Modelling of the Acoustic Input Admittance of the Newborn Ear Canal and Middle Ear. *Journal of the Association for Research in Otolaryngology*, *18*(1), 25–48. https://doi.org/10.1007/s10162-016-0587-3

Motallebzadeh, H., Maftoon, N., Pitaro, J., Funnell, W. R. J., & Daniel, S. J. (2017b). Fluid-Structure Finite-Element Modelling and Clinical Measurement of the Wideband Acoustic Input Admittance of the Newborn Ear Canal and Middle Ear. *Journal of the Association for Research in Otolaryngology*, *18*(5), 671–686. https://doi.org/10.1007/s10162-017-0630-z

Neudert, M., Beleites, T., Ney, M., Kluge, A., Lasurashvili, N., Bornitz, M., … Zahnert, T. (2010). Osseointegration of titanium prostheses on the stapes footplate. *Journal of the Association for Research in Otolaryngology*, *11*(2), 161–171. https://doi.org/10.1007/s10162-009-0202-y

Ogando, P., Röösli, C., Karmody, C., & Northrop, C. (2013). The incudostapedial articulation in Down's syndrome (Trisomy 21): A temporal bone study. *Otology & Neurotology*, *34*(8), 1489–1495. https://doi.org/10.1097/MAO.0b013e318289866e

OpenCV. (n.d.). *Image Pyramids*. Retrieved from https://docs.opencv.org/2.4/doc/tutorials/imgproc/pyramids/pyramids.html

Paragios, N., Chen, Y., & Faugeras, O. D. (Eds.). (2006). *Handbook of mathematical models in computer vision*. Retrieved from https://www.springer.com/gp/book/9780387263717

Prendergast, P. J., Ferris, P., Rice, H. J., & Blayney, A. W. (1999). Vibro-acoustic modelling of the outer and middle ear using the finite-element method. *Audiology and Neurotology*, *4*(3–4), 185–191. https://doi.org/10.1159/000013839

Puria, S., & Steele, C. (2010). Tympanic-membrane and malleus-incus-complex co-adaptations for high-frequency hearing in mammals. *Hearing Research*, *263*(1–2), 183–190. https://doi.org/10.1016/j.heares.2009.10.013

Qi, L., Funnell, W. R. J., & Daniel, S. J. (2008). A nonlinear finite-element model of the newborn middle ear. *The Journal of the Acoustical Society of America*, *124*(1), 337–347. https://doi.org/10.1121/1.2920956

Qi, L., Liu, H., Lutfy, J., Funnell, W. R. J., & Daniel, S. J. (2006). A nonlinear finite-element model of the newborn ear canal. *The Journal of the Acoustical Society of America*, *120*(6), 3789–3798. https://doi.org/10.1121/1.2363944

Rau, T. S., Würfel, W., Lenarz, T., & Majdani, O. (2013). Three-dimensional histological specimen preparation for accurate imaging and spatial reconstruction of the middle and inner ear. *International Journal of Computer Assisted Radiology and Surgery*, *8*(4), 481–509. https://doi.org/10.1007/s11548-013-0825-7

Ravicz, M. E., Rosowski, J. J., & Voigt, H. F. (1992). Sound-power collection by the auditory periphery of the Mongolian gerbil Meriones unguiculatus. I: Middle-ear input impedance. *The Journal of the Acoustical Society of America*, *92*(1), 157–177. https://doi.org/10.1121/1.404280

Reisser, C., Schubert, O., Forsting, M., & Sartor, K. (1996). Anatomy of the temporal bone: Detailed three-dimensional display based on image data from high-resolution helical CT: a preliminary report. *The American Journal of Otology*, *17*(3), 473–479.

Rodt, T., Ratiu, P., Becker, H., Bartling, S., Kacher, D. F., Anderson, M., … Kikinis, R. (2002). 3D visualisation of the middle ear and adjacent structures using reconstructed multi-slice CT datasets, correlating 3D images and virtual endoscopy to the 2D cross-sectional images. *Neuroradiology*, *44*(9), 783–790. https://doi.org/10.1007/s00234-002-0784-0

Rohani, S. A., Ghomashchi, S., Umoh, J., Holdsworth, D. W., Agrawal, S. K., & Ladak, H. M. (2016). Iodine potassium iodide improves the contrast-to-noise ratio of micro-computed tomography images of the human middle ear. *Journal of Microscopy*, *264*(3), 334–338. https://doi.org/10.1111/jmi.12447

Rosowski, J. J., Ravicz, M. E., Teoh, S. W., & Flandermeyer, D. (1999). Measurements of middle-ear function in the Mongolian gerbil, a specialized mammalian ear. *Audiology & Neuro-Otology*, *4*(3–4), 129–136. https://doi.org/10.1159/000013831

Salih, W. H. M., Buytaert, J. A. N., Aerts, J. R. M., Vanderniepen, P., Dierick, M., & Dirckx, J. J. J. (2012). Open access high-resolution 3D morphology models of cat, gerbil, rabbit, rat and human ossicular chains. *Hearing Research*, *284*(1), 1–5. https://doi.org/10.1016/j.heares.2011.12.004

Salih, W. H. M., Buytaert, J. A. N., & Dirckx, J. J. J. (2011a). Measurement of micro-motions within non-transparent objects using gray scale information in x-ray stereo projection imaging. *Measurement Science and Technology*, *22*(3), 035801. https://doi.org/10.1088/0957-0233/22/3/035801

Salih, W. H. M., Soons, J. A. M., & Dirckx, J. J. J. (2011b). High-resolution 3D translation measurements using point source x-ray stereoscopy. *Measurement Science and Technology*, *22*(2), 025502. https://doi.org/10.1088/0957-0233/22/2/025502

Salih, W. H. M., Soons, J. A. M., & Dirckx, J. J. J. (2016). 3D displacement of the middle ear ossicles in the quasi-static pressure regime using new X-ray stereoscopy technique. *Hearing Research*, *340*, 60–68. https://doi.org/10.1016/j.heares.2015.12.003

Shapiro, R. (2014). *An experimental study of vibrations in the gerbil middle ear under static pressure* (McGill University). Retrieved from http://digitool.library.mcgill.ca/R/-?func=dbin-jump-full&object_id=126993&silo_library=GEN01

Shimada, T., & Lim, D. J. (1971). The fiber arrangement of the human tympanic membrane. A scanning electron microscopic observation. *The Annals of Otology, Rhinology, and Laryngology*, *80*(2), 210–217. https://doi.org/10.1177/000348947108000207

Shrapnell, H. J. (1832). On the structure of the os incus. *London Medical Gazette*, *12*, 171–174.

Silver, R. D., Djalilian, H. R., Levine, S. C., & Rimell, F. L. (2002). High-resolution magnetic resonance imaging of human cochlea. *The Laryngoscope*, *112*(10), 1737–1741. https://doi.org/10.1097/00005537-200210000-00005

Sim, J. H., Puria, S., Steele, C. R., & Steele, C. R. (2007). Calculation of inertial properties of the malleus-incus complex from micro-CT imaging. *Journal of Mechanics of Materials and Structures*, *2*(8), 1515–1524. https://doi.org/10.2140/jomms.2007.2.1515

Sun, Q., Gan, R. Z., Chang, K.-H., & Dormer, K. J. (2002). Computer-integrated finite element modeling of human middle ear. *Biomechanics and Modeling in Mechanobiology*, *1*(2), 109–122. https://doi.org/10.1007/s10237-002-0014-z

Thompson, A. C., Llacer, J., Campbell Finman, L., Hughes, E. B., Otis, J. N., Wilson, S., & Zeman, H. D. (1984). Computed tomography using synchrotron radiation. *Nuclear Instruments and Methods in Physics Research*, *222*(1), 319–323. https://doi.org/10.1016/0167-5087(84)90550-7

Unbehauen, H. (2009). *Control systems, robotics and automation- Volume II: Ssystem analysis and control: Classical approaches-II*. EOLSS Publications.

Vogel, & Schmitt, T. (1998). 3D visualization of middle ear structures. *Medical Imaging 1998: Image Display*, *3335*, 141–151. https://doi.org/10.1117/12.312487

Vogel, U. (1999). New approach for 3D imaging and geometry modeling of the human inner ear. *ORL*, *61*(5), 259–267. https://doi.org/10.1159/000027683

Vogel, Zahnert, T., Hofmann, G., & Hüttenbrink, K.-B. (2000). *3D-imaging of internal temporal bone structures for geometric modeling of the human hearing organ*. https://doi.org/10.1142/9789812793980_0007

Voie. (2002). Imaging the intact guinea pig tympanic bulla by orthogonal-plane fluorescence optical sectioning microscopy. *Hearing Research*, *171*(1–2), 119–128.

Voie, Burns, D. H., & Spelman, F. A. (1993). Orthogonal-plane fluorescence optical sectioning: Three-dimensional imaging of macroscopic biological specimens. *Journal of Microscopy*, *170*(Pt 3), 229–236.

von Unge, M., Decraemer, W. F., Bagger-Sjöbäck, D., & Dirckx, J. J. (1993). Displacement of the gerbil tympanic membrane under static pressure variations measured with a real-time differential moire interferometer. *Hearing Research*, *70*(2), 229–242. https://doi.org/10.1016/0378-5955(93)90161-S

Wada, H., Metoki, T., & Kobayashi, T. (1992). Analysis of dynamic behavior of human middle ear using a finite-element method. *The Journal of the Acoustical Society of America*, *92*(6), 3157–3168. https://doi.org/10.1121/1.404211

Wang, H., Northrop, C., Burgess, B., Liberman, M. C., & Merchant, S. N. (2006). Three-dimensional virtual model of the human temporal bone: A stand-alone, downloadable

teaching tool. *Otology & Neurotology: Official Publication of the American Otological Society, American Neurotology Society [and] European Academy of Otology and Neurotology*, *27*(4), 452–457. https://doi.org/10.1097/01.mao.0000188353.97795.c5

Wen, Y.-H., Hsu, L.-P., Chen, P.-R., & Lee, C.-F. (2006). *Design optimization of cartilage myringoplasty using finite element analysis* (Vol. 18).

Williams, K. R., & Lesser, T. H. (1990). A finite element analysis of the natural frequencies of vibration of the human tympanic membrane. Part I. *British Journal of Audiology*, *24*(5), 319–327.

Wolfe, D. (2019). Tissue processing. In S. K. Suvarna, C. Layton, & J. D. Bancroft (Eds.), *Bancroft's Theory and Practice of Histological Techniques (Eighth Edition)* (pp. 73–83). https://doi.org/10.1016/B978-0-7020-6864-5.00006-2

Appendix 1

Arduino code to generate pressure signals

```
int defSpeed = 255;
int pause = 0; //pause=0 means active, pause=1 means stop
// Pressure reading variables setup
int val;
float val_old;
int analogPin = 0;
int diff;
int flag_reach = 920;
int counter_PID = 0;
int flag_forward = 0;
int flag_reverse = 0;
// User input values
int userInput[3];      // raw input from serial buffer, 3 bytes
int startbyte = 0;         // start byte, initialize reading input
int masterPause = 1;   // pause system now? initialized to 1 for breaking
int pressureVal = 460;       // desired pressure value to achieve
float speedTarget;    // desired speed
float Speed;          // current speed of pump
int initialSpeed = 0;   // initial speed of motor
int speedNew = 0;       // refined speed of motor
int i;
int valNum = 0;         // number of times pressures added
unsigned long Time;       // passed time
unsigned long Time_old; // passed old time
int offset=460;
int gain=12;
int safePressure=460;   // pressure to stop the pump

// PID values
int PID_delay=10;              // window of PID=serialVal_delay*PID_delay in ms
float kp = 0.5;                // proportional coefficient
float ki = 0.02;                // integration coefficient
float kd = 0.05;                // derivative coefficient
float valSum = 0;           // sum of preesure values
float SumEr = 0;            // sum of errors for integration
float er = 0;              // error
float er_old = 0;           // error of previous step
float PID = 0;              // PID value
int speedRatio=3;           // convesion ration of pressure speed to pump speed
/*****************************************************************************/
// Limit Values
int serialVal_delay=10;       // delay between sending pressure values
int speedCorrection=12;       // added to desired speed
int tolerance = 2;            // tolerance in sweep mode
int rotate_tolerance = 2;     // tolerance in rotate mode
int delay_reach=100;          // delay after sending reach flag
bool reach=false;
void setup() {
  // motor pin connections
  pinMode(2, OUTPUT);  // directional voltage pin
  pinMode(3, OUTPUT);  // PWM pin
  pinMode(4, OUTPUT);  // directional voltage pin
```

```
  // serial connection, 9600 baud
  Serial.begin(9600);
}
//Motor functions
void stay()
{
  digitalWrite(2, HIGH);
  digitalWrite(4, HIGH);
  //Serial.println(flag_stay);
}
void forward()
{
  digitalWrite(2, LOW);
  digitalWrite(4, HIGH);
  // Serial.println(flag_forward);
}
void reverse()
{
  digitalWrite(2, HIGH);
  digitalWrite(4, LOW);
  // Serial.println(flag_reverse);
}
void loop()
{
  if (Serial.available() > 2)
  {
    startbyte = Serial.read();
    if (startbyte == 255) {
      for (i = 0; i < 3; i++) {
        userInput[i] = Serial.read();
      }
      //Amplify user input by 4 due to 256 bit transmission. (256*4=1028 Sensor unit)
      speedTarget = userInput[2] * 2;
      pressureVal = userInput[1] * 4;
      masterPause = userInput[0];

      safePressure=round(((pressureVal-offset)*12*1.05+100)/gain+offset);  // safe pressure value to
stop the pump 5% of desired pressure(+100 Pa for 0 Pa)
      defSpeed = initialSpeed;
      speedTarget = 360+speedCorrection;
         PID_delay=round(-0.07*speedTarget+33);   // calculate window length for PID controller to
refine speed
      //Set pump speed
      initialSpeed = floor(0.3175 * speedTarget + 111.9); // initial motor speed from speed target
        if (initialSpeed < 171) {
        initialSpeed = 171;
      }
      else if (initialSpeed > 255) {
        initialSpeed = 255;
      }
      er_old = 0;
      PID = 0;
      counter_PID = PID_delay;  //start PID right after new pressure input
      speedNew = 0;
      Speed = 0;
      er = 0;
      valSum = 0;
      valNum = 0;
      flag_forward = 0;
```

```
    flag_reverse = 0;
    reach=false;
    val_old = analogRead(analogPin);
    Time_old=millis();
  }
}

// If move command is given
if (masterPause == 0) {
  val = analogRead(analogPin);
  Time = millis();
  Serial.println(val);
  counter_PID += 1;
  valSum += val;
  valNum += 1;
  delay(serialVal_delay);
  if (counter_PID >= PID_delay) {
    valSum = valSum / valNum;
    Speed = (abs(valSum - val_old) * 12 * 1000) / (Time - Time_old);
    er = speedTarget - Speed;
    //PID = (kp * er +ki*SumEr+ kd * (er - er_old)) / speedRation;     //PID with P, I, and D
    PID = (kp * er + kd * (er - er_old)) / speedRatio;  // PD controller
    speedNew = defSpeed + floor(PID);
    if ((speedNew >= 161) && (speedNew <= 255)) {
      defSpeed = speedNew;
    }
    else if (speedNew < 161) {
      defSpeed = 161;
    }
    else if (speedNew > 255) {
      defSpeed = 255;
    }
    counter_PID = 0;
    flag_forward = 0;
    flag_reverse = 0;
    er_old = er;
    Time_old = Time;
    val_old = valSum;
    valNum = 0;
    valSum = 0;
  }
  // send reach flag
  if ((abs(val-pressureVal)<= tolerance) && reach==false){
    Serial.println(flag_reach);
    reach=true;
    delay(delay_reach);
  }
   diff = val - safePressure;
  if ((diff >= -tolerance) && (diff <= tolerance)) {
    stay();
    flag_forward = 0;
    flag_reverse = 0;
  }
  else if ((diff < -tolerance) && (flag_forward == 0)) {
    forward();
    analogWrite(3, defSpeed);
    flag_forward = 1;
    flag_reverse = 0;
  }
```

```
    else if ((diff > tolerance) && (flag_reverse == 0)) {
      reverse();
      analogWrite(3, defSpeed);
      flag_forward = 0;
      flag_reverse = 1;
    }
  }
//If stop command is given
  else if ((masterPause == 1)) {
    stay();
    delay(100);
  }
  //If pressure reading command is given
  else if (masterPause == 2) {
    stay();
    val = analogRead(analogPin);
    Serial.println(val);
    delay(10);
  }
  //If rotate command is given
  else if (masterPause == 3) {
    val = analogRead(analogPin);
    defSpeed = 171;
    diff = val - pressureVal;
    if ((diff <= rotate_tolerance) && (diff >= -rotate_tolerance)) {
      stay();
      delay(1000);
      flag_forward = 0;
      flag_reverse = 0;
    }
    else if ((diff < -rotate_tolerance) && (flag_forward == 0)) {
      forward();
      analogWrite(3, defSpeed);
      flag_forward = 1;
      flag_reverse = 0;
    }
    else if ((diff > rotate_tolerance) && (flag_reverse == 0)) {
      reverse();
      analogWrite(3, defSpeed);
      flag_forward = 0;
      flag_reverse = 1;
    }
  }
}
```

Appendix 2

Python code to send user's input to the Arduino and receive pressure data

```
import serial
import time
import datetime
import math
import numpy as np

#Definitions
usbport = 'com19' #Connected port
Dir="C:\\Users\\sajjad\\Desktop\\Data\\G44\\"
# Directory where the time domain results are to be stored
File_Name="d8.txt"     # Filename to save measured data

#Sensor variables
offset = 460
gain = 12
tolerence= 24
Default_Cycleno = 1
Default_Timedelay = 100
Default_pressureVal = 2500
Default_steps = 5
Default_speed = 340
direction=1

Dat= np.zeros((1,2))
# serial baud rate setup
ser = serial.Serial(usbport, 9600, timeout = 1)

# ----------------------------------------------------------------
# ROTATE MODE
# ----------------------------------------------------------------
def rotate(pressuretarget):
  masterPause=3
  setVal=int(pressuretarget/gain+offset)
  print 'Setting pressure to zero'
  #Send to Arduino
  ser.write(chr(255))
  ser.write(chr(masterPause))
  time.sleep(0.001)
  ser.write(chr(setVal/4))
  time.sleep(0.001)
  ser.write(chr(0))
  ser.flushOutput()
```

```
# ------------------------------------------------------------
# SWEEP MODE
# ------------------------------------------------------------
def sweep(pressureVal,Cycleno,FirstDelay,speed):
  print Dir
  if((0 <= pressureVal <= 3000) and (1 <= Cycleno <= 10) and (30>= FirstDelay >=0)):
    masterPause=0

    #Wait before the first sweep for positioning
    rotate(0)
##    time.sleep(FirstDelay)
    raw_input('<<Press Enter to start pressurization>>')

    DataFile=open(Dir+File_Name,'a')
    # Open a raw file to save the measured data into

    pressurestep=np.zeros((1,(Cycleno+1)*2))
    pressurestep[0,1:Cycleno*2:2]=pressureVal
    pressurestep[0,2:Cycleno*2+1:2]=-(pressureVal)

    for x in range(2,(Cycleno+1)*2+1): #Ordered number of points
        pressuretarget=pressurestep[0,x-1]
        #Triangle Wave definition
        print 'Speed target: ' + repr(speed)
        #Current pressure target
        print 'Pressure Target: ' + repr(pressuretarget)

        #Convert from Pa to sensor unit (with 4x reduction)
        setVal=int((pressuretarget)/gain+offset)
        print 'Input value: ' + repr(setVal) #Display input
        #Send to Arduino
        ser.write(chr(255))
        ser.write(chr(masterPause))
        time.sleep(0.001)
        ser.write(chr(setVal/4))
        time.sleep(0.001)
        ser.write(chr(speed/2))
        ser.flushOutput()

        while (True):
            #Read input, clean the signal and convert it to bytes
            incoming=ser.read(4).encode("utf-8")
            incoming=incoming.strip()
            #print incoming
            Ps=list(incoming)
            ser.flushInput()
            PS=0
            Dat[0][0]= time.time()
            if len(Ps) == 3:
```

```
                for i in range(2,-1,-1):
                        PS=PS+int(Ps[i])*10**(2-i)
                pressureSens = (gain*(PS-offset))
                if 200 <= PS <=700:
                  Dat[0][1]=pressureSens
                  np.savetxt(DataFile,Dat)
            if PS==920:
              print "Step Achieved"
              break
    #Finish
    masterPause=1
    ser.write(chr(255))
    ser.write(chr(masterPause))
    ser.write(chr(0))
    ser.write(chr(0))
    ser.flushOutput()
    DataFile.close()
  else:
     print "Value out of range"

# ---------------------------------------------------------------------
# SAVING PRESSURE SENSOR MODE
# ---------------------------------------------------------------------
def saveTofile():
    DataFile=open(Dir+File_Name,'a')
    masterPause=2
    try:
       while (True):
          #Initialize Arduino for pressure reading
          ser.write(chr(255))
          ser.write(chr(masterPause))
          ser.write(chr(0))
          ser.write(chr(0))
          ser.flushOutput()
          #Read input, clean the signal and convert it to bytes
          incoming=ser.read(4).encode("utf-8")
          incoming=incoming.strip()
          Ps=list(incoming)
          ser.flushInput()
          PS=0
          Dat[0][0]= time.time()
          if len(Ps) == 3:

             for i in range(2,-1,-1):
                PS=PS+int(Ps[i])*10**(2-i)
             pressureSens = (gain*(PS-offset))
             if 200 <= PS <=700:
                #print repr(pressureSens)
                Dat[0][1]=pressureSens
```

```
                    np.savetxt(DataFile,Dat)
                    time.sleep(0.001)
            except KeyboardInterrupt:
                masterPause=1
                ser.write(chr(255))
                ser.write(chr(masterPause))
                ser.write(chr(0))
                ser.write(chr(0))
                ser.flushOutput()
                DataFile.close()

        # ------------------------------------------------------------------------
        # SELECTING INPUT MODE
        # ------------------------------------------------------------------------
        pressureVal=raw_input("Positive/Negative maximum pressure value? (in Pa) ")
        Cycleno =raw_input("Number of cycles? (default is 1)  ")
        continueSaving=raw_input("Continue saving pressures? 1 for yes, 0 for no  ") #Continue
saving in file
        FirstDelay=raw_input("Delay (sec) before the first sweep? (DEFAULT WILL START
IMMEDIATELY)  ")
        if (pressureVal==""):
            pressureVal= Default_pressureVal
        if (Cycleno==""):
            Cycleno= Default_Cycleno
        if (FirstDelay==""):
            FirstDelay= 0
        sweep(int(pressureVal),int(Cycleno),int(FirstDelay),Default_speed)
        if (continueSaving==''):
            continueSaving=0
        if(int(continueSaving)==1): #Continue saving pressures
            print 'Saving pressures to file.....\nPress Ctrl+C to finish saving'
            saveTofile()
```

Appendix 3

X-CLARITY protocol (for whole mouse brain)

This protocol was developed by DLO and SJ (Watt Lab, Biology Department, McGill University, 2017-06-14). We received it from the Advanced BioImaging Facility (ABIF).

Step1:

Transcardially perfuse the animal with PBS containing heparin, and followed by PFA (4%).

Incubate the brain in 4% PFA at 4°C (up to a week and not more).

Wash the brain with PBS (several times) in a rotatory shaker. This step ensures that you get rid of PFA which may affect with the polymerization of the brain. Optionally, you can wash the brain in PBS at 4°C for 24 hours.

Step2:

Incubate the brain in 15 ml of Hydrogel solution at 4°C for precisely 24hours in 50 mL centrifuge tubes (do not exceed over 24 hours).

Hydrogel solution (total 15ml).

- 10X PBS 1.5 ml
- 40% Acrylamide 1.5 ml (Final 4%)
- 10% VA-044 375 ul (Final 0.25%)
- Filled with double distilled water (DDW) up to 15ml

Note: To make up 10X PBS and VA-044, please refer to the protocol at the end. If you are making the 25% VA-044 stock solution, please make sure the finale concentration of VA-044 is 0.25%.

Step3:

Place 50 ml centrifuge tube containing the Hydrogel solution and the brain in the Polymerization system and use the below settings to start the polymerization of the gel matrix.

- -90 kPa
- 37.0 °C
- 3 hours

Rinse the brain in the Electrophoretic tissue clearing (ETC) and transfer the brain to the tissue container (single chamber).

Place the chamber inside the ETC system.

Fill the chamber with ETC solution and empty the rest in the reservoir (Total 1L = 1 bottle).

Start the Pump at :

- 30 RPM
- Counter-clockwise (CCW)

Use the below settings to set the ETC Controller and press Start.

- Current 1.0 A (Maintained endogenous protein)
- Temp. 37.0 °C
- Time 24.0-26.0 hours (for whole brain), check every 6hours if possible.

  Exchange ETC solution after 24hours!!!! Please make sure to stop the pump before opening the chamber to check the brain.

Once cleared, transfer the brain into PBS Overnight (O/N) at Room temperature (RT).

- Brain could be stored in PBS for few days, this might cause the brain to become cloudy, which should be restored when placed in the mounting solution.
- The brain may be stored in 1x PBS at 4ºC for up to 1 week until immunolabeling or imaging.

Step4: Mounting and Imaging

- Prior to imaging, incubate the brain in mounting solution (5~10ml) for 24h at room temperature.
- Replace with fresh mounting solution and incubate for additional 1-2 hours.

Step5: ETC Clean up

Fill the chamber with 500 ml of fresh ETC solution.

Set ETC Controller at :

- Current 1.5 A
- Temp. 37.0 °C
- Pump 30 RPM (ACW)
- Time CL (Press down after ‘’----‘’)

Run for 1-2h.

Reverse pump to empty the chamber and tubing – Clockwise (CW).

Wash the ETC chamber with deionized water (white tap; 1L).

Reverse the pump again – Counter-Clockwise (CCW) and press the prime button (>>) for a few hours.

Let it dry.

10% VA-044 Stock Solution (5ml)

To make 10ml of 10% VA-044 Stock solution

- Add 0.5g of VA-044.
- Filled up to 5ml of DDW.

Keep refrigerated with the X-CLARITY open kit.

Optional: You can also dissolve 2.5g of VA-044 in 10ml 1X PBS to make 25% (w/v) stock solution. Aliquot (e.g. 0.5ml each) and store at -20oC for up to 6 month. Thaw at 4oC or on ice before use.

10X PBS solution (500ml)

- Add 45g of Sodium Chloride
- Add 50ml of 10X Phosphate Buffer (10X PB). Final [0.1M].
- Fill up to 500ml with DDW.
- pH = 7.4

10X PB (0.1M) solution (200ml)

- Add 19ml of 0.2M Monobasic sodium phosphate (27.6g/L).
- Add 81ml of 0.2M dibasic sodium phosphate (28.4g/L).
- Add 100ml of double distilled water (ddH_2O).
- Adjusted the pH to 7.4

Refraction Index Matching Solution (RIMS)

- Add 6ml of 10X PB
- Add 24ml of double distilled water (ddH_2O).
- Dissolve 40g of Histodenz in Phosphate Buffer (0.02M).
- Add 0.01% Sodium Azide (~3mg)
- Adjusted pH to 7.5 using NaOH.